Universität Ulm
Institut für
Quanteninformationsverarbeitung

Quantum State Manipulation and Dynamics in Micro Ion Traps

Dissertation

zur Erlangung des Doktorgrades Dr. rer. nat.
der Fakultät für Naturwissenschaften der Universität Ulm

vorgelegt von

Frank Ziesel

aus Leutkirch i. A.

2012

Amtierender Dekan:	Prof. Dr. Fedor Jelezko
Erstprüfer:	Prof. Dr. Ferdinand Schmidt-Kaler
Zweitprüfer:	Prof. Dr. Johannes Hecker Denschlag
Tag der Promotion:	26.02.2013

Hiermit erkläre ich, Frank Ziesel, dass ich die vorliegende Dissertation selbstständig angefertigt und keine anderen als die angegebenen Quellen und Hilfsmittel benutzt sowie die wörtlich und inhaltlich übernommenen Stellen als solche kenntlich gemacht und die Satzung der Universität Ulm zur Sicherung guter wissenschaftlicher Praxis beachtet habe.

Frank Ziesel
Ulm, den 10. Dezember 2012

Zusammenfassung

Gefangene Ionen in einer Paul-Falle bilden ein System, welches ein höchstes Maß an Kontrolle ermöglicht. Der interne und externe Ionenzustand kann präzise mit Hilfe optischer Übergänge manipuliert werden. Auf diese Weise können nichtklassische Zustände erzeugt werden, welche ein Grundbaustein von quantenmechanischen Gattern und Algorithmen sind. Diese umfangreiche optische Schnittstelle ermöglichte es den Ionenfallen-Experimenten die führende Rolle auf dem Gebiet der experimentellen Quanteninformationsverarbeitung einzunehmen.

Diese Arbeit behandelt zwei Fragestellungen auf dem Gebiet der Mikrofallen Quantenoptik. Die Abhängigkeit der Heizrate von der Oberflächentemperatur der Falle wurde in einem neuen experimentellen Aufbau untersucht. Die ersten Messergebnisse in dem kryogenen 3D Mikrofallen Aufbau bilden den Grundstein für zukünftige Messungen. Des Weiteren bieten segmentierte Fallen mit ihren Kontrollelektroden ein starkes Stellglied für die Manipulation externer Freiheitsgrade. Die transportbasierte Quanteninformationsverarbeitung basiert auf einer Vielzahl von Transport, Trenn- und Vereinigungsoperationen von Ionenkristallen, während optische Operationen auf kleinen Kristallen durchgeführt werden. In dieser Arbeit wurde mit dem nichtadiabatischen Transporten einzelner Ionen auf der Zeitskala der Fallenperiode ein Grundbaustein für dieses Schema realisiert. Ein experimenteller Höhepunkt dieser Arbeit ist die Realisierung von Grundzustandstransporten auf der Zeitskala der Fallenperiode mit vernachlässigbarem Energiezuwachs [WZR+12]. Hierfür war die Entwicklung einer rauscharmen Spannungsquelle für die Versorgung segmentierter Mikroionenfallen ausschlaggebend. Spannungsrampen mit einer Rate von 2.5 MSample/s auf bis zu 12 Kanälen ermöglichen die direkte Manipulation des Quantenzustands mittels elektrischer Felder. Dies führte zur ersten experimentellen Realisierung von „displaced number states“ in Ionenfallen [ZRW+12].

Summary

The outstanding degree of control over trapped ions in Paul traps gives rise to the development of novel quantum manipulation techniques. Optical transitions can be used for precise manipulation of internal and external states. This way, non-classical states can be created which are a key component of quantum algorithms based on quantum logic operations. This powerful optical toolbox enabled the trapped ion system to assume leadership in the field of quantum computation.

This thesis addresses two major challenges in the field of micro ion trap quantum optics. The temperature dependence of the heating rate from the ion trap surface is analysed in a novel cryogenic micro ion trap. Furthermore segmented traps allow state manipulations by time dependent electrical potentials, generated by the control voltages. These electrical fields provide a fast and reliable control handle to the ions external degrees of freedom. Quantum computation in Paul trap arrays is based on a combination of ion crystal transport, splitting and merging operations, while laser driven quantum state manipulations are mainly carried out on small ion crystals. Within this thesis a basic building block was realised by performing transport operations with a single ground-state cooled ion. As a highlight of experimental achievements, shuttling in the non-adiabatic regime, on the timescale of the motional period was demonstrated with low residual energy transfer [WZR$^+$12]. For his endeavour a specialised low noise arbitrary function generator was designed and manufactured during this thesis. Arbitrary voltage ramps at a sampling rate of up to 2.5 MSample/s on up to 12 channels allow the study of a novel excitation method by directly manipulating the ion using electrical forces. Accurate numerical simulations in combination with the fast high resolution voltage supply allow deterministic quantum manipulations via momentum kicks. I report the first experimental demonstration of displaced number states with trapped ions [ZRW$^+$12].

Contents

1. Introduction **1**

2. Segmented Ion Trap Experiments **3**
2.1. Segmented Linear Micro Paul Trap 3
2.2. Vacuum Apparatus 8
2.3. Laser Setup 16
2.4. Fast Voltage Control Hardware as Ion Interface 23
2.5. Experiment Computer Control 32

3. Simulation of Static Electic Fields and Ion Dynamics in Time Dependent Potentials **37**
3.1. Segmented Micro Paul traps 37
3.2. Numerical Electric Field Simulation 39
3.3. Axial DC Potentials 41
3.4. Radial RF Potentials 43
3.5. Dynamic Trajectory Simulation 44
3.6. Transport Voltage Determination Using Singular Value Decompsition . 47
3.7. Simplified Scheme for Concatenated Transport Operations 51

4. Qubit Implementation and Development of a Universal Toolbox of Operations **53**
4.1. Trapping, Initialization and State Detection of Ions 53
4.2. Internal State Manipulation 59
4.3. Energy and Phonon Distribution Measurement 63

5. Coherence Measurement and Testinig of Decoherence Processes **69**
5.1. Motional Heating Rate 69
5.2. Heating Rate Dependency from Trap Surface Temperature 71
5.3. Ramsey Experiments 73
5.4. Fock State Thermalisation 75

6. Transport Operations in Segmented Ion Traps for Sensing Electric and Magnetic Fields **79**
6.1. Adiabatic Transport Operations 80

6.2. Electronic Motional Excitation and Generation of Displaced Number States 86
6.3. Ultra Fast Transports Without Excitation as Architecture Building Block for Quantum Computing 90

7. Conclusion and Outlook **97**

A. Acronyms **99**

B. Quantum Optics Laboratory Design **103**

C. Lab Parameter Sheet **109**

D. Publications **111**
D.1. Peer reviewed journal publications 111
D.2. Peer reviewed journal publications from earlier work 112
D.3. Talks 112
D.4. Posters 112

E. Bibliography **113**

F. Acknowledgements **117**

List of Figures

2.1. Micro structured linear Paul trap design 4
2.2. Fibre cavity implementation 6
2.3. Vacuum setup 9
2.4. Laser beam lines 10
2.5. Vacuum setup with cryostat 11
2.6. Cryogenic ion trap 12
2.7. Cryostat operation 14
2.8. Cryostat operation using liquid Nitrogen 15
2.9. 397 nm laser setup 17
2.10. 866 nm and 854 nm laser setup 18
2.11. Spectroscopy laser setup 19
2.12. Frequency measurement and stabilisation setup 20
2.13. Laser ion interface 21
2.14. Detection setup 22
2.15. Multiple arbitrary function generator setup 24
2.16. Digital to analog converter circuit 25
2.17. Digital to analog converter board 26
2.18. Low noise battery power supply 27
2.19. Power line trigger 28
2.20. USB-FIFO interface wiring 29
2.21. Long term ADC measurement 31
2.22. Linearity of the DAC output 33
2.23. Experiment control setup sketch 34

3.1. Simulation trap model 40
3.2. All DC potentials 41
3.3. Three potentials with field and curvature 42
3.4. Ponderomotive potential 43
3.5. Ion trajectory and Fourier transformation 44
3.6. Secular motion angle dependence 45
3.7. Secular motion tilt variation 46
3.8. Ponderomotive potential in a planar ion trap 49
3.9. Transport segment voltages 50

3.10. General transport voltage function 52

4.1. Calcium level scheme 54
4.2. Measured two dimensional fluorescence spectrum 56
4.3. Fluorescence histogram 57
4.4. Measurement sequence 58
4.5. Harmonic oscillator ion states 60
4.6. $D_{5/2}$-State spectrum with motional sidebands 61
4.7. $D_{5/2}$ state Rabi oscillations 62
4.8. Transition matrix elements 64
4.9. Rabi Oscillations for a near ground-state cooled ion 64
4.10. Rising slope method 65
4.11. Coherent state analysis 67
4.12. Pseudo Energy 68

5.1. Heating rate measurements 70
5.2. Electrical field noise density temperature dependence 72
5.3. Ramsey measurement sequence 73
5.4. Ramsey analysis of $S_{1/2}\ m_j = 1/2 \rightarrow D_{5/2}\ m_j = +5/2$ transition 74
5.5. Ramsey contrast improvement 75
5.6. Fock state thermalisation 76
5.7. Fock state thermalisation 77

6.1. Remote spectroscopy scheme 81
6.2. Remote electric field probe 82
6.3. Magnetic field gradient measurement 84
6.4. Electric stray fields in planar trap 85
6.5. Coherent excitation scheme 87
6.6. Asymmetric coherent excitation 88
6.7. Symmetric electric excitation measurement 89
6.8. Displaced Fock States 90
6.9. Transport operations 91
6.10. Pairwise neutral transport 92
6.11. Self-neutral transport 93
6.12. Ramsey singal of ground state and spin-motion entangled state 94
6.13. Motional frequency deviation 95

B.1. Sketch of Lab design 104
B.2. Quantum optics laboratory 105
B.3. Laser setup 107

1 Introduction

Since the first idea of *atoms* as basic building block of matter, in the late 18th century, the ambition for better understanding of our world lead through several milestones in research history. A new research field was born around the understanding of atoms. The science of *chemistry* lead to various elements and the study of reactions. It took another century until first effects arising from the inner structure was measured. The discovery of the electron in the 1897 by J. J. Thomson contributed to the development of a realistic atom picture. The formulation of simple models lead to a better understanding and more specialised experimental apparatuses, responding open questions. A. Einstein described the *photoelectric effect* by interpreting light as quantised particles, the photons in 1905 (Nobelprize in 1921). This was based on the idea of M. Planck, who discovered the energy relation $E = h\nu$ and set the basis for the light-atom interaction awarded with the Nobelprize in 1918. During the year 1913, N. Bohr formulated his idea of electrons populating discrete orbits around the atom core. The discrete transitions of electrons between different orbits had to be realised by the absorption or emission of photons. His work was awarded with the Nobelprize in 1922. E. Schrödinger developed his idea of *wave equations* to describe the evolution of a quantum system (Nobelprize 1933). Followed by the *uncertainty relation* by W. Heisenberg this provided the basis for the mathematical description of quantum mechanics (Nobelprize 1932). The early quantum physics was developed by Einstein, Bohr, Heisenberg and Schrödinger among others in the first half of the 20th century. The picture of a single atoms changed over these years from the building block of matter to a novel interesting system with strange properties. The famous statement from Schrödinger 1952, that "we never experiment with just one electron or atom or (small) molecule" was proven wrong only 35 years

later. The direct observation of single atoms in free space was shown in the first ion trap experiments [DW87]. This lead to the new experimental field of quantum optics, where isolated quantum systems can be manipulated with laser light on there optical transitions. This experimental work has been awarded with the Nobelprize for D. Wineland and S. Haroche in 2012.

Using various versions of the initial 3D Paul trap multiple achievements have been reached during the last decades. The resulting limitation is the scalability of these ion trap experiments. The research field of quantum computation and quantum simulation evolved in recent years towards microscopic segmented ion traps. The possibilities for a scalable quantum computation unit led towards further development of these *micro ion traps*. The evolved production techniques allow the manufacturing of advanced 3D trap geometries and planar trap structures using lithographic production methods. On the long run these traps will become smaller with increasing amount of trap electrodes to store and operate a rising number of qubits. The big advantage of multiple electrodes is the possible combination of the powerful optical quantum operations and the direct manipulation by electric fields. The system gains scalability due to possible transport operations allowing to control the amount of interacting qubits. A sequence of ion crystal splitting and merging operations in combination with optical gates allow the interaction of a large qubit number. This transport based quantum computation scheme was proposed by Kieplinski [KMW02] and several research groups aim for this architecture.

This approach requires a microstructured ion trap design with a high number of control electrodes. In fact each control electrode is able to form an individual trapping potential and store an ion crystal. Due to the miniaturisation of the ion traps further challenges arise. The closer ion-electrode distance results in higher decoherence rates due to the trap heating rate. This problem is addressed by cryogenic cooling, which is able to reduce certain heating effects. The other challenge arises from the higher sensitivity to applied control voltage, also due to the closer ion-electrode distance. This requires a low noise voltage source supplying the control electrodes.

2

Segmented Ion Trap Experiments

This chapter explains the experimental setup with all components necessary for performing quantum optics experiments with trapped ions. First we will take a closer look on how to manufacture and assemble ion traps in section 2.1. The required vacuum setup is discussed in section 2.2 with focus on the implementation of a cryostat cooling system. Section 2.3 treats the required laser setup with all components for laser frequency stabilisation and modulation as well as the creation of fast laser pulse sequences. The fast ion trap voltage supply is described in section 2.4 with a variety of peripheral components to realize fast transport operations on trapped ions. The general design of an optics laboratory is described in section B.

2.1. Segmented Linear Micro Paul Trap

The trap geometry and manufacturing process was designed and developed by S. Schulz [Sch09] and will only be outlined here. The trap consists of two electrode layers separated by one insulation layer. The base material of this sandwich structure is Alumina[1] with gold coated electrode structures. The surface structuring is done by femtosecond laser micromachining[2]. The manufacturing process consists of several steps which are chosen to realize the desired geometry as precise as possible.

[1] 125 μm thick 1 inch waver, Reinhardt Microtech AG, Wangs, Switzerland
[2] Micreon GmbH, Hannover, Germany

1. Structuring plain ceramic wafer with 'finger' geometry using femtosecond laser micromachining
2. Performing gold coating of whole wafer surface using gold sputtering
3. Separating electrodes by removing lines of gold with femtosecond laser micromachining
4. Dicing the trap chips from the whole wafer using femtosecond laser micromachining

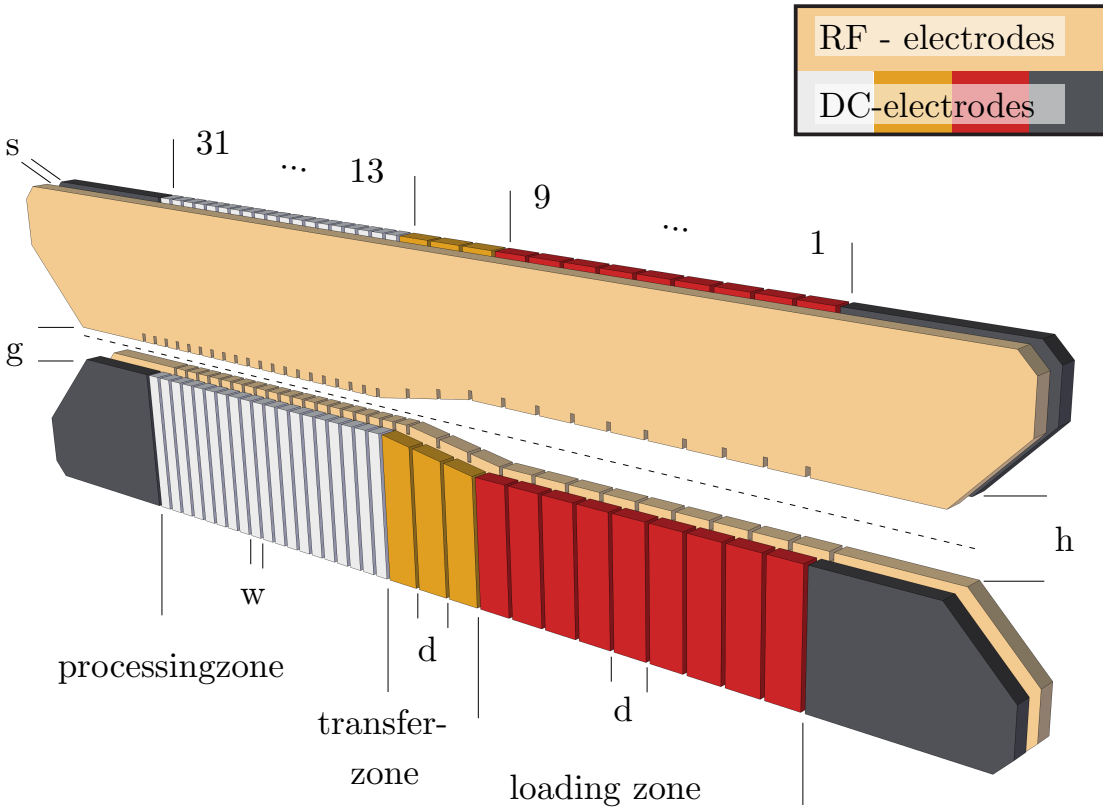

Figure 2.1.: Micro structured linear Paul trap design: [Sch09] The relevant conductive parts of the used ion trap design including DC-segment numbering. The separation of the two conductive layers is similar to their height s=125 μm. The slit size is h=500 μm in the loading zone and g=250 μm in the processing zone. The width of the DC-segments is reduced from d=250 μm in the loading zone to w=125 μm in the processing zone.

Figure 2.1 shows the geometry which is optimized to achieve similar direct current (DC) potential values from one segment in the loading zone and one segment in the processing zone, which is also shown in figure 3.2. The different regions allow for i) change the ion

electron distance within one trap, ii) increase the segment number for complex transport operations and iii) transport ions in a smaller trap structure where initial trapping is difficult. A Further advantage is that the contamination from the calcium (Ca) oven is restricted to the loading zone. A detailed description of the physical operation principle can be found in chapter 3.

2.1.1. Implementation of a Fibre Optical Resonator

The combination of Paul traps and optical resonator allows experiments in the field of cavity quantum electrodynamics. Our approach is to integrate a fibre optical resonator [Hun05, Deu08, Het09] into a micro structured Paul trap. By using cavity fibres with a diameter of 125 μm the trap design changes are minimal. It is sufficient to change the design of the alumina spacer layer and keep the two electrode layers unchanged. The spacer is separated in two parts to form a guidance channel for the fibres. This channel is designed to be located far in the processing zone to prevent charging effects due to ultra violet (UV) light. This is mainly used in the loading zone where all visible surfaces are covered with conductive material. Furthermore the fibre channel is designed with a 7 $^\circ$ tilt to the trap axis. This creates tilted cavity modes inside the ion trap and enables the possibility of scanning the ions position over several cavity modes influencing the coupling strength. For scanning and locking of the fibre cavity a stack shear piezo is attached to one fibre.

The fibre trap assembly process is quite complex consists mainly of these steps:

1. Cleaning of all trap parts. This includes a bath in strong solvents like Aceton and ultrasonic cleaning if the trap geometry is stable enough to prevent structural damage.

2. Align the bottom layer to the larger ceramic spacer piece using the alignment holes. The accuracy of this step determines the exact position of the fibre cavity which is guided by this part. The spacer part is glued through the bottom layer using UV adhesive glue[3].

3. A spare piece of fibre can now be placed from the top side at its desired location shown in figure 2.2a). The second part of the spacer is now aligned using a microscope. It is placed flat on the bottom layer and pressed slightly towards the fibre piece. This working step realises the guidance channel consisting out of the two spacer parts from left and right and the bottom layer from below. The smaller spacer part is fixed from the top side using UV adhesive glue. The glue position must be chosen not to disturb the top electrode layer which will be placed in the next step.

[3]Epo-Tek OG142-13, Polytec PT GmbH, Waldbronn, Germany

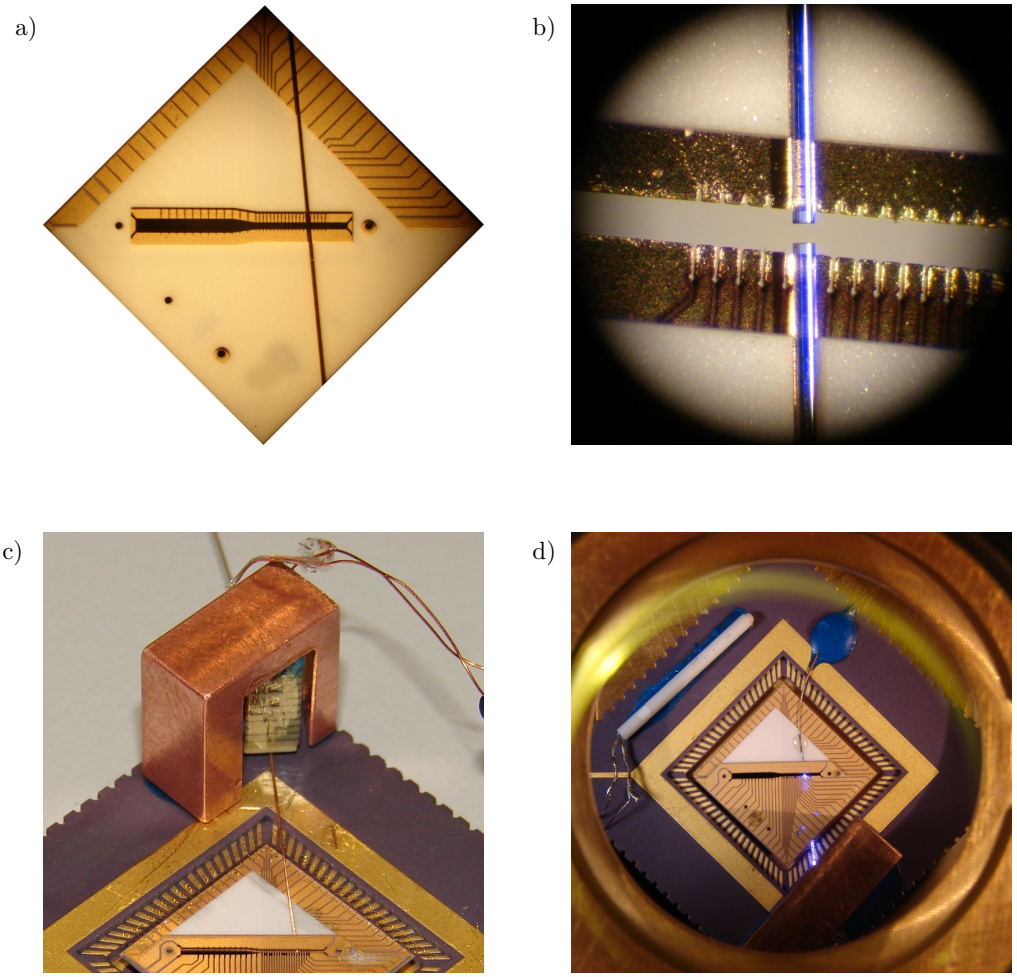

Figure 2.2.: Fibre cavity implementation: The sandwich structure allows to embed a fibre optical resonator within the spacer layer. a) shows the slit in the spacer ceramics before final assembly of the top electrode layer. In b) the centre region with both fibre tips is magnified. The piezo motorized fibre attachment is shown in c) with a stack shear piezo and d) shows the completely installed fibre cavity trap inside the vacuum chamber with IR light coupled in (blue lumminescence due to CCD bandpass coating). The white temperature sensor was used to observe the thermal behaviour of this test trap.

4. To install the fibre cavity the trap height inside the ceramic chip carrier array must be adjusted properly. Doing so a copper spacer frame is glued inside the chip carrier using thermal conductive glue[4]. The same glue is used to attach the bottom layer of the trap and the two spacer parts inside the chip carrier. The bottom electrodes are now connected to the chip carrier using wire bonding.

5. The Installation of the fibre optical resonator required active resonance tracking while assembly and consists of multiple steps:

   - The shear piezo drive[5] for scanning the cavity length has to be attached to its copper holder using the thermal conductive glue[6], visible in figure 2.2c).
   - Afterwards one cavity fibre can be attached to the bottom of the piezo actuator using UV adhesive glue[7] with the desired length. The assemblage of fibre, piezo and copper holder is attached to a six axis micrometer manipulator stage for alignment.
   - The second fibre is attached to micrometer manipulators and used in to align the resonator inside the trap. The resonance peak is observed while scanning the cavity length during assembly. A suitable laser source and additional electronic equipment, like triangle voltage generator, high voltage amplifier, photodiode and oscilloscope is required during the installation. In figure 2.2b) the final positioning of the cavity inside the trap is shown.
   - After the cavity is adjusted inside its guidance channel the top electrode layer is aligned using the DC electrode geometry and attached using UV adhesive glue through the holes to the spacer layers. It is important that not too much pressure is applied to not lock the fibre and preventing further scanning.
   - The copper piezo holder is glued using thermal conductive glue to the chip carrier. While the curing time of the glue slight position corrections of the cavity are necessary. Figure 2.2c) shows the final position of the piezo holder.

6. The final assembly step is to connect the top electrodes using wire bonding to the chip carrier and connect the chip carrier contacts to the low pass filter board using electric conductive glue[8]. In figure 2.2d) an assembled test trap is shown inside the radiation shields in vacuum. This trap and the visible temperature sensor[9] is used to test the cavity operation in cryogenic environment. The luminescent optical fibre shows the diffraction of infrared light in the fibre.

[4] DeltaBOND 152,Cast-Coat Inc., W. Bridgewater, USA
[5] P-111.05 (UHV,Cryo,AL2O3 end plate and Ta electrode), PI Ceramic GmbH, Lederhose, Germany
[6] DeltaBOND 152,Cast-Coat Inc., W. Bridgewater, USA
[7] Epo-Tek OG142-13, Polytec PT GmbH, Waldbronn, Germany
[8] EPO-TEK H20E, EPOXY TECHNOLOGY INC., Billerica, USA
[9] PT100

This combination of cryogenic micro ion trap and fibre optical resonator was operated for multiple months and it was possible to perform several experiments. The operation of the fibre cavity is possible while trapping ions in the loading zone. Unfortunately has the conductive coating of one fibre not been removed completely. A thin layer of carbon produced a strong asymmetric power dissipation from the radio frequency (RF) drive electrodes. This electrical problems lead to a strongly distorted radial potential and no transport to the cavity or ground state cooling was possible. This trap was replaced by a basic version without cavity at a later stage.

2.2. Vacuum Apparatus

To operate an ion trap, a ultra high vacuum (UHV) environment is necessary to minimize interaction with background gas. This is realized using a custom made conflat (CF) vacuum chamber with commercial vacuum pumps. Figure 2.3 shows the design and all relevant vacuum parts. The vacuum pressure measurement is done by a ionization gauge[10]. The ion getter pump[11] and the titanium sublimation pump (TSP)[12] are necessary to preserve ultra high vacuum ($3 \cdot 10^{-11}$ mbar at room temperature operation) without acoustic noise. The vacuum pumps and the valve[13] are mounted at the opposite site of the imaging optics and have direct connection to the main chamber which includes the ion trap. This short way with large cross section achieve high pumping power in the main chamber.

During one week of bakeout at 180 °C several cleaning operations have been performed in various instruments with a external vacuum pump connected. To obtain more information about the bakeout process and the status of the different instruments a commercial quadrupole mass spectrometer[14] was connected to the pumping stage. The main pollution sources are the Ca oven which gathers a lot of water and the ion getter pump which gathers many different gases. The oven was operated at 2.7 A for half an hour to remove the water. This has to be repeated multiple times during the bakeout process until there is no water peak in the mass spectrometer during oven operation. The ion getter pump should be switched on and off in short intervals for approximately 100 times during the whole time of bakeout. The pressure gauge was two times switched to “DEGAS” during bakeout. The TSP was ignited once a day on all filaments with increasing current. The maximum current was set to 30 A with a sublimation time of 1 minute. Each cleaning process sets free some contamination agents which then are partly removed through the pumping stage. The remaining part sticks the most to gettering surfaces like the ion getter pump. The concentration at certain instruments is

[10] UHV-24p, Agilent Technologies, Frankfurt, Germany (former VARIAN GMBH)
[11] DN63 Vaclon Plus 55 StarCell, Agilent Technologies, Frankfurt, Germany (former VARIAN GMBH)
[12] DN35 TSP,Vacom, Jena, Germany
[13] DN63 UHV – All Metal Angle Valve, VAT, Haag, Switzerland
[14] Restgasanalysator Serie LC-D,Vacom, Jena, Germany

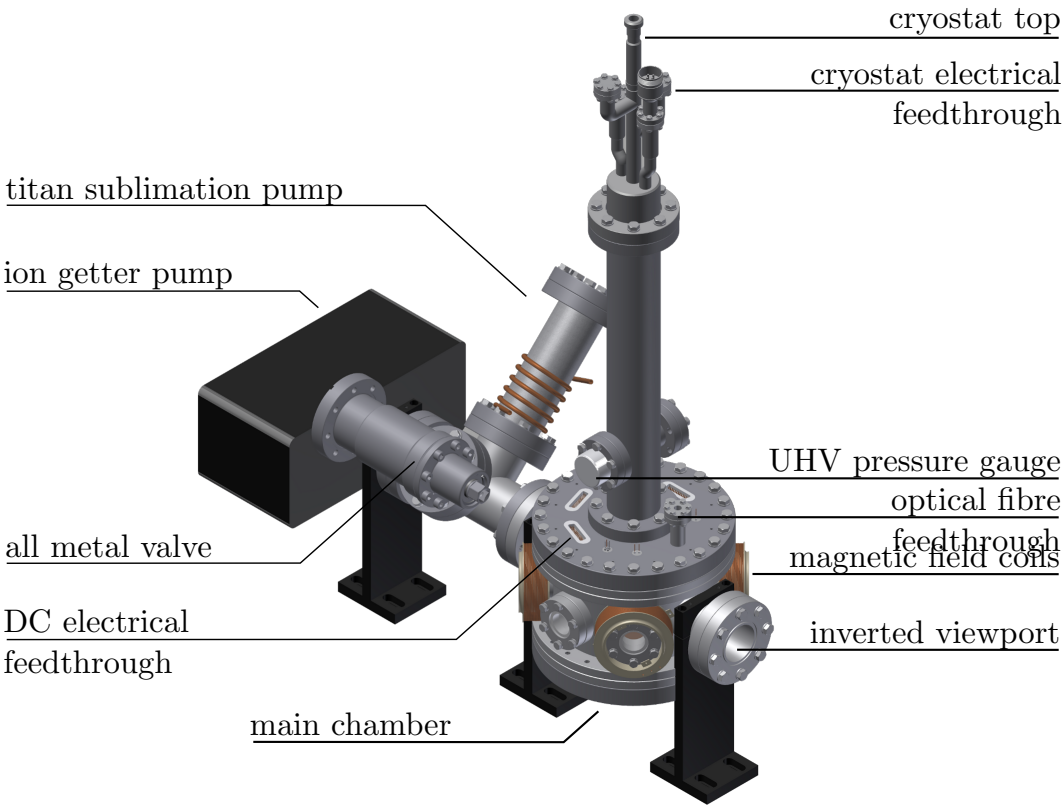

Figure 2.3.: Vacuum setup: The main chamber preserves optical access to the ion trap while the vacuum pumping section is attached at its rear part. The cryostat is mounted on top of the main chamber and its cold finger permeates down to the main chamber. Top flange all electrical connections for operation of the ion trap are fed through.

dependent from the affinity to specific contamination. The strong hydrophilicity of calcium for example leads to the fact that water returns or redistributes in the oven which makes multiple oven operations necessary. All electronic connections are fed through the top flange of the main chamber including 84 analog DC lines, the radio frequency lines for the trap electrodes, as well as the current supply for the calcium oven and the voltage supply for the shift piezo of the fibre cavity. The used viewports are anti reflection coated to reach a maximum transparency at 397 nm.

The main chamber is an octagon ring with six CF35 flanges for laser beam access and two CF63 flanges for pumping and imaging optics access. A sketch of all laser beam lines is shown in figure 2.4. The general idea behind the separation to different viewports is guided by physical requirements and practical optimisation constrains like stray light reduction. The laser at 423 nm is used for photo ionization and for neutral fluorescence detection, therefore it is sent in at the side adjacent to the imaging optics. Like this

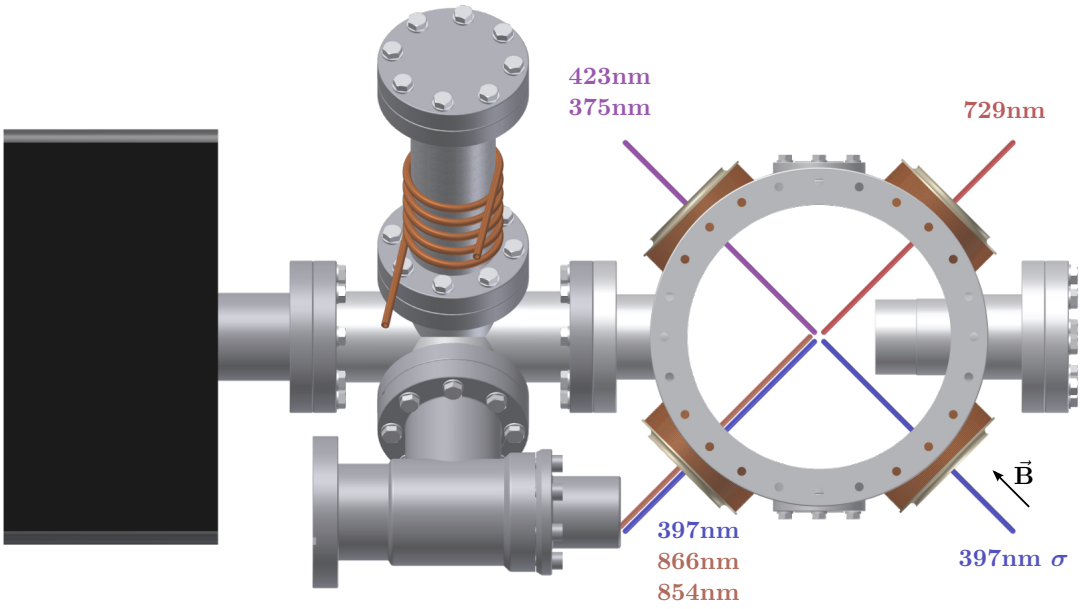

Figure 2.4.: Laser beam lines: Top view of the main vacuum chamber with transparent top flange and cryostat. The different laser beam directions are sketched in addition to the direction of the quantisation magnetic field.

the micro trap operates as pin hole and shields stray light from laser beam. The most important lasers for trapping, cooling and detection are the Doppler cool laser at 397 nm and it is repump lasers at 866 nm and 854 nm. These lasers are precisely overlapped in front of the viewport and irradiated together to the ion. Because the laser at 397 nm is switched on during detection it has to enter the chamber at the opposite side of the detection. Furthermore the polarisation of the Doppler cooling laser must not be circular. The 397 nm σ beam must be aligned along the magnetic field to perform optical pumping. Furthermore this laser is not switched on during detection, thus it can enter the apparatus from the imaging optics side. Same holds for the 729 nm beam, where the angle of 45 ° to the trap axis enables the possibility to drive axial and radial sideband transitions. Furthermore its angle to the magnetic field enables to drive the required Δm transitions for sideband cooling[NHTD78].

2.2.1. Cryostat Implementation

The continuous flow cryostat[15] is already optimized to be implemented in UHV chambers. A detailed picture of the inner construction is shown in figure 2.5. The basic

[15]ST-400 UHV, Janis Research Company, Wilmington USA

function principle is that a cold liquified gas is inserted close to the bottom of the cold finger using a cryogenic transfer line. The liquid gas reaches the inside of the cold finger and evaporates at thermal contact. The gas is fed out through a double walled tube and exits the chamber through the vent port. This leads to a temperature gradient from the cold finger towards the mounting flange close to the top of the cryostat. Along this gradient it is possible to attach a second radiation shield with an intermediate temperature. Dependet from the actual position the outer radiation shield has a temperature of approximately 20 % warmer than the cold finger. The inner radiation

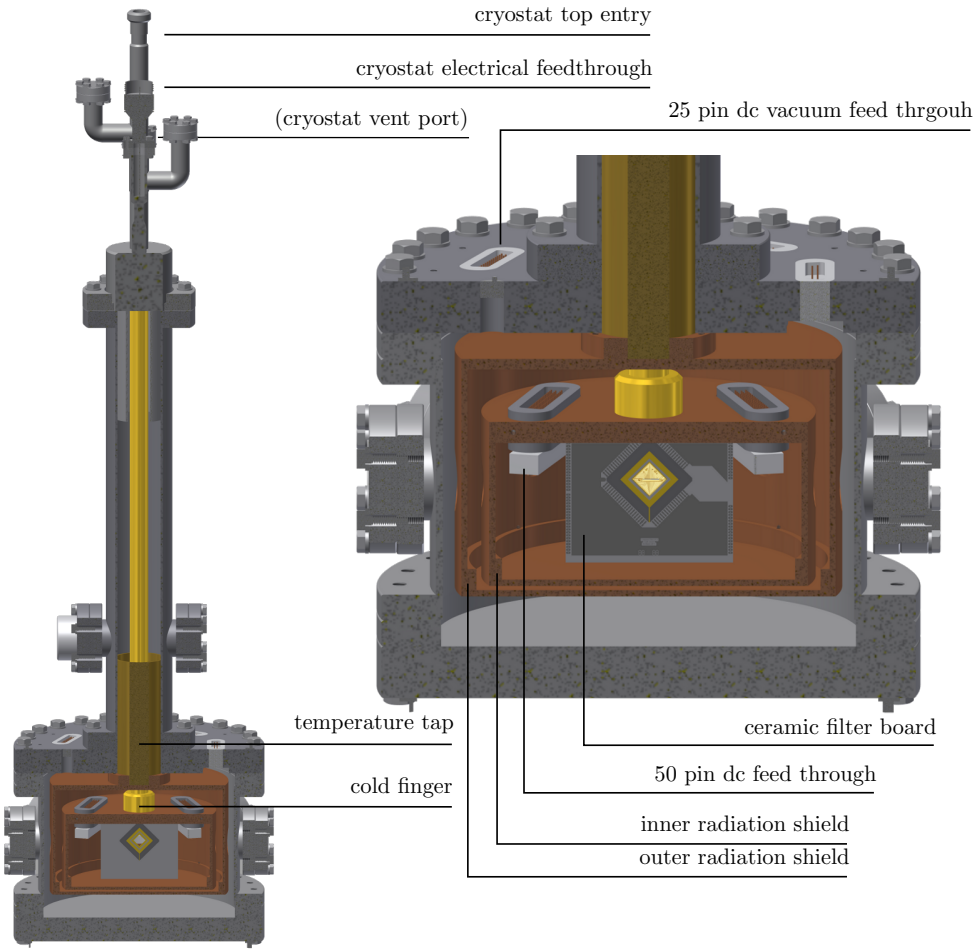

Figure 2.5.: Vacuum setup with cryostat: These cuts through the vacuum chamber illustrate the cryostat design. The ion trap and it is surrounding radiation shield are hanging at the gold coated cold finger of the cryostat. The cryostat vent port on the back side of the setup is not visible in this view.

shield is directly attached to the cold finger and thermalizes to the minimum reachable

temperature. The base plate of this shield is used to attach the ion trap setup. The electrical contacts are fed from the low pass filter board over 50 pin D-Sub connectors through the inner radiation shield. All DC connections are also fed through holes in the outer radiation shield. Finally they are fed through four 25 pin D-Sub feedthroughs out of the vacuum chamber. Both radiation shields are manufactured from oxygen free copper using soldering and milling.

The high mass at the end of the coldfinger leads to strong mechanical vibrations in the low Hertz regime. In a later stage of the experiment a vibration damping tool was added to the cryostat design. It consists of a linear manipulator with a Teflon tip pushing against the inner radiation shield. Like this the coldfinger is bent and vibrations are inhibited by the friction between the tip and the copper shield.

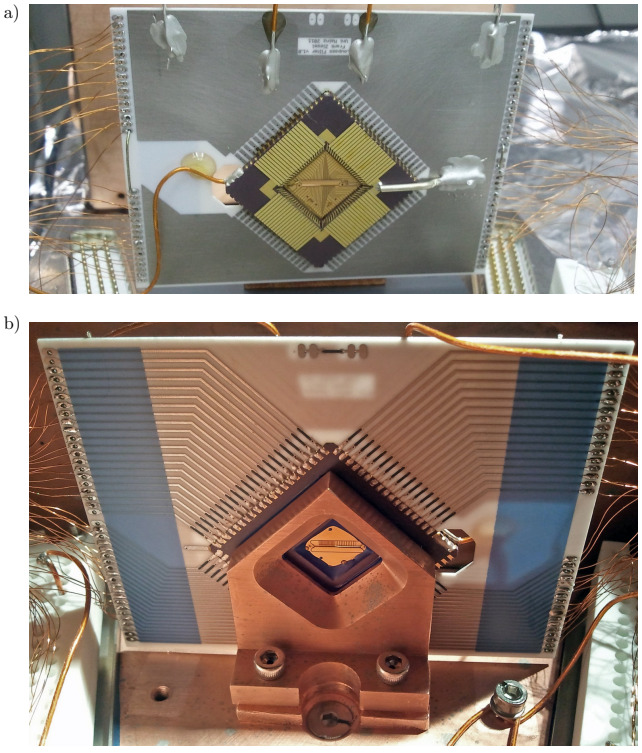

Figure 2.6.: Cryogenic ion trap: In a) the ion trap is pictured inside it is chip carrier with final assembly of the ceramic capacitor arrays and all connections to the surrounding filter board. The large connection from the filter board to the ground plane of the filter board is also visible. In the rear view of b) the black 50 Ohm resistors on the filter board and the individual dc lines are shown. This picture shows the final assembled trap inside with its holder inside the radiation shield.

The ion trap is mounted on an oxygen free copper holder to the inner radiation shield. In figure 2.6b) the rear view of the final mounted ion trap is shown. The trap holder is mounted with some height adjustment to the radiation shield, which is mounted directly to the cold finger. One clearly recognizes the enclosing ceramic filter board with DC connection wires. The filter board is produced using hybrid thick film technologies[16] and is UHV compatible. On the front view, figure 2.6a) the capacitor arrays are visible on top of the chip carrier. The common contact of these arrays is connected, using reflow paste, to the ground ring on top of the chip carrier. The individual contacts are connected via wire bonding to the individual DC electrodes. Together with the resistors they form a low pass with a cut off frequency of 5 MHz. One crucial point in wiring low DC and RF electrodes is the low impedance of the ground connections. The drive circuit of the radio frequency voltage must have good ground connections to the vacuum chamber and the radiation shield to ensure a defined capacitance. Furthermore the ground connection must be good at the capacitor arrays to allow compensation currents to flow. In this setup the general mass point is chosen close to the ion trap. From the ground ring on the chip carrier all ground connections are fed in a star-shaped manner to the radiation shields, the vacuum chamber, the RF drive circuit and the DC drive.

2.2.2. Cryostat Operation

A sketch of all cryostat relevant components is shown in figure 2.7. Operating with liquid Helium a minimum temperature of 4 K can be reached. The cooling power can be adjusted using the flow rate of the liquid gas and reaches values up to several watts, according the specification. For transport and storage of the liquid gas a suitable cryogenic dewar is used. The flow regulation is done by two control elements: A needle valve at the cryogen entry at the end of transfer line inside the dewar shown in figure 2.7. It regulates the cross section over which the liquid flows. The other control parameter is the pressure inside the dewar which is regulated by dewar heating and an over-pressure valve. The cryogen gas flows through the transfer line to the very bottom of the cryostat where it leaves on the inside of the coldfinger. This thermal contact cooles the crostat. The vaporized gas leaves the setup via the gas exhaust and is lead through a digital mass flow meter[17] is used to detect the flow.

A 50 Ohm resistor inside the cryostat is used to regulate the temperature with a stability better than 50 mK. The temperature measurement is done by a 4-point measurement of a silicon diode located at the bottom of the cold finger. The proportional-integral-derivative (PID) regulation works in both directions if the heater is operated with offset load. The electronic connections for heater and temperature sensor are winding around the inner cryostate tube (figure 2.7, highlithed red) which can be removed for

[16] Hybrid-Dickschichtelektronik, Dieter Gebauer, University Siegen, Germany
[17] EL-Flow F111B, Bronkhorst,AK Ruurlo, NL

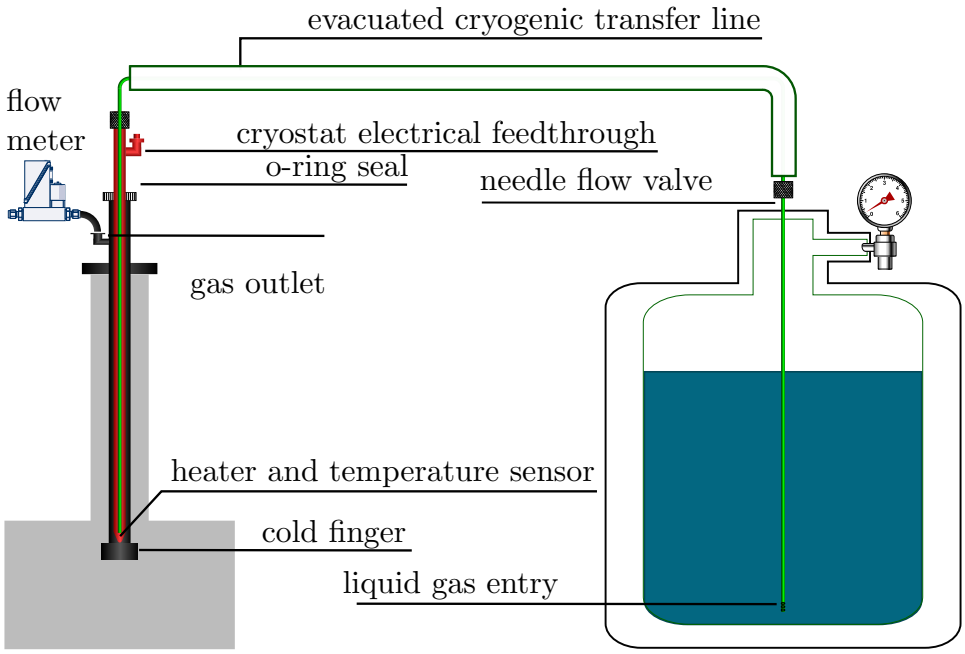

Figure 2.7.: Cryostat operation: The left side shows the inner design of the flow through cryostat. The actual cryostat highlighted in red. This part can be removed with all functional components for maintanance. It is mounted in the black stainless steel vacuum tube which has a gold coated copper part at the cold finger. The green transfer line enters until the very bottom to supply the liquid gas. The gas is pressed through the transfer line via applied pressure in the supply can and holes at the bottom of the can.

maintanence without breaking the vacuum. The heat transfer to the UHV part of the cryostat is realised by a cone inside the coldfinger to ensure optimal heat transfer.

To cover the temperature range from room temperature down to 77 K the use of liquid nitrogen is recommended. It is more economic compared to helium and its heat capacity is much higher. The nitrogen transport container[18] has a capacity of 250 l and enables the continuos operation for approximatly one month as shown in figure 2.8. The average liquid consumption of 5.8 ml/min is higher than the specified 1.6 ml/min but it was not optimized for minimum comsumption. For continuous operation the pressure in the container and the needle valve must kept fix. The thermal setup contraction is not only dependent from the operation temperature but also from the cryogen flow. For operation down to 77K a constant gas flow less then 3 l/min is enough. The unstable temperature for the low temperature range in figure 2.8 results from wrong PID regu-

[18] CS 250 SK, Cryo Anlagenbau, Wilnsdorf

lation parameters of the temperature regulation. This parameters have to be adjusted to the actual flow and the operation temperature.

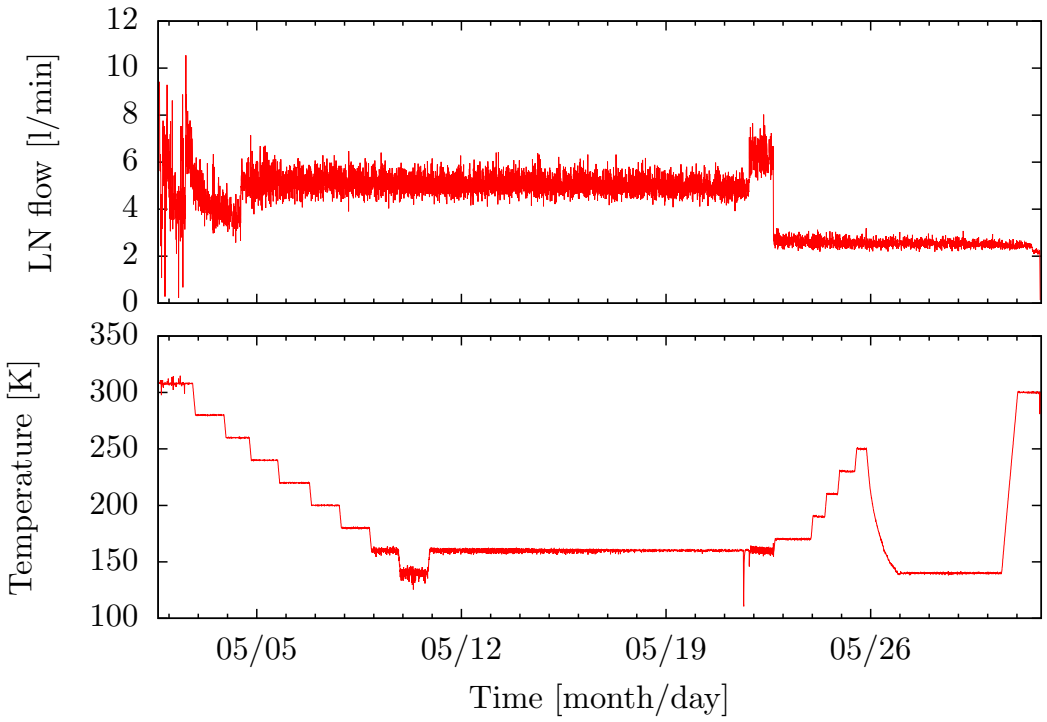

Figure 2.8.: Cryostat operation using liquid Nitrogen: The continuous operation over $\approx$ 1 month with 16 different temperature steps observing the nitrogen gas flow and the coldfinger temperature.

During operation with liquid Helium the gas exhaust leads through the gas flow meter and continues to the Helium recouvery system for being liquified in the building basement. A cryogen transport container with 67 l liquid Helium was used for operation of down to 40 K during 4 days. This results in an average consumtion of 11.6 ml/min liquid gas. The specified consumtion of 8 ml/min was not achieved because of the stability requirements of the system. The pressure generation of the Helium container occures due to gas heating of the transfer line. The Helium setup has no over pressure regulation connected to the recouvery system and the only pressure reducing part is the needle valve opening. This is why the setup had to be operated with incerased Helium flow. The cryostats cooling power is sufficient enough to reach liquid Helium temperatures while operating the ion trap.

The thermal contraction of the cryostat was determined by logging the laser stage positions during operaiton at various temperatures. Operating at a constant nitrogen

gas flow of 4.5 ml/min a contraction of 6.0(3) μm/K was measured using all laser stage positions. This value enables an experiment operation in the full temperature range from 4 K till 300 K where the ion is always in the camera field of view and accessable by al laser beams. In this temperature range the ion would be shifted by 1.77(8) mm in total.

2.3. Laser Setup

To create 1 μs resolved laser pulse sequences each beam is switched by acousto optical modulators (AOMs). This allows fast switching and the creation of laser pulse sequences of all relevant laser sources. A wavelength meter[19] including eight channel switcher box is placed on the optical table and is used to monitor the laser frequencies with an accuracy of better than 10 MHz. All relevant lasers are stabilized using a Pound-Drever-Hall (PDH) frequency stabilisation. The necessary cavity and optics to create the regulation signals are placed on the optical table as well as described in section 2.3.4.

2.3.1. Laser System for Fluorescence Excitation, Doppler Cooling and Optical Pumping

The laser source is a TA SHG[20] which includes an infrared laser diode as light source, a tapered amplifier and a second harmonic generation (SHG) cavity for frequency doubling. The full setup is shown in figure 2.9. The laser light from the diode is guided through a Faraday insulator to prevent lasing disturbance through back reflexes. A small part of the infrared beam is extracted to supply the wavelength meter and the optical cavity for stabilisation. The larger part of the light is guided through an optical amplifier. After passing an additional protection Faraday insulator the light is coupled into the doubling cavity. The SHG crystal creates a frequency doubled laser light at 397 nm. The doubling cavity must be locked to the master laser to realize continuous and intensity stable blue laser light. More details to the stabilisation can be found in section 2.3.4. The blue light exits the laser and is redirected using a dichroic mirror to remove infrared laser power from the beam path. An adjustable prism pair corrects the beam elliptic profile and a telescope creates a collimated beam with approximately 1 $\mathrm{mm_{FWHM}}$ diameter. All electronic components required for supplying and switching the AOMs[21] are mounted on a separate copper drawer below the optical table. The copper plate is used as ground plane and for additional cooling of the amplifiers. The drive Frequency of 80 MHz is created by a voltage controlled oscillator and adjusted to

[19] HF-ANGSTROM WS/U-30U, HighFinesse GmbH, Tübingen, Germany
[20] TOPTICA Photonics AG, Munich, Germany
[21] BRI-QZF-80-20, Brimrose, Sparks, USA

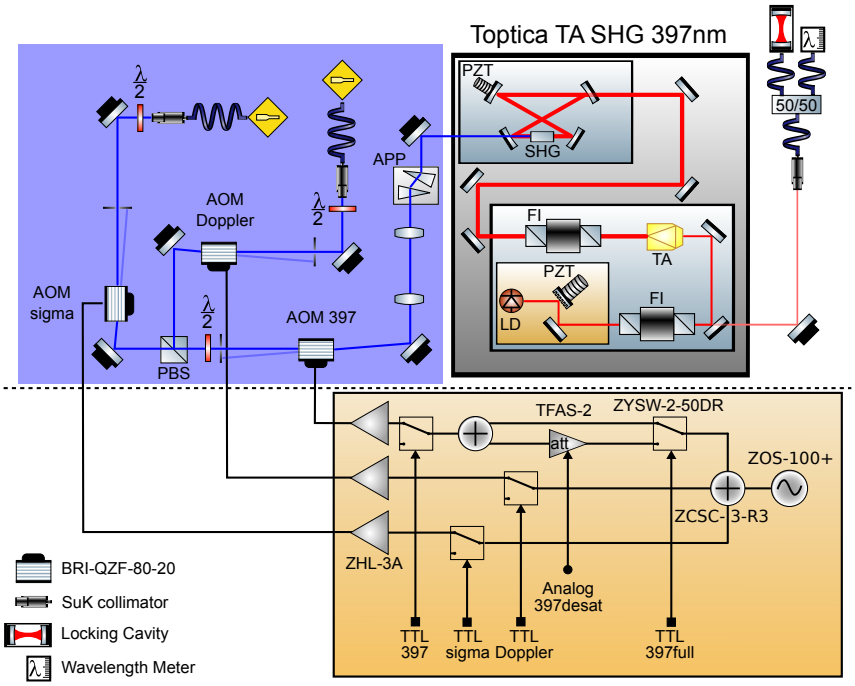

Figure 2.9.: 397 nm laser setup: All relevant parts of the optical setup creating the Doppler cooling and detection light as well as the light for optical pumping. The orange area highlights the AOM drive electronics mounted below the optical table. Further details see text.

optimum diffraction efficiency of the AOM. This signal is split and switched using high frequency switches. The first 397 nm laser AOM provides the possibility to be switched to reduced drive power. This results in lower laser power optimized for most efficient Doppler cooling. All signals have to be amplified before they are connected to their AOMs. The first single pass AOM is used to switch all blue light from this laser source. It is also used to change the intensity level on the following beam paths. The zeroth order is blocked using an adjustable iris. The laser light is now separated in two beam paths using a polarising beam splitter (PBS) and a $\lambda/2$ plate. One beam is used for Doppler cooling and one for optical pumping, referred to as sigma beam. Both beam paths lead through one additional AOM single pass and are coupled to individual fibres which lead to different viewports at the ion trap. Please note the additional $\lambda/2$ plate in front of the optical fibres to adjust the polarisation axis on the polarisation maintaining fibre, which is important for efficient optical pumping.

2.3.2. Repump Lasers

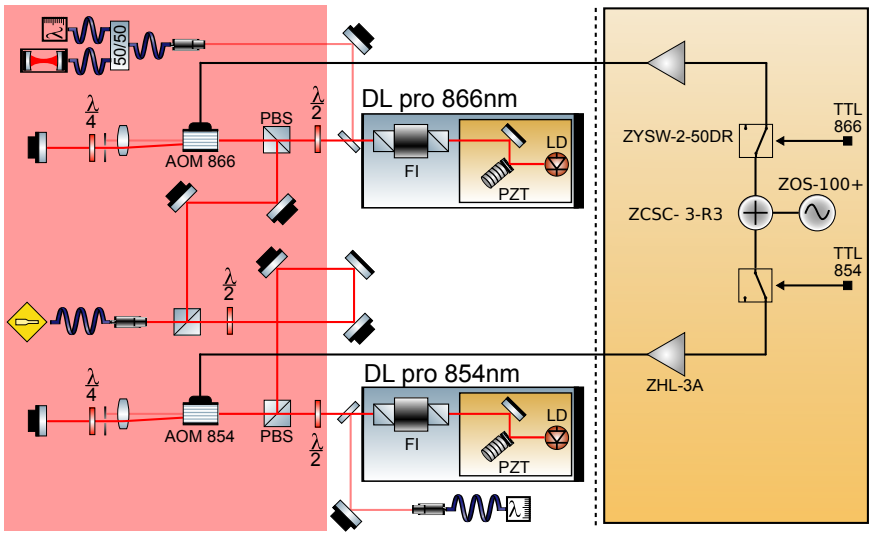

Figure 2.10.: 866 nm and 854 nm laser setup: The basic optical and electronic setup required for switching of the repump lasers. The orange area highlights the AOM drive electronics mounted below the optical table. Further details see text.

Both infrared laser sources used in this experiment are DL pro[22] type commercial diode lasers with enhanced frequency stability and a large modejump free range. Both lasers are equipped with Faraday insulators and produce almost gauss shaped beams which does not require further beam shaping. In figure 2.10 all relevant parts of the optical setup and necessary components for laser switching are shown. The AOM drive in this case only consists of a voltage controlled oscillator (VCO), a splitter, two RF switches and two amplifiers. From the light emitted by the laser systems a small part is branched off towards the wavelength meter. The laser at 866 nm is additionally guided to a frequency stabilisation cavity. The main part of each laser beam is lead directly to a double pass AOM for switching. Both double passes are set up in a cat eye geometry. The lens and the mirror in the switching branch build a cat eye geometric configuration. After switching both laser beams are overlapped and coupled into the same optical fibre. To allow uncoupled adjustment of the individual laser beams every beam is set up with four degrees of freedom adjustable.

[22]TOPTICA Photonics AG, Munich, Germany

2.3.3. Ultra Stable Laser System for Quantum Bit Operations

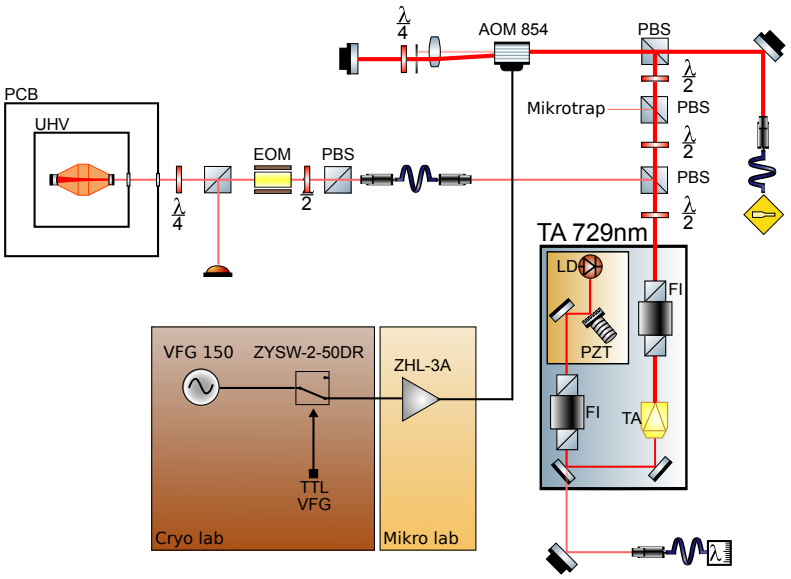

Figure 2.11.: Spectroscopy laser setup: A small part of the light emitted by the laser is sent through a fibre for mode cleaning. After polarisation filtering an EOM modulates sidebands to the light used for generating a PDH error signal. The main part of the light is split to different experiments. Only the relevant double pass is shown in this figure.

One additional double pass is set up in addition to the existing setup from [Pos10] to supply an optical fibre to the cryogenic experiment. The laser is stabilised on a high finesse cavity. A detailed explanation of the spectroscopy laser stabilisation can be found in [Pos10]. Figure 2.11 shows the relevant part of the frequency shifting AOM setup. The double pass is supplied from a versatile frequency generator[23]. This enables to generate spectroscopy pulses with defined frequency, duration, phase and amplitude. Laser pulse sequences with phase coherence can be realised with this drive synthesiser.

2.3.4. Frequency Stabilisation Setup of Dipole Lasers

Frequency stabilisation is done using the Pound-Drever-Hall method [DHK+83]. This method is commonly used and will be briefly discussed here. A frequency modulated laser source is sent to an optical resonator where a photo diode detects the reflection

[23] VFG 150, TOPTICA Photonics AG, Munich, Germany

signal. When the line width of the cavity is smaller than the modulation frequency, both side bands are reflected when the laser is in resonance with the cavity. By mixing this signal with the initial modulation one creates an error signal which is proportional to the frequency detuning. In the resonant case the two reflected side bands add up to zero due to a 180 ° phase shift from the mixing.

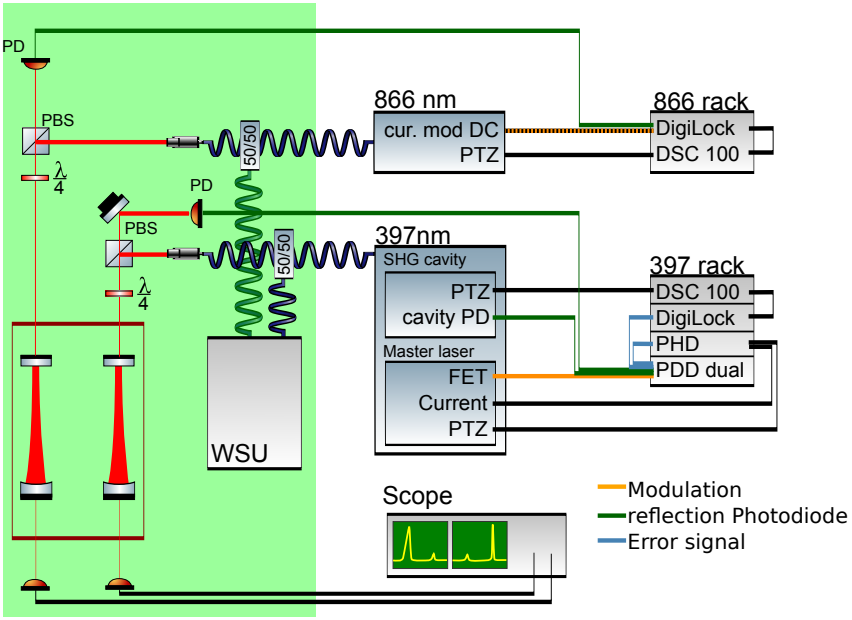

Figure 2.12.: Frequency measurement and stabilisation setup: The optical cavity resonator on the left side builds a solid state length reference for the laser sources. The control electronics on the right side adjust the laser wavelength according to this reference.

In figure 2.12 it is illustrated how the components required for this stabilisation scheme are set up. To get the reflected part of the cavity the incoupling beam is guided through a PBS. The following $\lambda/4$ phase plate rotates the polarisation of the reflected beam by 90 ° due to twice passing. The reflected light can now be monitored on a photo diode and generate the error signal. The easiest way to do so is shown with the laser at 866 nm. The commercial locking device DigiLock[24] is used to modulate the laser diode current and generates an error signal from the fed in photo diode signal. Two regulation outputs are used to correct the laser wavelength. Fast corrections are directly fed to the laser diode current and correct fast fluctuations. The slower corrections are applied to the piezo of the diode laser which stabilizes long term drifts. The Laser at 397 nm is more complex because it has to be stabilized to the SHG-cavity for frequency doubling and the external cavity for frequency stabilisation. Two error signals are created and

[24]TOPTICA Photonics AG, Munich, Germany

three regulation actuators are used to realize stable operation. A PDD dual is used to modulate the master laser and generate two error signals from the reflection diodes of the SHG- and the external cavity. For SHG stabilisation the PDH module of the laser system is used which regulates the master current and the master piezo. The external cavity error signal is lead to a DigiLock which regulates the piezo of the SHG cavity to correct slow frequency drifts. The laser at 854 nm is not locked to an external reference as this is not required for our experiments. For other laser sources like the photo ionisation lasers a cavity stabilisation is not required. This is because the transitions are much broader than the laser line width respectrive the atomic transition.

2.3.5. Laser Guidance and Imaging Design

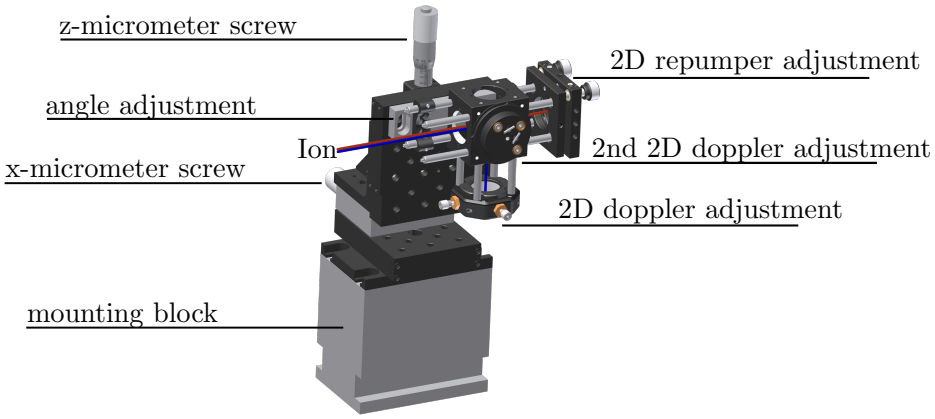

Figure 2.13.: Laser ion interface: The overlapping of two optical fibre outputs is realised by a combination of commercial manipulators (black) and three in-house build adapters (grey). A optimal overlapping of both beams is possible, using the three manipulators with two degrees of freedom each. A dichroic mirror inside the cage system cube[25] is used to realise a minimum loss overlapping. The whole fibre mounted cage system is mounted at an angle adjustment holder. In combination with the 3D micrometer stage (y-micrometer screw not visible) and the positioning of the mounting block a full angle alignment is possible.

The cryogenic ion trap setup requires, due to its thermal expansion and contraction, a reproducible positioning with sufficient travel. As all lasers are guided via optical fibres to the ion trap a micrometer stage based fibre out-coupler is the best realisation. The individual beams exit their respective fibres through a fibre collimator[26]. The complex fibre overlapping stage-design is shown in figure 2.13. Within the cage system

[26] 60FC series, Schäfter + Kirchhoff GmbH, Hamburg, Germany

several manipulators are used to overlap the two beams in five dimensions. Position and angle can be adjusted by the beam line manipulators. The individual collimator lenses are used to overlap the foci of both beams. The additionally used focusing lens (not shown in figure) enables influence on the beam waists as well. The whole cage system is mounted on an angle adjustable holder which establishes stable contact to the manipulator stage. The angle adjustment and the position of the mounting block on the table are fixed by locking screws. Three linear micrometer manipulators are used for aligning the beam on the ion. The micrometer scale on the actuators can be used to track the ion position or to recover laser positions. The whole stage can also be moved to measure beam waists and positions without destroying the relative alignment of both beams. Due to the combined movement of both beams the complexity of the system has been reduced. Similar setups with only one beam are built with the same manipulator stage but without cage system cube.

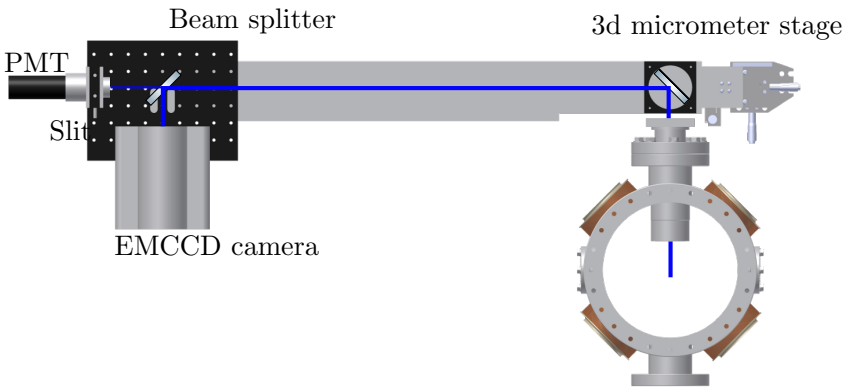

Figure 2.14.: Detection setup: The blue light emitted from the ion traverses through the objective inside the inverted viewport. After a 2" high reflective mirror the beam passes a 30:70 beam splitter and enters the two detectors.

The ion imaging is mainly done by a custom designed objective[27]. The imaging plane is adjusted to be at the electron multiplying charge-coupled device (EMCCD)[28] chip of the camera and in the slit of the photo multiplying tube (PMT)[29]. This light is once deflected from a mirror to propagate in the direction of the detectors. A beam splitter transmits 70 % to the PMT and reflects 30 % to the EMCCD camera. The beam splitter is mounted on a flip mount for fast removal. The EMCCD camera and the PMT are equipped with a spectral filter[30] which transimits light at 397 nm with 93 % with suppression of all other laser sources below 10^{-5}. The whole imaging setup

[27] Sill Optics GmbH & Co. KG, Wendelstein, Germany
[28] A-DU860-DCS-UVB, Andor Technology, Belfast, Northern Ireland
[29] P25PC 9111, Sens-Tech Limited, Midxx, UK
[30] SEM-FF01-395/11-25, Semrock, New York, USA

can be moved using a xyz-translation stage. This also ensures reproducible positioning and deterministic movement of the imaging optics.

2.4. Fast Voltage Control Hardware as Ion Interface

The operation principle of segmented ion traps as quantum processors is based on multiple transport operations [KMW02]. The qubits are shuttled, merged to larger crystals or split in separate potential wells. These operations are performed by varying the voltages of the axial DC segments. This leads to time dependent potentials which produces the desired ion movement in axial direction. The techniques to calculate these voltage ramps is described in chapter 3.

For fast transports described in section 6.3 the voltage ramps must be performed on the time scale of the axial harmonic oscillator. The next section describes the in-house developed hardware which key component is a low noise high speed digital to analog converter (DAC) which was chosen accord all requirements mentioned previously. This parallel arbitrary function generator is supplied using a continuous operational battery power supply described in section 2.4.2. The possibilities of this system are expanded by digital output channels, described in section 2.4.3, and the use of a power line and RF trigger, described in section 2.4.4. To allow more general applications the function generator got additional interfaces, described in section 2.4.5 and section 2.4.6. The automatic test equipment (ATE) described in section 2.4.7 is used to perform specification and calibration data of the function generator.

2.4.1. Multiple Arbitrary Function Generator

The Hardware design is shown in figure 2.15 and uses an field programmable gate array (FPGA) as versatile real time source for digital pulses. The experimental control personal computer (PC) transmits data in form of digital pulse sequences to the FPGA. They are stored and can be executed multiple times via a looping command. The raw Ethernet protocol enables reliable and fast data transfer with high transfer rate. A separate transistor-transistor logic (TTL) trigger starts preprogrammed pulse sequence. Due to more then 100 digital output channels the FPGA also provides digital TTL signals for general purpose which is explained in section 2.4.3. The firmware of the FPGA[31] was designed and realised by K. Singer and S. Dwakins. The embedded PowerPC is used to handle the ethernet communication and store the data in the double data rate random access memory (DDR-RAM) of the board. If the execution is started via the trigger, the FPGA uses direct memory access (DMA) to load the data into a cascaded first in first out (FIFO) which is stored in the block random access memory (RAM). After this initialisation the FPGA runs a state machine which writes

[31] Avnet Virtex-5 FXT Evaluation Kit, Avnet electronics marketing, Phoenix, USA

the digital signals to the output pins. The digital low voltage transistor-transistor

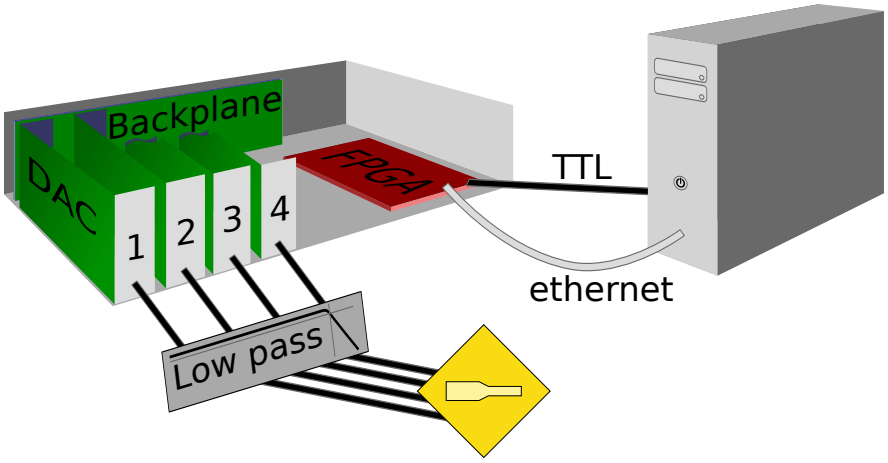

Figure 2.15.: Multiple arbitrary function generator setup: The information of shape and timing of all voltage functions is generated on a PC and sent to the FPGA. The stored sequences are started by a TTL trigger and propagate over the *backplane* to the DAC boards. There the voltage ramps are generated and they are fed to the ion trap through low-pass filters.

logic (LVTTL) signals from the FPGA are fed to the backplane for distribution to further circuits. Input buffers increase the signal strength to the standard TTL level. High speed digital insulators[32] are used to separate the noisy FPGA lines from the voltage generation part. The backplanes digital lines are resistor terminated to the individual DAC boards to reduce ringing on the digital data lines. Furthermore the clock signal is delayed by an adjustable duration, which allows the programming data to be at the same speed as the clock. For the highest programming frequency of 50MHz the clock is delayed half a cycle to match the specification. This ensures that the serial data is present when the reading clock flank rises. After the insulation components a separate, noise reduced power supply is used. It can be a commercial high stability voltage supply or our low noise battery power supply described in section 2.4.2.

The required voltage change is on the timescale of the motional frequency $\tau = 2\pi/\omega_z \approx 1\,\mu$s. To create axial frequencies about 1 MHz DC voltages from -10 V to +10 V are required. The high voltage resolution of 16 bit enables optimisation of transport operation using the high voltage resolution from one least significant bit (LSB) steps of 305 μV. To operate the whole ion trap with 32 segments, while each segment consists of two electrodes, there are 64 analog output voltages necessary. One DAC circuit board performs the generation of up to 24 high speed analog voltages and was developed in collaboration with H. Lenk. Figure 2.16 shows a pseudo circuit of one channel process-

[32]HCPL-900J high speed magnetic coupling insulator, Avago Technologies, San Jose, USA

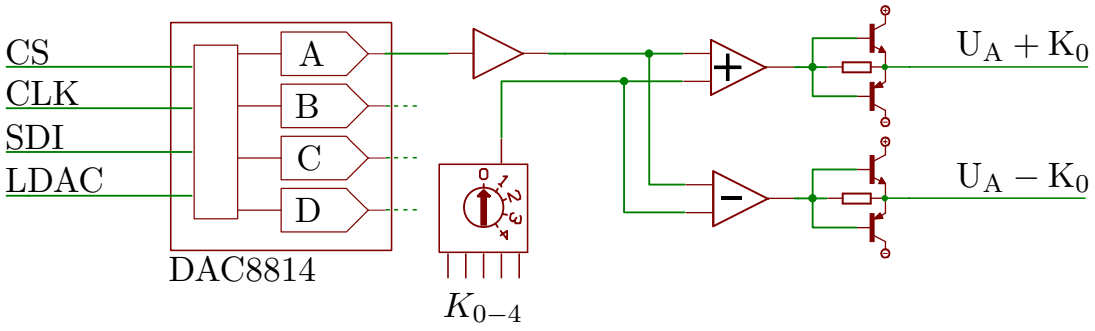

Figure 2.16.: Digital to analog converter circuit: This sketch shows the principle of the signal generation. All output channels are generated by a similar circuit, so only one is shown to explain the principle. The first operational amplifier after the DAC is used to create the output voltage U_A. The correction voltage K_i is chosen via a rotary DIP switch and is then added and subtracted to generate two voltages supplying the electrode pair of one segment.

ing the circuit board. The digital signals from the back plane are first conditioned and then lead to the 16-bit quad-DACs[33]. These are fed with an 18 bits serial command to program one output voltage. The two extra bits are for choosing the desired output channel. This serial protocol is sent through the serial data input (SDI) channel timed by the clock input (CLK) channel. The load DAC (LDAC) input is used to simultaneously apply all programmed voltages to the four outputs of one DAC chip. The chip select (CS) line is used to address individual chips, they are only programmable if the corresponding CS line is set. The fast DAC chips produce defined output currents using a resistor ladder type circuit with internal feedback. This is why the first operational amplifier (op-amp) is used to generate a defined output voltage which can be used for further processing. This segment voltage U_A will now supply two physical trap electrodes belonging to one segment A. One on the top layer and on the bottom layer of the 3D trap. The *compensation voltage* is the difference between the two electrodes of the same DC-segment number. To vary the compensation voltage of a group of segments, its source can be chosen via a rotary DIP switch for each segment. For one electrode of a given semgent, the compensation voltage K_i is added to the segment voltage V, while it is subtracted from the other one. Thus the actual compensation voltage is twice the voltage K_i.

[33]DAC8814, Texas Instruments, Dallas, USA

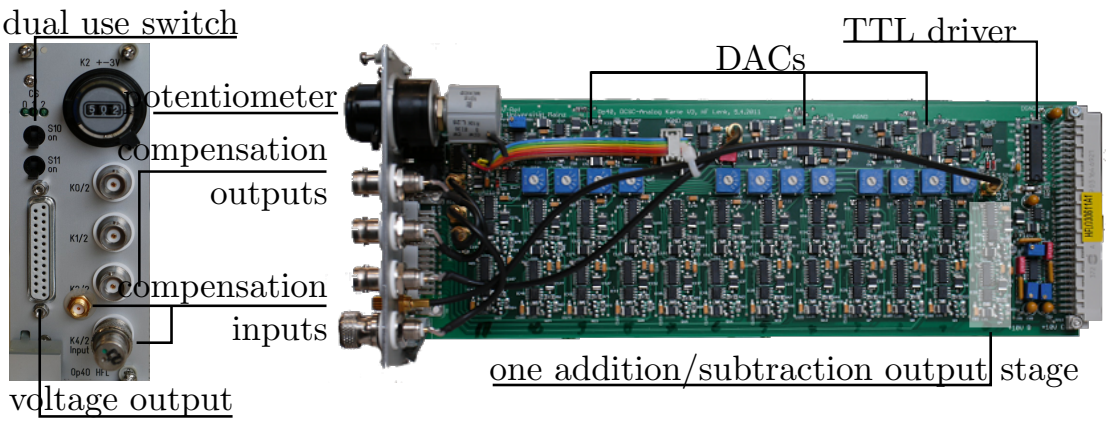

Figure 2.17.: Digital to analog converter board: The front and side view of the DAC board. Additionally to the highlighted components are the blue rotary DIP switches for each channel and the large grey connector for the backplane are visible.

The different compensation voltages are either created by DAC channels or fed in from the front connectors as shown in figure 2.17. Two voltages created from a DAC can be used as digitally controlled compensation voltage. If these channels are used as compensation voltage there corresponding outputs at the D-Sub connector can be switched off using switches on the front of the board. The ten-turn wirewound potentiometer for direct adjustment by hand in the range from -3 V to +3 V. Two additional compensation sources can be fed in through the front connectors. This is usable for long distance transports where a DAC compensation voltage from one board should be used on further boards. This is also the reason why the three mainly used compensation sources are available through front connectors. The final output voltages are created by a transistor output stage with unity gain. This is required to reduce the output impedance and enables the voltages ramps to drive the capacitance of the trap electrodes and the capacitances of additional filters.

The multiple arbitrary function generator is able to supply 96 analog output voltages in the range from -10 V to +10 V with a voltage resolution of 0.3 mV. The maximum update rate is dependent on the amount of used channels as shown in table 2.1. It depends on how many serial commands have to be send to the individual DACs.

Number of channels	Number of output voltages	Max update rate MS/s
1 - 9	2 - 18	2.500
10 - 24	20 - 48	1.250
25 - 36	50 - 72	0.625
37 - 48	74 - 96	0.312

Table 2.1.: Analog update rates

2.4.2. High Stability Battery Power Supply

The power supply consists of two pairs of lead-acid accumulators[34] which are operated and recharged alternating. The conductor switching is realised by four bistable double pole double throw (DPDT) Relais to maximize operation time. One pair of batteries is connected directly to the voltage output on the back side, while the non used pair is connected to separate charging circuits. Each charging circuit is a constant voltage and constant current source with 2 A and 14.5 V charging voltage or 13.5 V conservation voltage.

Figure 2.18.: Low noise battery power supply: In the left part the display and control unit and in the right part four separate charging circuits, each connected to one battery

A non interfering voltage measure circuit tracks the supply voltages of both accumulators in use via two insulation amplifiers. The voltage measurement and control of used and charged batteries is managed by a micro controller[35]. If one accumulator voltage drops below the minimum voltage an acoustic alarm informs the operators. If required a automated battery pair switching is possible as well. As shown in figure 2.18 is all necessary information about the batty voltage supply is visible on a digital display in the front of the case. Even if the circuit design ensures no influence of the voltage measurement on the supply voltage a future addition might be one additional TTL input,

[34] 12 V 12 Ah
[35] ATMega16, Atmel corporation, San Jose, USA

which disables all operations of the micro controller whene measurements require strict decoupling of the main power line.

2.4.3. Multiple Digital Output Expansion

A useful expansion to control additional digital channels. The circuit board is designed to be attached directly to the FPGA. The circuit is a TTL driver stage for the LVTTL outputs of the FPGA. All 30 output signals are available via bayonet navy connector (BNC) connectors on the front side. Two digital inputs are placed on the same circuit. The inputs are double buffered to protect the FPGA from damage. Further details see in [Len]. Correct settings in the firmware of the FPGA allow the usage of these inputs as triggers or other input values.

2.4.4. Power Line and Radio Frequency Trigger Expansion

Experiments like Ramsey measurements (section 5.3) require precise control over the global timing of measurements related to external signals. For example the omnipresent 50 Hz signal from the power line influences several components of the experiment. The other relevant signal is the RF drive frequency at about 30 MHz which directly influences the ion motion in the trap.

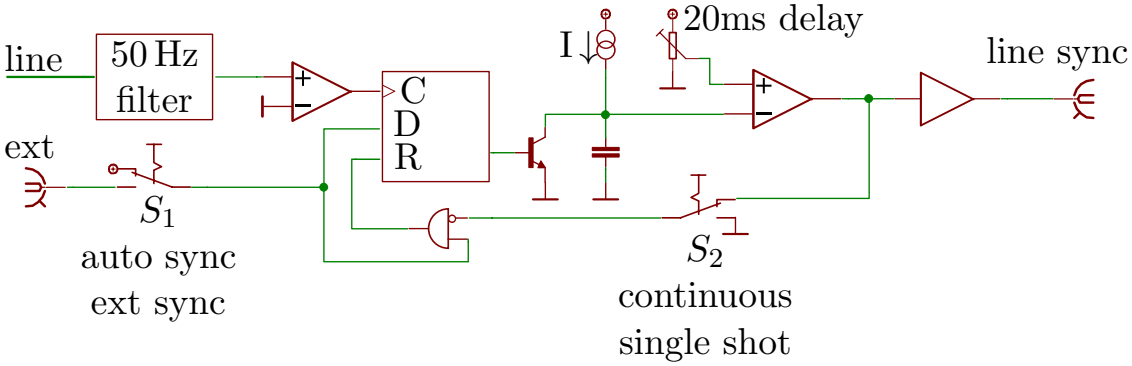

Figure 2.19.: Power line trigger: Reduced electronic circuit to explain the function principle of the power line trigger.

Two consecutive triggers for both frequency ranges are used to realize a measurement synchronisation. The function principle of the line trigger is shown in figure 2.19 and a detailed explanation can be found in [Len]. The Line voltage is cleaned through a 50 Hz filter to remove higher harmonics and other noise. The first comparator is used to create a high flank on the zero crossing of the sinusoidal line voltage. This flank triggers the clock of a D-type flip-flop, which operates on eternal triggering set by the synchronisation switch S_1. This switch controls the data input (D) from high to

external input. Within this state the trigger waits for a external high level. The flip-flop output starts charging a capacitor supplied from a constant current source. The capacitor voltage is compared to a voltage which enables to choose a time delay up to one line period (20 ms). These voltages create a high flank in the following comparator dependent on the delay setting. Using this technique, one is able to control the phase of the power line trigger. The second switch deals with the flip-flop reset circuit. It can be operated in single shot mode or it is continuously resetting the flip-flop.

The much faster RF-trigger works basicly with the same mode of operation. An adjustable nanosecond delay is created by phase shifting of the input signal. This is done by changing the impedance within a multi pole low pass filter. A high speed comparator creates a trigger signal which is then buffered by a flip-flop, which creates the output signal. All details can be found in [Len].

2.4.5. USB Interface Expansion

To increase the flexibility of the voltage supply system, we developed a different source for the digital pulse sequences. The universal serial bus (USB) interface was chosen because it is widely used in almost all computers. The easiest way to create digital pulse sequences is using a USB-FIFO[36]. Via a software interface pulse sequences are defined and sent to the FIFO. One big drawback is that the execution depends on software run time and internal driver timings. The digital sequence can not be timed properly without a real time operating system. But for less critical timing operations this interface provides fast and easy control over many analog output voltages.

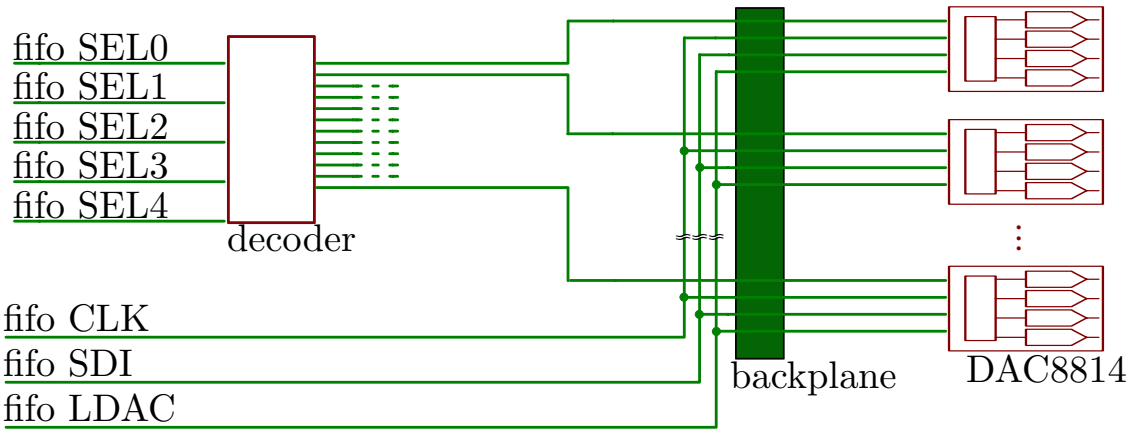

Figure 2.20.: USB-FIFO interface wiring: Reduced electronic circuit of the USB-FIFO interface. On the right are the contacts of the USB-FIFO module which are multiplexed and then passed too the backplane.

[36] FT2232H Mini Module, Future Technology Devices International Limited (FTDI), Glasgow, United Kingdom

The 16 digital out lines of the USB-FIFO require a multiplexing of the CS lines while using a common SDI line to supply all DACs. The built-in decoder allows to address only one DAC for programming. Using this technique only two fast digital out lines for CLK and SDI are reqired. The timing for the multiplexed CS lines is about a factor of 20 slower. Thereby the analog voltage update rate depends linearly of the amount of used channels. The synchronisation of the channels is guaranteed by a single LDAC flank after all DACs have been programmed.

2.4.6. Printer Port Interface Expansion

One further DAC programming interface is realised mainly for failure detection, debugging and maintenance. The line print terminal (LPT) board is connected to all four DAC board slots in parallel. Additional light emitting diodes (LEDs) are added as simple debugging tools to track line activity. Default use is to test full functionality of a backplane. The required power supply for the high speed insulators on the backplane is not provided from the LPT interface and must be connected separately from the rack power supply.

2.4.7. Automated ADC Calibration Expansion

To ensure full operation of all output channels an additional multiple channel digital volt meter was designed as ATE. The separate module allows high precision voltage measurement of all 24 output voltages from one DAC board. This allows a serial functionality test as well as the automated creation of calibration data for each channel. The calibration data can be used to correct the software DAC programming for reaching more precise output voltages.

The circuit consist of a 24×1 relay matrix which enables the selection of one output signal from 24 input signals. This signal is fed to the second part, which key component is a 24 bit analog to digital converter (ADC)[37]. One conversion with full resolution takes about one second including readout. This low power ADC reaches enough voltage resolution to measure LSB changes on the 16 bit DACs. The measurement range can be changed with a switchable high precision resistor array. This resistance changes the voltage applied to the input amplifier, which supplies the ADC.

The relay matrix is controlled by a decoder logic circuit which ensures defined switch states for all input states. The source for digital signals is a USB-FIFO[38], as described in section 2.4.5. It is used as source for static digital signals as well as for the communication with the ADC. Therefore it uses its serial peripheral interface (SPI) which

[37] MAX11210, Maxim Integrated, San Jose, USA
[38] FT2232H Mini Module, Future Technology Devices International Limited (FTDI), Glasgow, United Kingdom

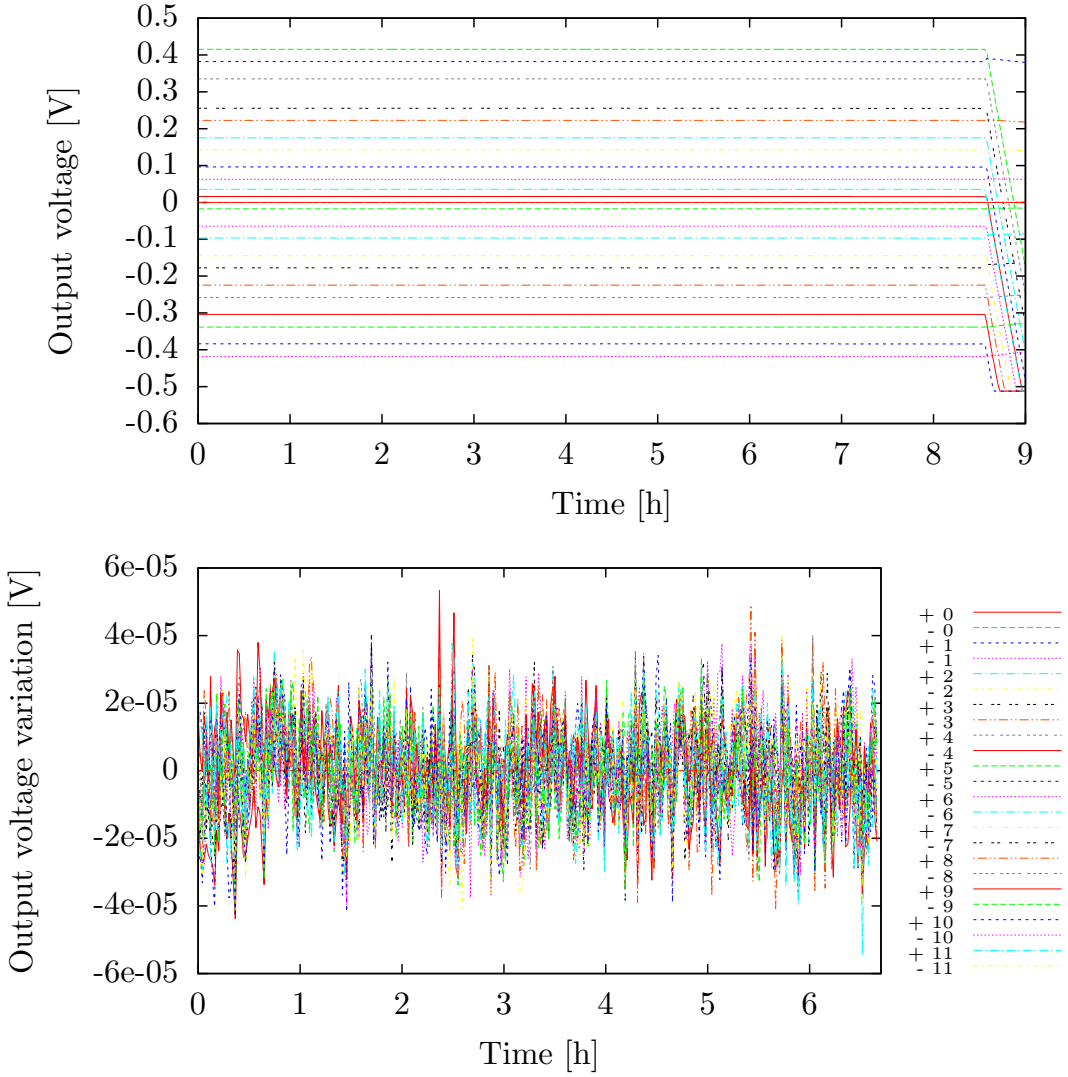

Figure 2.21.: Long term ADC measurement: All output channels have been measured over ten hours. The top part shows the individual programmed voltage until the battery supply voltage drops. In the bottom plot, the first 6 hours, are analysed by calculating the variation of the individual output channels. The common variation produced due to the drift from the ADC, was removed by subtracting all channesl from channel +0. The standard deviation from all measurement points is 12 μV wich corrisponds to 0.041 LSBs from the DAC.

can be software activated. The control commands are sent via this 2-wire interface to

the ADC and set parameters like conversion time and gain settings. The measurement result is read by the same interface and available in the experiment control software.

This hardware is capable of measuring all channels automatically which is shown in figure 2.21. A long term measurement was performed to determine the output voltage stability during battery power supply operation. The measurement started with a fully charged set of batteries and continues for 10 hours. Each voltage output was programmed with a different output voltage and measured afterwards using the ADC. The maximum accuracy is achieved by using a conversation time of 1 s per channels which leads to a measurement interval of approximately 1 minute. After 7 hours a minor voltage drop started, after 8.5 hours one battery was empty and some channels dropped to the negative supply voltage. The lower part of figure 2.21 shows the long term stability of all channels subtracted from the respective mean value. Over more than 6 hours the standard deviation from all pints 12.6 μV, which corrisponds to 0.041 LSB of the DAC. The common behaviour of all curves also implies that the main features are caused by a drift of the ADC or external pickup. The high measurement precision of the ADC allows an automated calibration measurement shown in figure 2.22. This measurement was performed by programming one output channel of the voltage supply with a high resolution linear voltage ramp. Each voltage is programmed and measured afterwards. Because the voltage resolution of the ramp is tighter than the DAC resolution, the LSB increments can be observed in the signal. The better voltage resolution of the ADC allows a precise determination of the discrete voltage steps. The model function

$$f(u) = A + B \times g^{-1}(\lfloor g(u) \rfloor), \quad \text{with } g(u) = \frac{u+10}{20} \cdot 2^{16} \tag{2.1}$$

is based on a rescaling to the binary resolution using fuction $g(u)$ with the correct voltage range (-10 V to +10 V) while u is the desired voltage. The parameters A and B are used to describe the deviation from optimal behaviour. The voltage is scaled back after the floor value $\lfloor a \rfloor = a' \in \mathbb{Z}$ was taken to create discrete voltage steps. The standard deviation in the lower part of figure 2.22 is 0.17 LSBs of the DAC. The variation in this measurement occures mainly due to ADC drifts which can not be corrected for this evaluation.

2.5. Experiment Computer Control

The key component of the experiment control is build a PC where several instruments are connected to. The homebuild control software uses the instruments application programming interfaces (APIs) and several extensions to access the hardware components. The software is written in C/C++ with an graphical user interface (GUI) written in QT mainly by K. Singer. All measurement routines consist of a hardware initialisation part followed by a measurement loop which writes out digital pulse sequences and reads

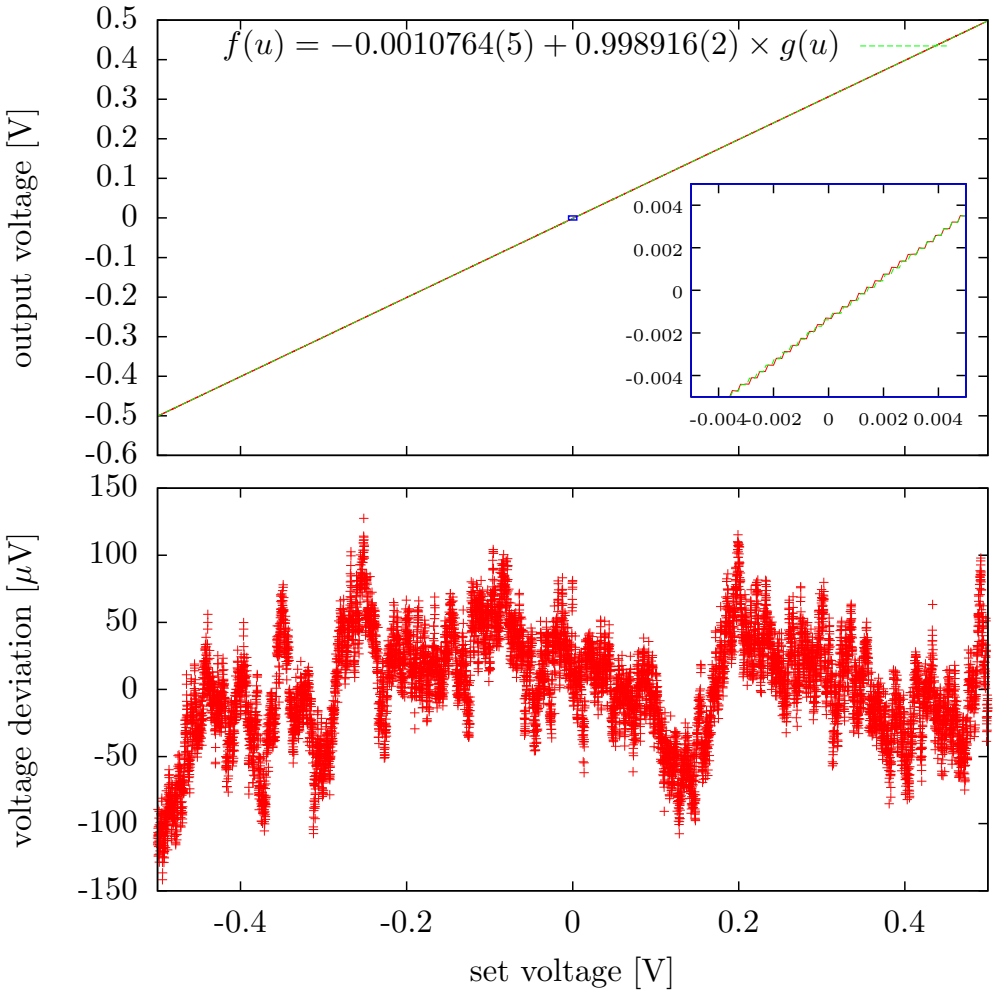

Figure 2.22.: Linearity of the DAC output: High precision measurement of one channel with high resolution programmed voltages. The magnified inset shows the DAC discretionary which is simulated with the discretisated function from equation 2.1, which allows the determination of linearity and offset parameters. The lower plot shows the variation from the model function.

fluorescence data from the PMT or the EMCCD-camera. Further details can be found in the measurement sections.

In figure 2.23 the main hardware components and their connections are shown. The control computer has peripheral component interconnect bus (PCI) high speed output cards[39] installed. These cards are synchronised and supply digital pulses with a

[39]PCI-6733 and PCI-6713, National Instruments, Austin, USA

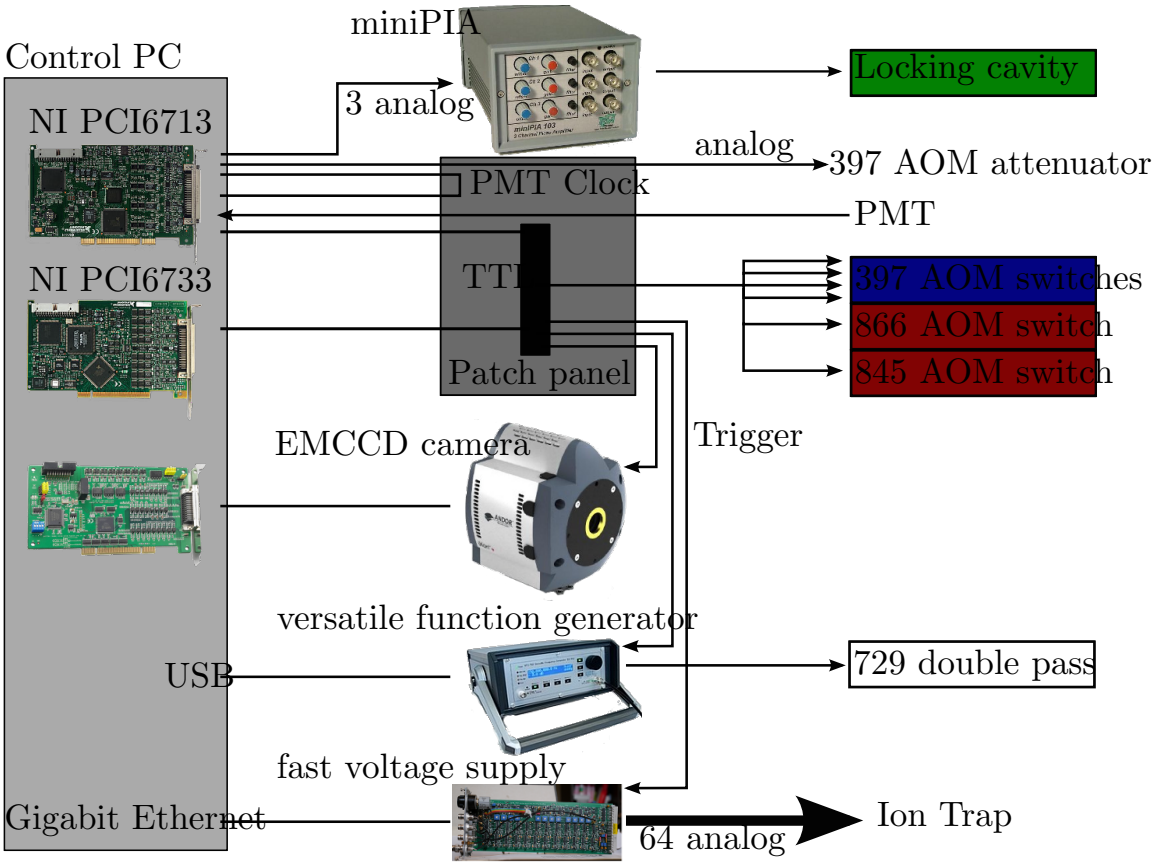

Figure 2.23.: Experiment control setup sketch: All key components are connected to the experiment control computer. The two national instruments cards handle analog and digital output as well as fast digital counting of the PMT signals. The analog signals control the locking cavity piezos and 397 nm AOM power during Doppler cooling. The digital TTL signals trigger all further instruments and supply the digital pulse sequence to the laser switching AOM setups. Data for the VFG is supplied via USB and to the fast ion trap voltage supply via Gigabit-Ethernet.

maximum time resolution of 1 MSp/s on all 8 digital channels. They also support high-speed analog channels, but in this experiment they are only used as static analog voltage source. Three analog voltages supply a three channel high voltage amplifier[40], which drives the locking cavity piezos described in section 2.3.4. This allows changing of the optical resonator length and resonance wavelength. This technique is used to tune the locked laser wavelength to the ion resonance. One additional analog voltage supplies a variable attenuator in the 397 nm laser AOM setup described in section 2.3.1. The

[40] miniPIA, TEM Messtechnik GmbH, Hannover, Germany

Digital TTL lines are connected to the RF-switches in all AOM laser switching setups. They are used to create fast laser pulse sequences. Additionally any further instrument, used in the experiment, is triggered by these digital pules. This technique ensures a synchronous operation of all experiment components. One special digital output channel is used to synchronise the PMT-detection with the laser pulse sequence. This *PMT clock* or *counter clock* is looped back to an input pin of the fast counter of the high speed output card and defined as clock in the software. The EMCCD-camera used for detection uses a special data transfer PCI-card to communicate with the computer. The settings like exposure time and gain are programmed and taken images are read out through the software interface of this control card. For synchronisation a separate digital TTL line is used. The *versatile function generator*[41], is used to drive the AOM of the spectroscopy laser as described in section 2.3.3. The required data characterizing the RF-pulses are transmitted via USB to the function generator. Again the digital trigger is used to ensure synchronous operation. The *fast voltage supply* of the ion trap is described in detail in section 2.4. The control computer transmits the voltages sequences via Gigabit-Ethernet and execution is timed by a digital trigger.

[41] VFG150, TOPTICA Photonics AG, Munich, Germany

3

Simulation of Static Electic Fields and Ion Dynamics in Time Dependent Potentials

The confinement and dynamics of an ion within a complex Paul trap geometry can not be solved analytically and rely on numerical simulations. The cornerstone of reliable simulations of electrostatic properties and particle dynamics is a geometric model of the trap with a sufficient detail level. The required detail level strongly depends on the chosen geometry. These geometric information is used to first determine surface charge distributions and afterwards electric potentials as described in section 3.2. This electrode related information can be used as a basis to analyse static or dynamic trapping potentials, as described in section 3.6.1 and propagate one or several ions in these potentials in section 3.5. The simulated potentials can also be used in a fast, simplified scheme for transport based quantum computing as described in section 3.7. A precise simulation supplies numerical data to verify experimental data and allows to determine experiment parameters to manipulate the ion in a defined way. It is also an essentcial tool for developing and optimizing ion trap geometries.

3.1. Segmented Micro Paul traps

The initial particle trapping principle was invented by Wolfgang Paul [PS53, POF58] and valued with the Nobel prize 1989. The combination of DC potentials and dynamic RF potentials create a three dimensional (3D) time varying potential which gives rise

to a trapping confinement for charged particles in free space. The ion's trajectory is described by uncoupled *Mathieu differential equations* for all coordinates u:

$$\ddot{u} = -a_u u + 2q_u \cos(2\tau)u \ , u = x, y, z, \tag{3.1}$$

using the following definitions

$$\begin{aligned} \tau &= \frac{\Omega_{rf} t}{2} \\ a_u &= \xi_u \frac{8eV_{dc}}{m\Omega_{rf}^2} \\ q_u &= \zeta_u \frac{4eV_{rf}}{m\Omega_{rf}^2}, \end{aligned} \tag{3.2}$$

where e is the charge of the particle with the mass m, the RF drive frequency Ω_{rf} and amplitude V_{rf} as well as the DC voltage V_{dc}. The only geometric parameters are the curvature ξ of the DC potential and the curvature ζ of the RF potential.

These equations of motion can be analysed in several ways. The geometry of the used ion trap determines the force components for the different spatial directions. For the linear segmented paul trap it turns out that $q_z = 0$, $q_x = -q_y$ and $a_z = a_y = -a_x/2$. This allows us to take a closer look at the axial confinement which is independent from the RF field. The equation of motion corrisponds to a simple harmonic oscillator

$$m\frac{d^2z}{d\tau^2} = \frac{4}{m\Omega_{rf}^2}\frac{d^2z}{dt^2} = -a_z z \tag{3.3}$$

with the effective spring constant a_z. The axial trapping frequency can now be obtained by taking the DC curvature ξ_z into account:

$$\omega_z = \sqrt{2\xi_z eV_{dc}/m} \tag{3.4}$$

The radial components of the Mathieu equations undergo a fast oscillation called *micro motion* with the frequency of the drive field and a slower motional frequency from the confinement created by the drive field, called *secular motion*. These oscillations are described by [Gho95]:

$$u_{x,y}(t) = A\cos\left(\beta_{x,y}\frac{\Omega_{rf}}{2}t\right)\left(1 - \frac{q_{x,y}}{2}\cos(\Omega_{rf}t)\right) \tag{3.5}$$

Where the *secular motion* with the frequency $\beta_{x,y}\Omega_{rf}/2$ is modulated with the drive frequency. The stability of this motion is described by the value of β, which is a function of a and b. In a simplified picture the ion moves slowly in a rapidly oscillating field. The polarity change of the field is much faster than the ion's movement. The basic principle can be illustrated as follows: The ion starts accelerating to the attractive RF

electrode. While the ion gets closer to the electrode the field strength increases and the polarity of the drive field changes. These two facts result in a repelling force on the ion. In time average the repelling forces form a trapping confinement. The ion now minimizes its oscillation energy and is pushed towards the minimum of the electric field amplitude, which is given by the node of the drive field. The RF drive field forms an effective potential, termed the *ponderomotive* potential:

$$V_{pond} = \frac{e^2|\vec{E}|^2}{4m\Omega_{rf}^2} \tag{3.6}$$

The particle with charge e and mass m feels a potential proportional to the electric field vector length $|\vec{E}|$ and its drive frequency Ω_{rf}. Note that no time dependent potential data is required. The electric field vector is determined by a electrostatic simulation. It can be modelled by a 1 V electrode voltage and scaled up in further applications. This simplified picture can be used to determine motional frequencies and the ion's equilibrium positsion in the trapping potential. If stability information and details about the micro motion are required, one has to evaluate the full Mathieu equation in the time varying potential.

3.2. Numerical Electric Field Simulation

A variety of numerical methods are available to solve problems like determining the electric potential created from certain electrode geometries. A general overview can be found in [SPM+10] which describes the finite difference method (FDM), the finite element method (FEM) and the boundary element method (BEM). Within this thesis a short description of the used BEM will be presented. Mostly used algorithms are FEM and the BEM which are available as commercial products as well. FEM is generally easier to implement, but leads also to less accurate results, while BEM needs more computational power to solve similar problems. K. Singer implemented a version of BEM enhanced by the fast multipole method (FMM), which allows a fast and precise calculation of potentials.

For all algorithms the staring point is a geometry definition as shown in figure 3.1. This version is generated from a program code which assembles all necessary faces in the right way. The ion moves along the geometric centre of the trap, which is termed as axial trap position from now on. All electrode dimensions are defined as variables, which are used to generate all surfaces. The big advantage for optimizing trap structures is the fast design change by adjusting individual geometry parameters. The program also supports the use of geometry definitions in computer-aided design (CAD) files, requirering a 3D model realised with CAD software. This method is only preferred if a finished design file is already at hand and can be adapted to the simulation. BEM operates with the Coulomb law to determine the electric potential in free space. The

electrode structure is separated in small parts which all carry some surface charge. The potential is now obtained by summing up the individual parts of all surface elements. The first step is to determine the surface charge distribution from the electrode geometry and separate the electrodes in several surface elements. This basic idea of the FMM is to perform a grouping of surface elements which have similar influence. For example a group of far distant elements can be combined, and the electrostatic potential of this group can be represented by a multipol expansion. This speeds up the usual scaling from BEM with N^3 to N, where N is the number of sufrace elements. Using this precise potential calculation it is also possible to perform numeric derivatives to obtain additional information like the electric field and the curvature. The main issue with this kind of numerical simulation is that the result might be dependent on several algorithm parameters, like the refinement of the electrode segments. The simulation result has to be verified by convergence tests. The biggest source of inaccuracy for micro structured ion traps is the production process, which introduces deviations from the designed and the realised electrode geometry. Detailed information on the production process can be found in [Sch09] along with a measurement of the actual geometry. These deviations can also be included in the geometrical model to increase accuracy of the simulation results.

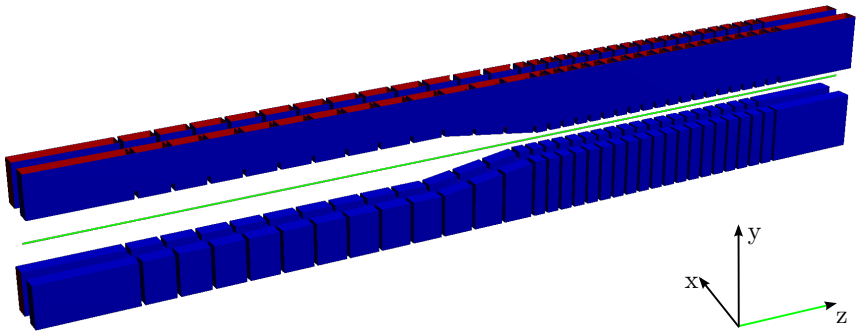

Figure 3.1.: Simulation trap model: Conductive surfaces realised with C/C++ simulation software described in [SPM+10]. The large solid electrode is the RF electrode and the opposite separated electrodes are DC electrodes.

There are two usual simulation modes: The static and the dynamic simulation. The static simulation is used to obtain a set of potential data which can be used in further algorithms to determine defined quantities. This method is used to optimize ion trap designs or calculate transport operations. This mode calculates potential data, which can be adapted for different ion trap operation conditions. Different questions require a complete dynamic simulation of the 3D trajectory of the ion inside the trap. In this mode realistic operation parameters like RF drive voltage and frequency are simulated with a defined DC configuration. The ion is then inserted with a certain kinetic energy and propagated through the time varying potential.

3.3. Axial DC Potentials

The possible outcome of numerical potential simulations can be stored and look like figure 3.2. Each potential curve was calculated using only one segment at -1 V and grounding all others. Using this technique one achieves a universal data set which allows to superimpose all possible DC voltage configurations and calculate the overall potential just by adding the potentials. One clearly observes the potential dependence

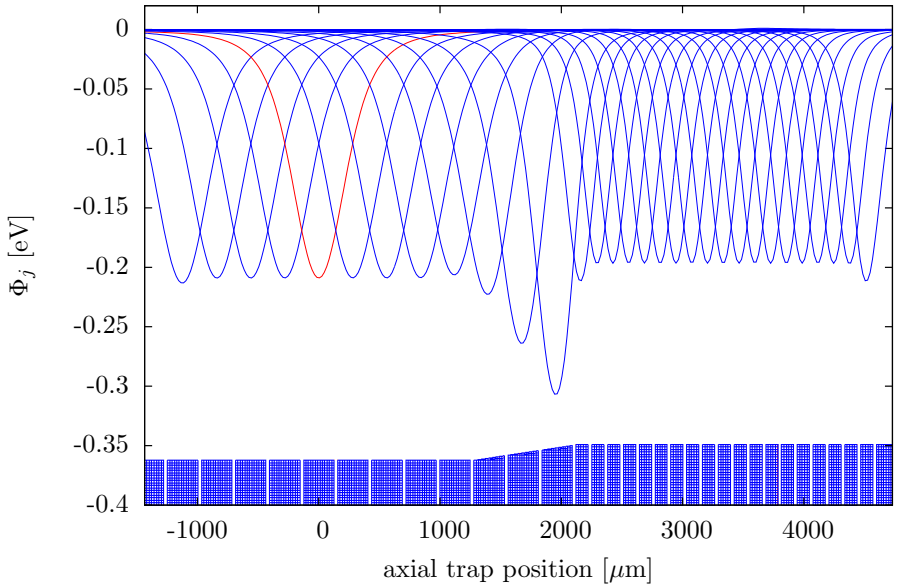

Figure 3.2.: All DC potentials: The individual curves correspond to the DC potential in the geometric centre of the trap, generated by one electrode pair at a voltage of -1 V. Highlighted is the main trapping potential from segment 5. Also visible is the corrisponding potential minimum value within the loading and the trapping region.

on the electrode's width and their distance to the geometrical centre of the trap. The constant width in the loading and taper region leads to increasing potential depth for the three taper electrodes because they get closer to the ion's movement axis. The smaller width of the processing region electrode compensate exactly the closer distance to achieve the same maximum potential depth. The same voltage range is used to generate similar trap depths in the loading and the processing region.

In figure 3.3 the electric potential created from one electrode with a voltage at -1 V is shown with its two neighbouring electrodes is shown. It also shows the numerical derivatives in axial direction up to the second order. The potential valley like in figure 3.3a) is shaped like a parabola in the centre, which fades out to zero in far distance. A trapped particle will be trapped inside if its kinetic energy along that axis is smaller

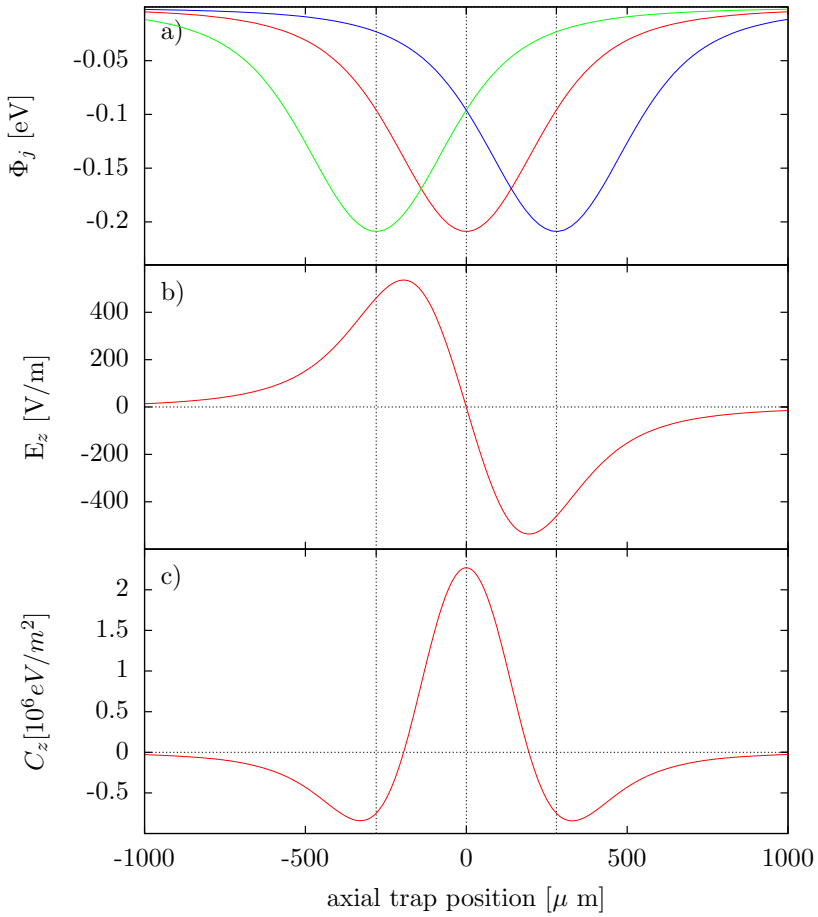

Figure 3.3.: Three potentials with field and curvature: The electric DC potential (a) generated by segment 5, the axial electric field (b) and the electric field curvature (c) is shown. The neighbouring segment 4 and segment 6 generate a similar potential translated by one inter-segment distance (280 μm). The dashed lines indicate the geometric position of the neighbouring segments to illustrate the effect of force and curvature on these: The force exerted by a neighboring electrode is close to the maximum value, and negative voltages on a neighbouring segment leads to a loss of confinement strenght.

than the valley depth. The next consideration treats the kind of trapping, which is be shown in figure 3.3b). The repelling force $F = eE$ is direct proportional to the electric field. The linear range around the centre shows where the force is proportional to the displacement. In figure 3.3c) the electric field curvature C_z is shown for segment 5. It illustrates the strength of the restoring force created by the field. The peak value defines the harmonic frequency ω_z according to equation 3.4. This formula illustrates

that a neighbouring negative electrode voltage will decrease the axial frequency, because the total curvature will decrease. On the other hand the curvature at segment 5 can be enhanced by applying a positive voltage to segments 4 and 6. The dimensions of the electrode influence the shape of the curvature and one clearly recognises that the minimum curvatures in figure 3.3c) are close to the neighbouring electrodes. For the applied negative voltage of -1 V one would achieve trapping of Calcium ions up to an energy of 200 meV. The realised harmonic frequency would be 500 kHz. The electrode distance is chosen to create high electric field and a high curvature at the neighbouring electrode.

3.4. Radial RF Potentials

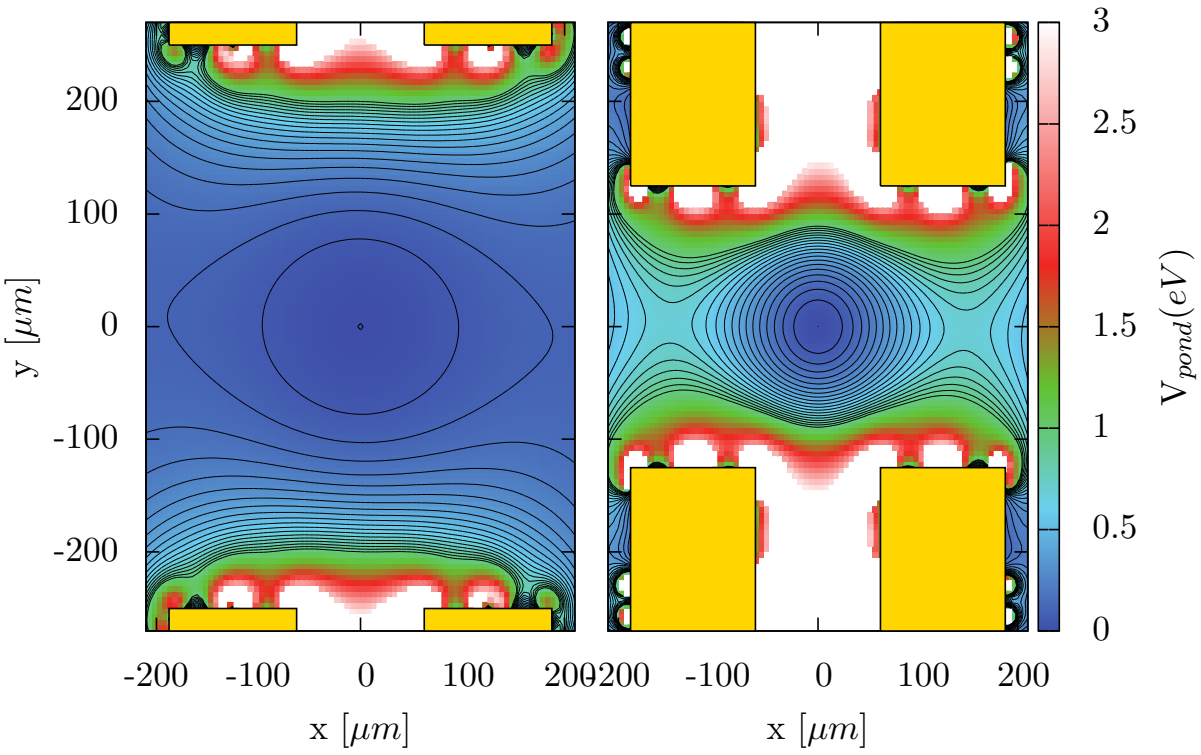

Figure 3.4.: Ponderomotive potential: The ponderomotive potential in the loading zone (left) and the processing zone (right) for usual operation parameters (440 Vpp@20 MHz). Equipotential lines are starting in the node are spaced by 50 meV.

Within the radial plane a rapid oscillating RF potential is determining the confinement properties. The best illustration of the confining behaviour is the ponderomotive potential which scales with the square of the electric Field vector $|\vec{E}|$ described in equa-

tion 3.6. In figure 3.4 the shape of the ponderomotive potential is shown in the loading and processing region. In normal operation conditions the ion is compensated to minimum micro motion and is located close to the RF node in the geometrical center of the trap. The potential is symmetric in both radial directions because no additional DC potential is applied. In case of our asymmetric trap geometry in the loading region, the shape of the equipotential lines is elliptic, but this is is circular in the symmetric processing region. Additional voltages applied at the diagonal DC electrodes lead to a tilt and deformation of the ellipse. This causes the axis of the secular motion to shift depending on the applied voltage. This effect is discussed in detail in the next section.

3.5. Dynamic Trajectory Simulation

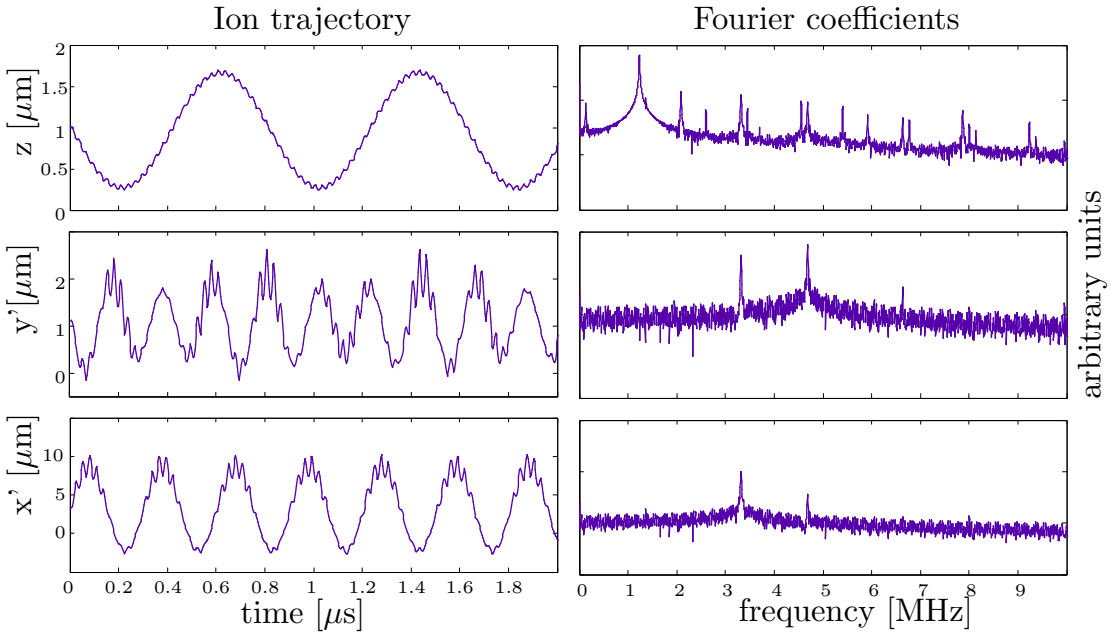

Figure 3.5.: Ion trajectory and Fourier transformation: Simulated ion trajectories on the left side and their Fourier analysis in the projected coordinate system on the right. The axial frequency component along the z axis is clearly dominant. Within the tilted radial coordinate system x' and y' one clearly recognizes both radial modes. The trajectory projection directions x' and y' with an agle of 50° to the x axis do not coincide with the oscillation main axes.

The BEM software framework [SPM+10] is also used to perform a dynamic ion trap simulation. After setting up the geometrical model of the electrode structure and solving

for the surface charge distribution, an intermediate field calculation takes place. Within a user defined 3D position grid all field components from all electrodes are calculated on the grid points. These data is stored in a cache and can be used during propagation. This allows fast calculation times for the individual propagation steps. The real field values are then determined by interpolation within the pre calculated grid. A software warning announces if the ion leaves the pre calculated area. The temporal sampling of the propagation is supposed to be more than 1/100 of one RF period, which defines the fastest timescale in the system.

In figure 3.5 the 3D trajectory of an ion with a nonzero initial kinetic energy is shown. The kineric enerty has to be chosen that the ion stays in the harmonic range of the trap. The additional freedom for the following analysis is the projection direction within the radial plane. One can choose any angle in the radial plane and project the trajectory on these possible axes of the secular motion. Using a fast fourier transform (FFT) the strength of the individual secular motions can be detected. If the projection angle corresponds to one of the main axis of the secular modes, this mode will reach a maximum amplitude while the other is vanishing. As shown in figure 3.6 the

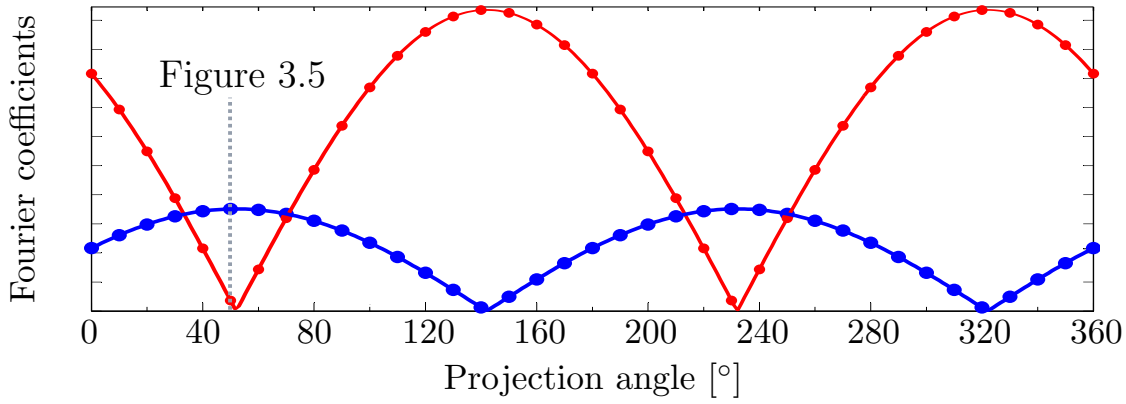

Figure 3.6.: Secular motion angle dependence: A varying projection angle changes the coordinate system and the relative size of the Fourie components of the high radial frequency and the low radial frequency. They form a ponderomotive potential ellipse with the axis tilted by 48° with respect to the x axis. These tilt corrisponds to the applied offset voltage of -4.4 V.

method reproduces separated secular modes with a right angle relation. The different heights of both Fourier components are dependent on the initial conditions and can not be interpreted further. This technique allows a precise analysis of secular oscillation modes for all possible sets of operation parameters. This simulated values vor tilt angle of the radial oscillator modes can be compared to experimental data.

The main axis tilt of the secular modes can be influenced and predicted by the DC voltage configuration. The main tool to do so is change the offset voltage of all DC

segments. This will cause an additional field superimposed with the quadrupole field of the RF drive field which leads to a tilt of the modes as shown in figure 3.7.

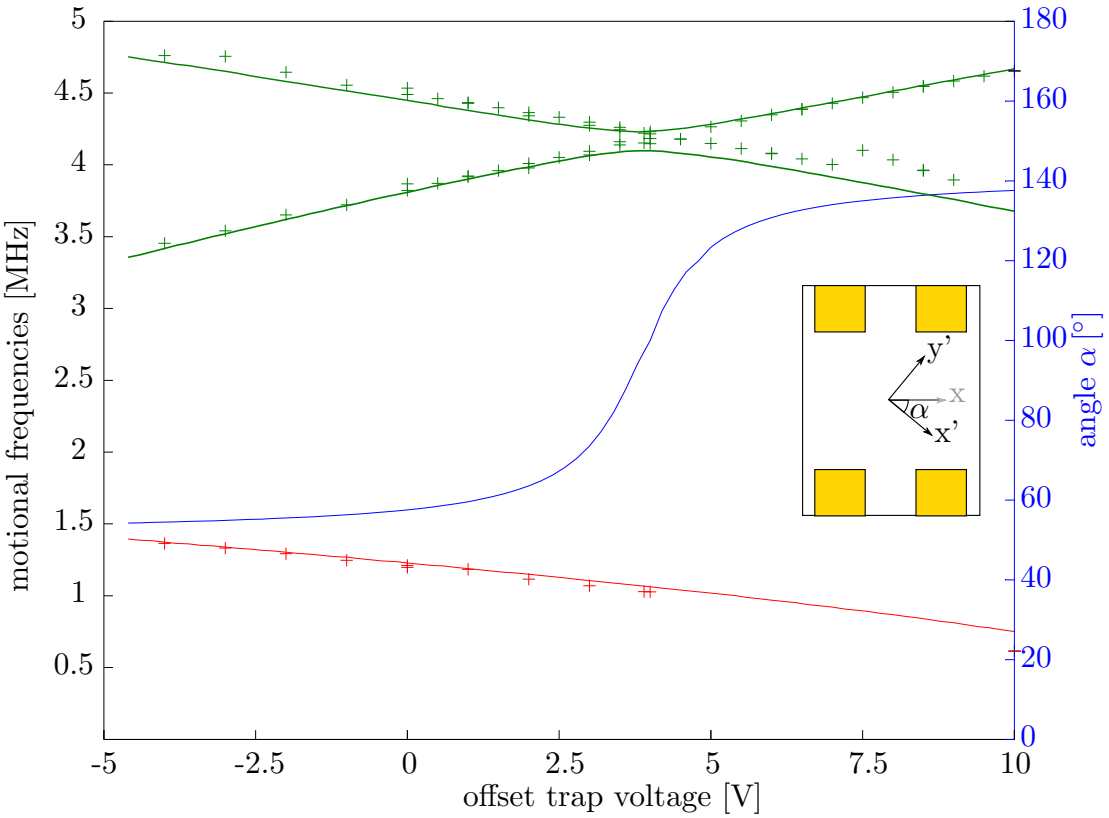

Figure 3.7.: Secular motion tilt variation: The motional frequencies under the influence of an applied offset DC voltage. Lines denote simulation data and points experimental results. The axial frequency is decreasing because of the grounded side segments 3 and 7. The radial frequncies show a transition from seperated frequencies into an degenerate range and. The elliptic potenti als is tilted by the angle and deformed close to a circle while crossing.

The restrictions for this technique are the voltage range of the supply and the stability of the trap. For the measurement in figure 3.7 a DC voltage of -5 V was used at segment 5. All segments 4,5 and 6 have been supplied with a variable additional offset voltage. The measurement of the actual trap frequency has been performed using the 729 nm spectroscopy laser described in section 4.2.2. Using this method one retrieves the information of the angle of both secular modes, which also defines the coupling strength to the spectroscopy laser at 729 nm and the efficiency of Doppler cooling. It also enables us to tune the angle or even rotate the angle dynamically during operation. The precise

simulation can be used for novel quantum simulation schemes [BAO+12, KUJ+12] as well as to determine optimized trap geometries.

3.6. Transport Voltage Determination Using Singular Value Decompsition

This section describes a technique to provide multiple voltage ramps creating a constant axial frequency for transport along the trap axis. This technique has already been described in [Zie08, SPM+10] and is outlined in section 3.6.1

3.6.1. Singular value decomposition and Thikonov regularisation

The determination of voltage configurations to realize certain transport operations is in general an inverse and ill-conditioned problem. In addition various constraints limit the realizable voltages. This problems can be targeted by a set of numerical operations. The starting point of this algorithm isthe calculated potential data from figure 3.2. This matrix A_{ij} contains the potential along all positions z_i for all electrodes j. We can now calculate any total potential $\Phi(z_i)$ by superimposing the voltage configuration U_j using

$$\Phi(z_i) = \sum_{j=1}^{N} A(z_i, j)U_j \Leftrightarrow \Phi_i = \sum_{j=1}^{N} A_{ij}U_j, \quad i = 1...M, \tag{3.7}$$

Where N denotes the number of segments in the simulation and M being the amount of points along the trap axis. This defines the inverse problem to be solved. We seek to determine the voltage configuration creating a defined harmonic potential. The potential is characterized by a parabola with defined minimum position z_0, potential offset and curvature C_z to determine the axial frequency ω. Since M is larger than N the problem can be reduced to the region where the potential minimum is desired to be. This over determined matrix problem is prone to diverging terms if a standard inversion algorithm is used. There are many electrodes with negligible effect on the potential at position z_0, which causes divergent terms due to singularities in the inverse. For simplicity the indices are omitted and it is always assumed that A is an $M \times N$ dimensional matrix while $\vec{\Phi} = (\Phi(z_1), \Phi(z_2), \ldots, \Phi(z_M))^T$ and $\vec{U} = (U_1, U_2, \ldots, U_N)^T$ are vectors. The whole problem boils down in finding an approdimate inversion A^{-1} to solve the relation

$$\vec{U} = A^{-1}\vec{\Phi}. \tag{3.8}$$

This problem is very common in physics and has to be solved often when noisy data is to be described by a linear system, and many data points are recorded which determine a small set of parameters. This class of problems is called *inverse problems*, and if singularities occur then they are called *ill-conditioned* inverse problems.

To realize the inverse matrix A^{-1} where the singularities are accessible for regulation, a singular value decomposition (SVD) is used. This operation decomposes the matrix A into a product of three matrices $A = USV^T$, where U and V are unitary matrices and S is a diagonal matrix with diagonal entries s_i. The inverse matrix can now be reconstructed by $A^{-1} = VS^{-1}U^T$. It is obvious why the diagonal elements $S_{ii}^{-1} = 1/s_i$ are called *singular values*. Values s_i close to zero lead to a diverging term in the inverse matrix and have to be suppressed.

The Tikhonov regularization method is a way to suppress diverging terms by replacing the singular values with the expression $s'_i = \frac{s_i}{s_i^2+\alpha^2}$. Using the regulation parameter α, this leads to a suppression of diverging terms which occur mainly for far distant segments. To ensure that inversion still represents the initial matrix within the spacial limits, the following expression is minimized with respect to the solution $\vec{U}$:

$$\left|\left|A'\vec{U} - \vec{\Phi}\right|\right|^2 \tag{3.9}$$

Using the reconstructed matrix $A' = US'V^T$ ensures a proper choice for the inversion in the relevant range. This minimization has to be performed for each transport step and individual potential parameters.

The general application for this algorithm is a set of voltage configurations U_i wich corrispond to translated potentials at equidistant positions z_i long the trap axis. The algorithm will generate constant axial frequency and the same potential offset for all voltage sets. To realize a smooth transport over the whole ion trap one additional constrained has to be added to the minimisation constraint. The term

$$\alpha|U - U_{i-1}| \tag{3.10}$$

is introduced to obtain the solution with the least change relative to the last solution U_{i-1}.

The last point to deal with is the limited range of the voltage supply. One has to suppress solutions with over limit voltages during the transport. This is done iteratively by rescaling the initial potentials according to the found solution. With an out of range voltage u_j the matrix element $A'_{ij} = \beta_j A_{ij}$ is decreased by the factor $0 < \beta_j < 1$ for all positions j. The final output voltage is then rescaled by the factor $1/\beta_j$ which influences the creation of the potential. The rerunning algorithm desires to generate an even higher voltage u_j, which is then suppressed by the additional minimisation term in equation 3.10. The iterative decreasing of β_j for all relevant electrodes produces a realisable solution.

This algorithm enables the calculation of continuous voltage ramps using all DC segments, guaranteeing transport through the whole ion trap at constant potential parameters. The result will be in the output range of the power supply and can be realised at the ion trap. The generated smooth voltage ramps allow interpolation of intermediate

positions with high precision. This technique was used to achieve experimental results in a 3D ion trap, published in [HZP+10] and described in section 6.1.1. In planar ion traps this method was used and published in [NDM+11] the results are described in detail within the next section.

3.6.2. Transport Simulation in Planar Ion Traps

The algorithm from the last section can be used with minor adaption in planar ion traps as well. One realized simulation and transport experiment has been published in collaboration with the ion trap group of the University of California, Berkeley[NDM+11]. The significant difference to symmetric 3D ion traps is the information about the exact position of the ion inside the trap. In planar traps this position can not be assumed in the geometrical center of the electrode structure, it is rather influenced strongly by border effects from the limited trap length. The ending RF electrodes cause a significant influence on the ions height above the surface. The ions hight influences strongly the potential strength of the individual DC electrodes. The varying ion electrode distance during transport leads to a complex DC potential behaviour along the axial path of the ion.

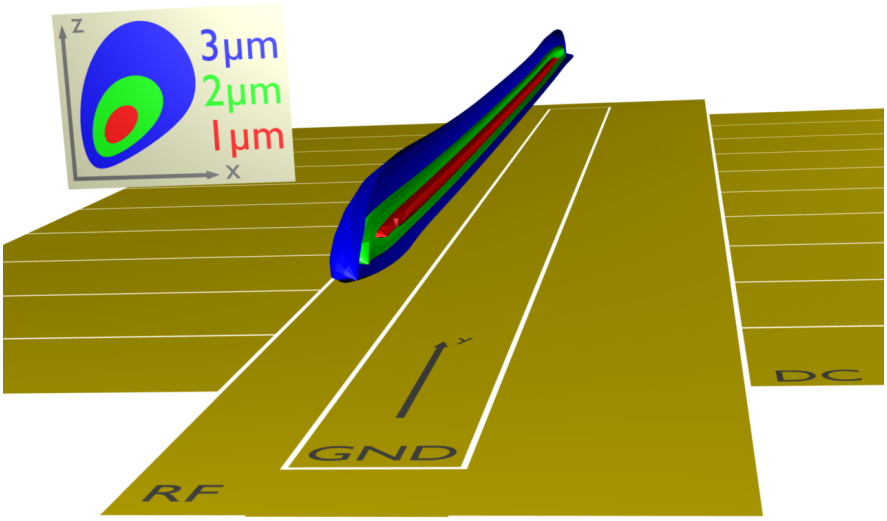

Figure 3.8.: Ponderomotive potential in a planar ion trap: The electrode geometry of a planar ion trap with RF, DC and GND electrodes. The coloured faces highlight the strength of the ponderomotive potential using the residual micromotion amplitude. They have been sliced by 90 degrees to show the inner structure. The cut through the z-x plane illustrates the tilt of the main axis in the axial center of the trap.

The starting point for a SVD simulation is always the determination of the potential matrix A. To do so the position of the RF node in the radial plane has to be determined along the axis of the ion trap. In figure 3.8 the used electrode structure is shown together with different ponderomotive equipotential planes. The planar trap uses an asymmetric and closed RF electrode to tilt the oscillation main axes of the radial modes. This can be seen by the cut through the ponderomotive potential. The multiple DC electrodes on each side of the RF electrode are used to generate the transport potential. The strength of the ponderomotive potential can be measured in micromotion amplitude for practical reasons. This measure is directly proportional to the electric field vector length and was measured in section 6.1.3. Once the RF node is determined through the trap a normal SVD and Thikonov regularisation algorithm is used to determine the necessary transport information. A result is shown in figure 3.9, where all segment voltages are shown to generate a potential minimum at a desired axial position. It is clearly recognizable that the electrode close to the desired minimum position contributes the main part of the potential. The irregularities at the axial border positions are produced

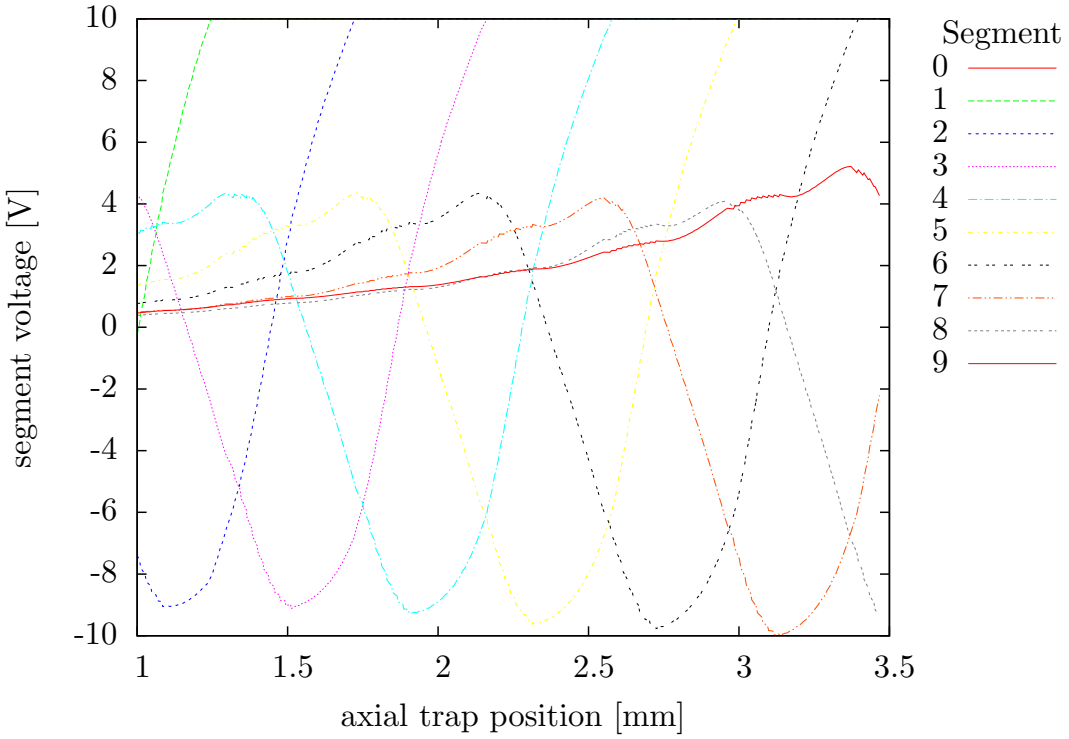

Figure 3.9.: Transport segment voltages: All required sesgment voltages to generate a defined axial confinement at the desired axial trapping position.

by the changing ion hight above the electrodes.

The main disadvantage of this technique is that smooth voltage ramps are only possible within one calculation set. It only allows one kind of transport parameters per voltages set. It is not possible to realize *split* and *merge* operations using this voltage sets. A scalable algorithm allowing the multiplexing of all kinds of transport operations is described in the next section.

3.7. Simplified Scheme for Concatenated Transport Operations

A general set of transport voltage ramps which can be concatenated for complex operations is one important step towards transport based quantum computing. The preferred way to do so is to separate all operations in the smallest logical unit and solve these. If a transport from one electrode to the next is possible with high fidelity, several of these operations can be concatenated to realize long distance transports. Even complex operation like *splitting* and *merging* of ion crystals can be included to the framework.

The starting point is again potential data obtained from numerical simulation as shown in figure 3.2. For the 3D trap described in section 2.1 the high translation symmetry within the loading and the processing region leads to the assumption that one segment transport voltages will not differ much from one segment to the neighbouring. This leads to an approach which bases on one type of transport voltage ramp describing the transport from segment i to segment $i+1$ which can be inverted to reach segment $i-1$ and concatenated to get to segment $i+j$. A simplified model is used where segment i is located at $z=0$ and segment $i+1$ at $z=1$. The maximum trapping voltage can also be rescaled to start at -1 and end at 0. The potential data of two neighbouring electrodes is used to numerically solve the equation of motion for one ion with constant axial frequency:

$$\xi_{const} = \frac{\omega^2 m}{2e} = \xi(z, U_i, U_{i+1}) \tag{3.11}$$

$$0 = E_z(z, U_i, U_{i+1}) \tag{3.12}$$

The curvature ξ and the axial electric field component E_z are obtained from the potential data along the whole distance between the segments. The potential minimum will always correspond to a zero of the electric field E_z. These equations are solved along the z-Axis. This will provide two voltage ramps $U_i(z)$ and $U_{i+1}(z)$ which are shown in figure 3.10. These voltage ramps can now be rescaled to real voltages. The peak value defines the maximum scaling factor to obtain voltage ramps within the limitation of the power supply.

For real usage of these functions the transport has to be broken down in realizable discrete steps and timed in the desired way. Furthermore the timing of $U(z(t))$ offers multiple opportunities. One can think of a linear transport ramp $z(t) = t$ or a sine square ramp $z(t) = \sin(\pi/2\ t)^2$. The effects of different transport shapes are described

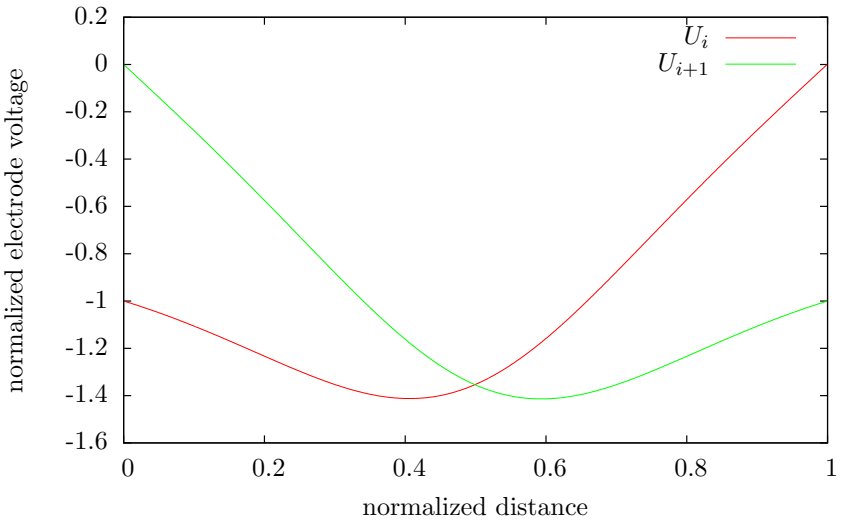

Figure 3.10.: General transport voltage function: The voltage function of two generic electrodes in the loading region realizing a axial frquency perserving transport.

in detail in section 6.3. Further parameters for the realisation of the transport are the sample number, update rate of the DACs and the maximum trapping voltage. These values can be chosen in the experiment control software and do not require any further simulation.

4

Qubit Implementation and Development of a Universal Toolbox of Operations

This chapter describes the laser-driven operations on trapped ions. The basic electronic operation conditions have already been described in section 2.4 so we will now focus on the laser interaction. First a short introduction on ion trapping and incoherent laser interaction is given in section 4.1. These operations allow the internal state preparation and detection as well as Doppler cooling of the trapped ions. In section 4.2 the coherent manipulation of the qubit is described in detail before several methods for motional energy measurement are described in section 4.3.

4.1. Trapping, Initialization and State Detection of Ions

The basic laser interactions for Doppler cooling are described in section 4.1.2. This process builds the foundation of all further ion operations, as the preparation of spin states and the internal state discrimination. The *electron shelving* technique is discussed in section 4.1.3, which is a fast and precise method to determine the electronic state of the ion.

First we will take a look at the creation of calcium ions inside the trap. A neutral beam of Ca atoms is emitted from a heated oven operated at 3.3 A and passes the ion trap. A resonantly enhanced two photon ionisation process takes place inside the ion trap and leaves Ca^+ ions with there initial kinetic energy in the trap. The trapped ions are Doppler cooled and there scattered light can be observed using the EMCCD

camera. The Ca^+ ion posesses one valence electron and therefore displays an energy

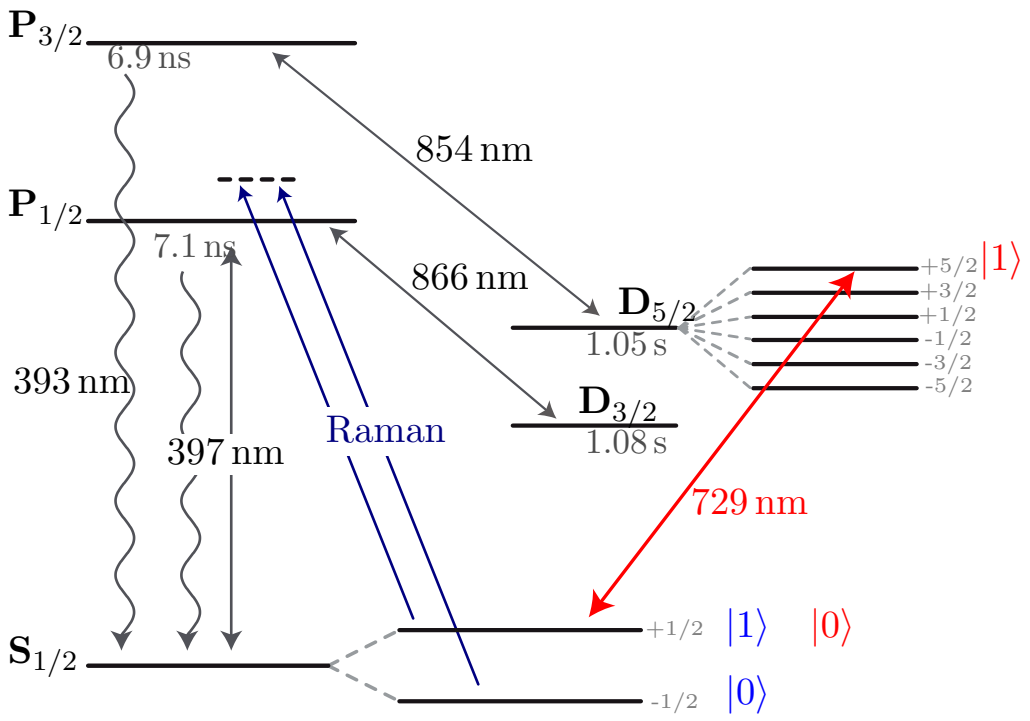

Figure 4.1.: Calcium level scheme: Laser sources as straight lines and emitted light from the ion as wavy lines. The two qubit implementations are the optical qubit in the ground and metastable state, and the spin qubit addressing the individual Zeemann levels declared with the magnetic quantum numbers m_j.

level scheme similar to Alkaline atoms shown in figure 4.1. All laser sources and emitted wavelengths of the trapped ion are shown. The laser at 397 nm is used for Doppler cooling, state preparation and detection. It requires the repump lasers at 866 nm, which is used to avoid population of the metastable states during Doppler cooling and state preparation. The additional lasers at 729 nm and the Raman laser beams are used to generate two independent qubit representations. They optical qubit requires the small natural linewidth of the metastable state $D_{5/2}$ to perform operations using the laser at 729 nm. The metastable $D_{5/2}$ state is repumped by the laser at 854 nm. The stimulated Raman transition is driven by two laser beams at 397 nm and is used to perform operations like sideband cooling and complex motional detection schemes.

4.1.1. Basic Light Ion Interaction

The basic interaction of light with two electric levels of an atom can be described as follows. The ground state $|g\rangle$ and excited state $|e\rangle$ are coupled by a monochromatic laser beam described by the electric field

$$\vec{E}(t) = \vec{E}_0 \cos(\omega_l t) \tag{4.1}$$

with the amplitude $\vec{E}_0 = E_0\vec{\epsilon}$ including the polarisation vector $\vec{\epsilon}$. To obtain this expression the dipole approximation is used, which eliminates the spacial position of the ion relative to the laser source. The Schrödinger picture Hamiltonian then consists of two parts:

$$i\hbar\frac{d}{dt}\psi = \hat{H}\psi = (\hat{H}_0 + \hat{H}_i)\psi \tag{4.2}$$

$$\psi = c_g\,|g\rangle + c_e\,|e\rangle \tag{4.3}$$

The atom Hamiltonian $\hat{H}_0$ and the interaction Hamiltonian $\hat{H}_i$, which act on the wave function defined by the parameters c_e and c_g.

4.1.2. Doppler Cooling

Doppler cooling was first proposed simultaneousls by Hänsch, Schawlow [HS75] and Wineland, Dehmelt [WD75] in 1975. A red detuned laser beam interacts under the Doppler shift with a moving atom. If the atom moves towards the direction of the laser beam it realizes a Doppler shifted laser frequency. Therefore, a photon scattered in a random direction leads to an effective momentum transfer in the direction of the laser beam. This effect vanishes if the Doppler shift exceeds the transition linewidth. The optimum Doppler cooling is achieved with a detuning $\delta = \Gamma/2$, reaching the Doppler cooling limit of

$$k_b T_{Dop} = \frac{\hbar\Gamma}{2} \tag{4.4}$$

Where Γ is the natural linewidth of the transition. For our experiment this value corresponds from 10 to 30 phonons, dependent on multiple parameters, like the trap frequency and the saturation parameter. Different saturation parameters are used to achieve an efficient dual use of the laser source at 397 nm. A laser power of 10 μW is used for Doppler cooling and a significantly increased laser power of 115 μW is used for detection (see also section 4.1.3).

To optimize all parameters for efficient cooling and fast detection the Doppler and repump spectrum was analysed together. Like shown in figure 4.2 the fluorescence of the ion changes dependent of both detunings. The two visible dark resonances illustrate that the Zeemann substructure of the electronic states has to be taken into account. This multi level system also depends on the applied magnetic field which influences the

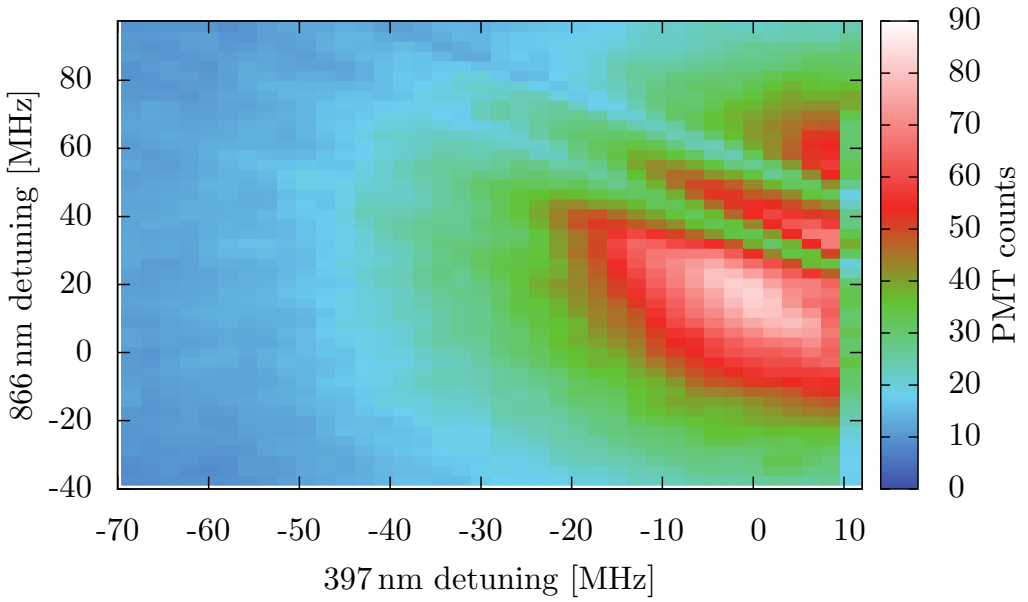

Figure 4.2.: Measured two dimensional fluorescence spectrum: The fluorescence light of the ion was detected using 10 averages on 10 ms PMT windows while 130 μW Doppler laser at 397 nm and 170 μW repump laser at 866 nm are changed in frequency. The dark resonance structure occurs because ofthe multi level structure. The frequency axis are calculated from wavemeter values for each measurement point.

Zeeman splitting of the ground state and the excited states. Due to the additional use of the laser source at 397 nm for detection, the optimum choice for both wavelengths is close to the maximum of the emitted fluorescence at the origin of figure 4.2. This saturated fluorescence scan shows a broad maximum where equivalent detection parameters are found for 10 MHz range of the laser at 397 nm and 20 MHz of the laser at 866 nm.

A reduction in laser power is used creating less saturation broadening and allow Doppler cooling to 18 Phonons as shown in figure 4.7. This corrisponds to 2.5 times the theoretical Doppler limit (7.5 Phonons for $\omega_z = 1.4$ MHz) and is a reasonable value for micro traps.

The maximum fluorescence value is relevant for the detection count rates described in the next section.

4.1.3. Electron Shelving Measurement Scheme

The internal state measurement is done by fluorescence detection and requires a high count rate difference on two electronic states. In Ca ion states, used for encoding the optical qubit are the groundstate $S_{1/2}$ and the metastable state $D_{5/2}$. There decay rates differ by about 8 orders of magnitude, which enables fast and precise state detection. In figure 4.3 a measured histogram is shown, which is used as a calibration source for the ion fluorescence count rate and the background count rate. The two peaks correspond to a bright ion with high count rates and a dark ion with low count rates mainly produced by background light scattered from the trap electrodes. The detection time is usually chosen to be 2 ms with a saturated laser power of 150 μW at the ion (see also table C.1). A usual way to obtain this fluorescence data is to produce the dark ion state on purpose by switching off the repump laser at 866 nm while irradiating the Doppler laser at 397 nm. The ion will end up in the meta stable $D_{3/2}$ state and show similarly no fluorescence as if it would be in the $D_{5/2}$ state. This calibration data is used to determine a detection threshold for subsequent measurements.

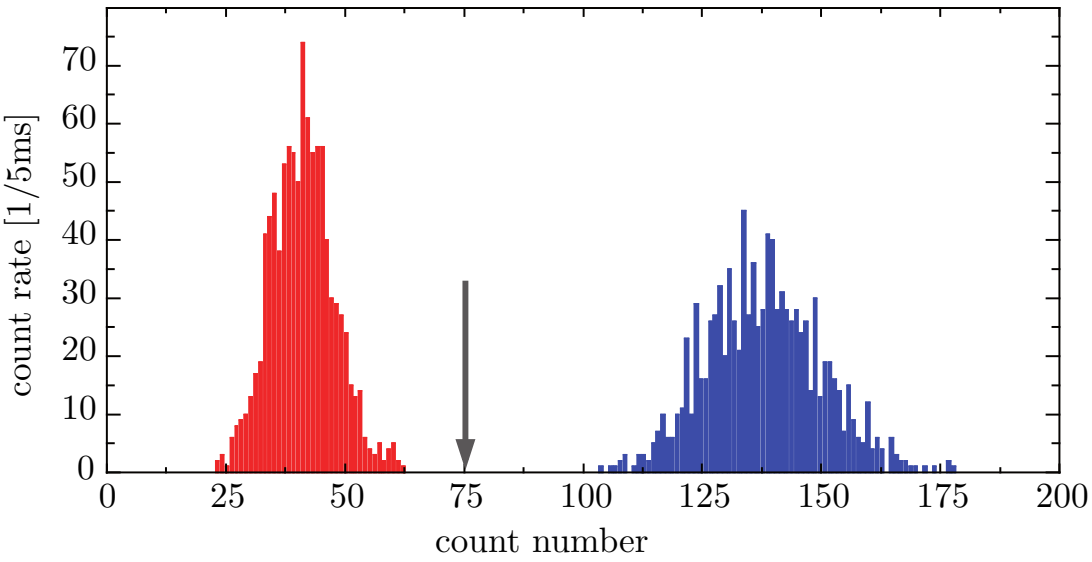

Figure 4.3.: Fluorescence histogram: The two peaks occur from dark ion produced by switching off the repump laser at 866 nm and from bright ion. The defined threshold at 75 counts is used as reference in further measurements.

The measurement scheme of a typical measurement consists of ion state preparation, state manipulation and fluorescence measurement. For simple spectroscopy, as example the spectroscopy laser frequency is varied which leads to a frequency dependent excitation of the meta stable state. This manipulated state is now analysed by fluorescence detection. The excitation probability is calculated from multiple repetitions of identical measurements.

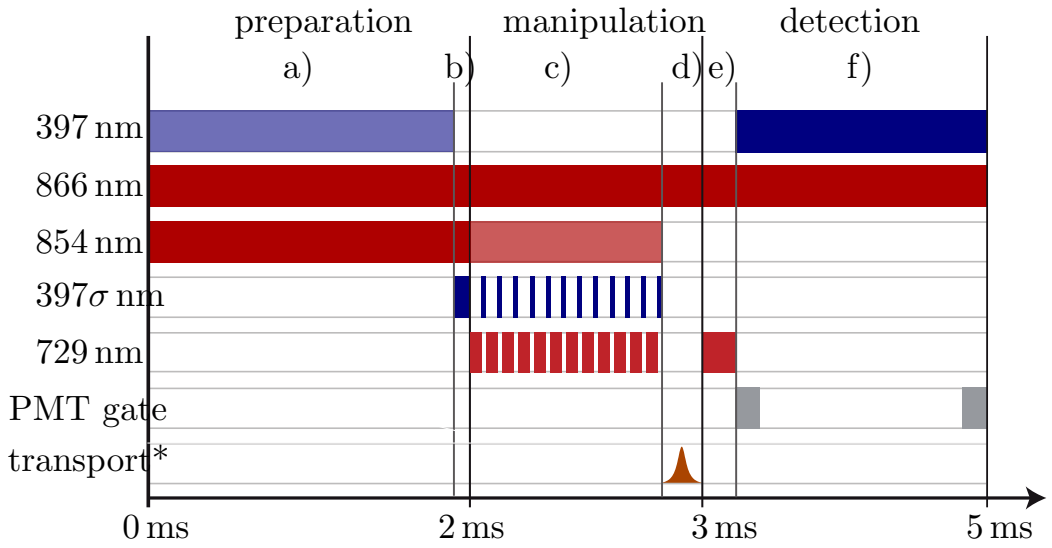

Figure 4.4.: Measurement sequence: Different colours indicate a different laser power. The state preparation is done by a) Doppler cooling and b) optical pumping. The ion can now be manipulated to perform c) sideband cooling and d) transport operations. The final e) 729 nm pulse is used to obtain information about the created state which is f) detected afterwards. (*) this state manipulation can be replaced by various other operations as described in text.

Each measurement consists of a series of laser pulses as shown in figure 4.4. The basic principle is fiven by the following sequence:

a) Doppler cooling is used to cool the ion close to the Doppler limit. The high scattering rate ensures a defined temperature, even for short pulse times of about 2 ms.

b) Optical pumping populates the $m_j = +1/2$ ground state with a fidelity of 95 % using circularly polarized light.

c) Ground state cooling is performed by repetitive excitation on the red sideband (RSB) transition using the spectroscopy laser at 729 nm while the repumper at 854 nm leads to a fast decay to the ground state. Each excitation and decay cycle reduces the phonon number by one. Interleaved optical pumping prevents hiding in a non coolable state. This *sideband cooling* is always concluded by one optical pump step to generate a defined state.

d) Transport operation or dark wait time for heating rate measurements can be performed with the ground state cooled ion.

e) A pulse at 729 nm performs excitation to the meta stable state with a certain probability. For spectroscopy, the laser frequency is changed, while for Rabi oscillations the pulse length is varied.

f) Fluorescence analysis detects the internal state of the ion. The binary information corresponds to $S_{1/2}$ if a high count rate was detected and to $D_{5/2}$ otherwise.

This measurement is repeated N times with the same parameters to estimate the excitation probability of the meta stable state $P_D = n_d/N$ with the number of dark ocurrences n_d. The total measurement number N determines the error for this statistical measurement. While for normal spectroscopy 20 measurements are suitable some high precision evaluations use up to 2000 measurements with equal settings. The standard error is given by [Pos10]

$$\sigma(P_D) = \sqrt{\frac{P_D(1-P_D)}{N}}. \tag{4.5}$$

This measurement scheme relies on the fact that all measurements with the same settings are prepared identical. Fluctuations of the various control parameters give rise to systematic errors and increase statistical errors. Obtaining the fluoresence data, even post evaluation is possible by generating a histogram from all measured fluorescence data.

4.2. Internal State Manipulation

To operate the ion in the resolved sideband regime and drive coherent dynamics on electronic states requires to be within the Lamb-Dicke regime $\eta\sqrt{\bar{n}} << 1$. This requires a cold ion with a low mean phonon number $\bar{n}$ weighted with the Lamb-Dicke parameter as explained in the next section.

4.2.1. Coherent Dynamics

To perform coherent dynamics, we continue from equation 4.2, using the rotating wave approximation (RWA) along the discussion in [Pos10] and end up with the well known *Rabi oscillations* for resonant laser light

$$P_e(t) = |c_e(t)|^2 = \sin^2(\Omega t/2). \tag{4.6}$$

The population of the excited state P_e oscillates with the Rabi frequency Ω. The *pulse area* $\Theta = \Omega t$ is used as simplified definition. A π-pulse, with $\Theta = \pi$ would cause a state transfer from $|g\rangle$ to $|e\rangle$, while a $\pi/2$-pulse creates a balanced superposition of ground and excited state.

If one includes a motional mode of a harmonic oscillator the quantum state of the ion can be written as

$$|\psi\rangle = \sum_n c_{g,n} |g,n\rangle + \sum_n c_{e,n} |e,n\rangle \tag{4.7}$$

The harmonic oscillator folded with the two electronic ion states is illustrated in figure 4.5. They form a phonon ladder with different transition frequencies $\omega_{ge}+m\omega_z$, $m \in \mathbb{Z}$ and different Rabi frequencies $\Omega_{n,n+m}$ for the transition $|g,n\rangle \rightarrow |e,n+m\rangle$. If we assume a ground state wave function with a certain phonon distribution p_n the Rabi oscillations take the form

$$P_e(t) = \sum_n |c_{e,n}(t)|^2 = \sum_n p_n \sin^2(\Omega_{n,n+m}t/2). \tag{4.8}$$

This 'averaging' over oscillations with different frequencies result in dephasing Rabi oscillation, dependent on the phonon distribution.

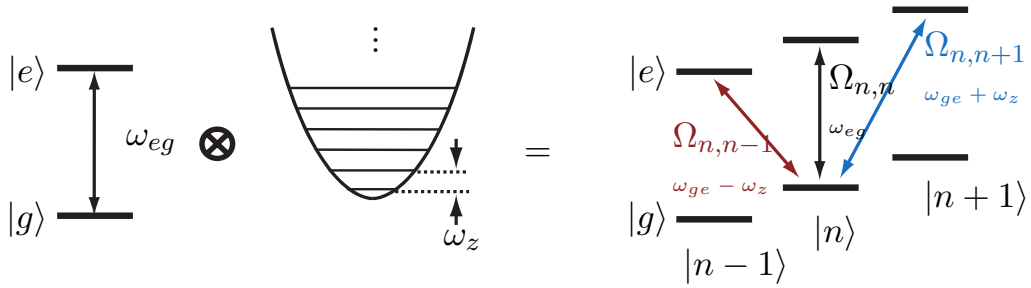

Figure 4.5.: Harmonic oscillator ion states: On the left side are the separate systems, two level ion and harmonic oscillator. The right side shows the quantum state representation with different coupling Rabi frequencies and transition frequencies.

The full description of $\Omega_{n,n+m}$ is given in section 4.3, as approximation within the Lamb-Dicke regime one finds

$$\Omega_{n,n} = \Omega_{\mathrm{CAR}} \approx \Omega, \tag{4.9}$$
$$\Omega_{n,n+1} = \Omega_{\mathrm{BSB}} \approx \eta\sqrt{n+1}\Omega, \tag{4.10}$$
$$\Omega_{n,n-1} = \Omega_{\mathrm{RSB}} \approx \eta\sqrt{n}\Omega. \tag{4.11}$$

Please note the dependence of n for the sideband transitions. In contrast to the blue sideband (BSB), the RSB Rabi frequency vanishes for $n = 0$ and can not be driven. This corresponds to the lower end of the phonon ladder. The *Lamb-Dicke parameter* $\eta = |\vec{e}_z\vec{k}|\sqrt{\hbar/2m\omega_z}$ determines the coupling strength of the laser to the motional mode.

For the spectroscopy laser at 729 nm one finds a Lamb-Dicke parameter of $\eta \approx 0.07$ for typical axial frequencies of $\omega_z = 1.3\,\mathrm{MHz}$. The projection $|\vec{e}_z\vec{k}| = k\cos(\phi)$ of the laser direction on the motional mode directly influences the coupling. The low Lamb-Dicke parameter occurs from $\phi = 45\,^\circ$ for the spectroscopy laser and the long wavelength of the laser. All experimental data obtained using this measurement technique is labled with the D-state excitation probability P_D.

The two laser beams at 397 nm driving a simulated Raman transition from $|\downarrow\rangle$ to $|\uparrow\rangle$ have an effective k vector parallel to the axial mode. This maximises the projection and leads to a Lamb-Dicke parameter of $\eta \approx 0.21$. This large coupling to the axial mode leads to fast sideband oscillations which facilitate sideband cooling and working on motional transitions. In addition the projection to the two radial modes vanishes which eliminates possible dephasing effect on the Rabi oscillations. More details on stimulated Raman transition can be found in [Pos10]. All measurements obtained using the simulated Raman transition are labelled with the Raman transition probability $P_\uparrow$.

4.2.2. Sideband Resolved Spectroscopy

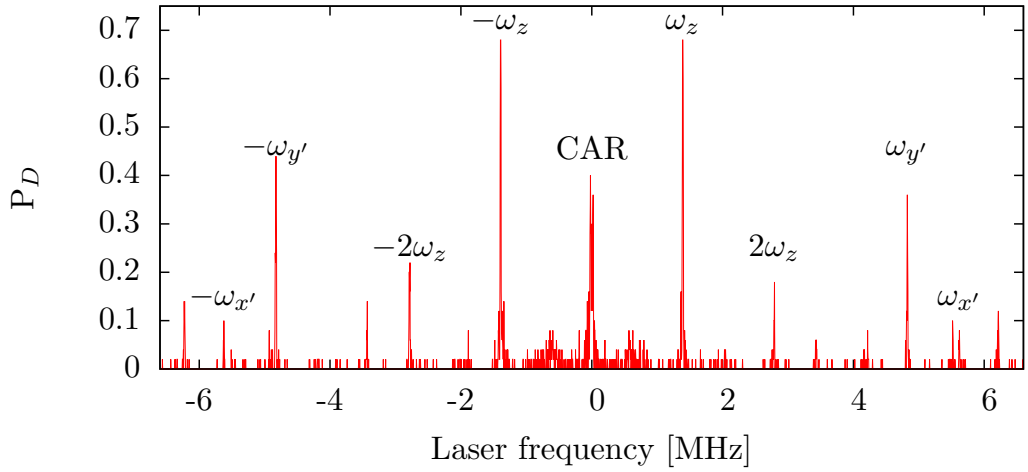

Figure 4.6.: $D_{5/2}$-State spectrum with motional sidebands: Frequency dependent $S_{1/2,m_j=1/2} \rightarrow D_{5/2,m_j=5/2}$ state excitation using the laser at 729 nm. The transition carrier and its motional sidebands are labeled ($\omega_z = 1.39\,\mathrm{MHz}$, $\omega_{y'} = 4.82\,\mathrm{MHz}$ and $\omega_{x'} = 5.62\,\mathrm{MHz}$). All transitions below zero are red sidebands (RSBs) and all above are blue sidebands (BSBs) transitions.

The basic measurement technique is used to determine the relevant transitions using spectroscopy. The laser at 729 nm is changed in frequency using the state measurement scheme described in section 4.1.3. Excitation P_D is possible if the laser frequency

corresponds to an atomic transition frequency or one of its motional sidebands. The signal in figure 4.6 can be used to determine the motional frequencies by observing the sideband distance to the carrier. An advanced motional mode analysis can be found in section 3.5.

The amount on observable motional sidebands is dependent laser power, motional excitation and the Lamb-Dicke parameter. The complexity of this setting limits the information obtained by such a spectrum to the motional frequencies. This information can be used to optimize trap operation parameters.

The same laser sequence can be used with fixed frequency and variable spectroscopy pulse length. One obtains Rabi oscillations like in figure 4.7 for a Doppler cooled ion.

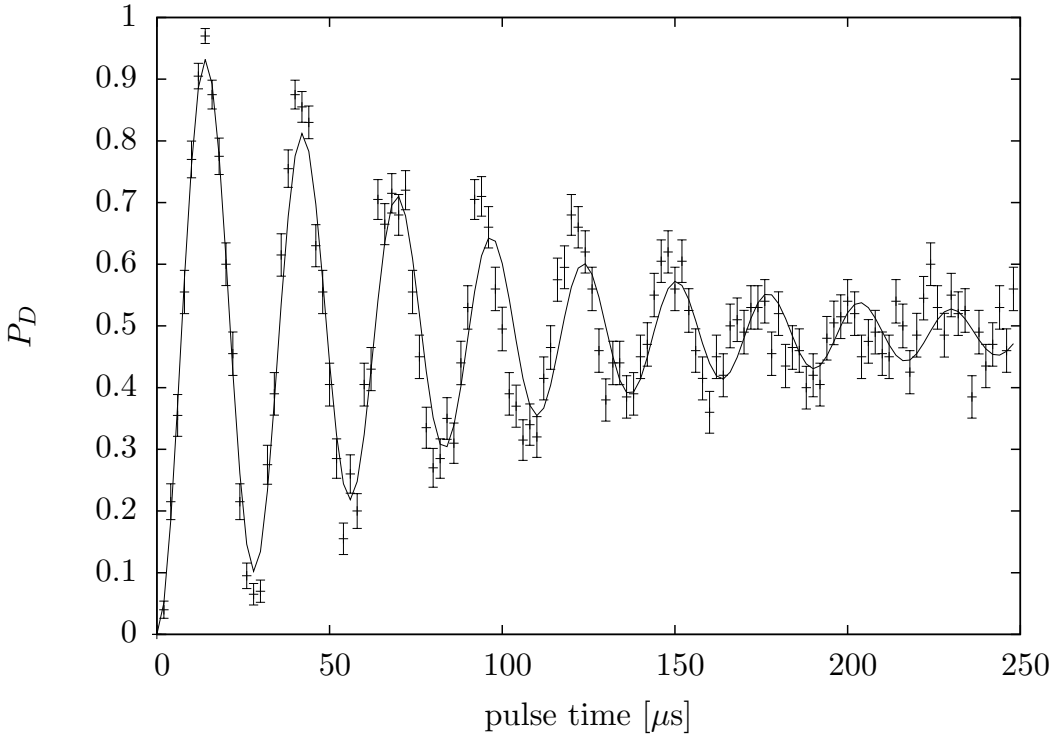

Figure 4.7.: $D_{5/2}$ state Rabi oscillations: This CAR transition of a doppler cooled ion showns a dephasing consitend with $\bar{n} = 18$ on the axial oszillation mode.

The spectroscopy data builds the foundation for further operations on the determined transitions. The pulse width scan is used for advanced techniques like energy measurement described in the next section.

4.3. Energy and Phonon Distribution Measurement

There are several methods to measure the motional energy of trapped ions. For the high energy range from the Doppler limit up to ≈5 meV the *Doppler recooling* method [WEL+07] is well suited. It analyses the fluorescence dynamics during Doppler cooling. This method can be used to analyse high heating rates as well as high transport energy transfer [GHSK08].

For the energy range of ground state cooled ions till $\bar{n} \approx 200$ coherent operations dependent from individual phonon numbers have to be used. The most general technique uses no additional information on the phonon distribution and determines each phonon occupation probability separately, as described in section 4.3.2. This technique is time consuming and limited to low phonon numbers. It is mainly used to study states involving a rather limited range of phonon number, as described in section 5.4 and in section 6.2.3.

If we assume a defined probability distribution, like a thermal or coherent distribution or a convolution of these two, phonon numbers up to 1000 can be included in the model. The measurement always relies on the phonon excitation dependence of the transition Rabi frequencies $\Omega_{n,n+m}$. Several motional transitions, like higher order RSB or BSB transitions can be used to obtain information with different dependence on the phonon number. For each transition as pulse width scan is performed, obtaining Rabi oscillations, According to equation 4.8. The Rabi frequency $\Omega_{n,n+m} = M_{n,n+m}\Omega_0$ is given according to [CG69], it depends on the coupling matrix element

$$M_{n,m} = \langle n+m| e^{ik\hat{x}} |n\rangle = e^{-\eta^2/2}(i\eta)^{|m|}\mathcal{L}_n^{|m|}(\eta^2)\left(\frac{n!}{(n+m)!}\right)^{\mathrm{sign(m)}/2} \tag{4.12}$$

While the bare Rabi frequency Ω_0 is from the ground state phonon neutral transition. The main components of the matrix elements are the Lamb-Dicke factor $\eta = k\sqrt{\hbar/2m\omega_z}$ and the associated Laguerre polynomials $\mathcal{L}_n^{|m|}$. The matrix elements shown in figure 4.8 left are mainly used for phonon distribution in the low energy range ($\bar{n} < 5$), for higher mean phonon numbers one uses higher order motional sidebands. This enables the choice of transitions with most contrast of the matrix elements for the desired phonon range.

4.3.1. Temperature Measurement using the Rising Slope Method

For some measurements a full modelling of the Rabi oscillations is not required. The *rising slope* method uses a sine approximation for small pulse area arguments of equation 4.8. This method can also be implemented as just in time energy measurements for known distributions. It is also recommended for systems with fast dephasing Rabi

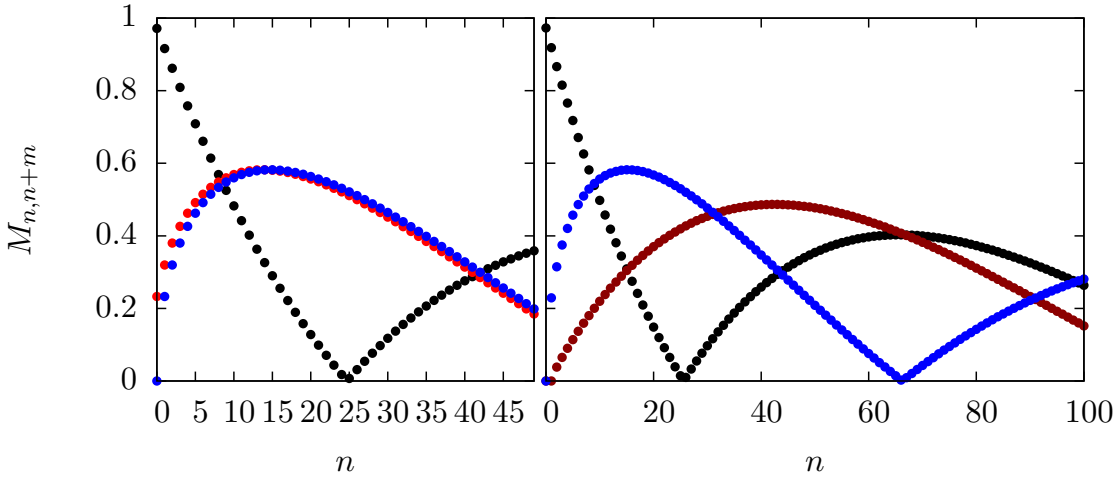

Figure 4.8.: Transition matrix elements: The matrix elements for the CAR transition (m=0) the first RSB (m=-1), the second RSB (m=-2) and the BSB (m=+1) for the stimulated Raman transition with $\eta = 0.21$. The left configuration is used for low phonon number while the right is used for high phonon excitations.

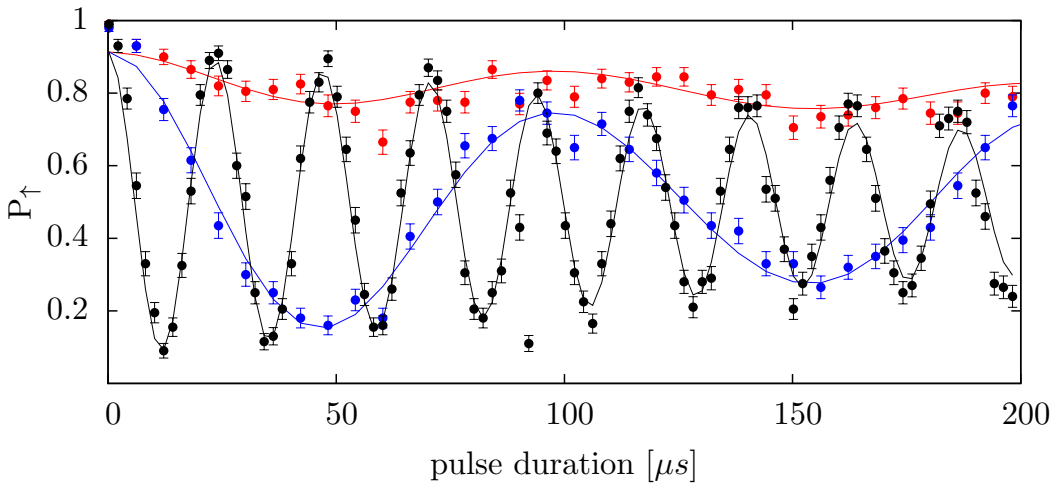

Figure 4.9.: Rabi Oscillations for a near ground-state cooled ion: The oscillations on the stimulated Raman transition of the CAR, RSB and BSB transition correspond to a thermal distribution with $\bar{n} = 0.10 \pm 0.01$.

oscillations. If for example the heating rate is on the order of the π time the increasing temperature leads to an additional dephasing while taking full oscillations like in figure 4.7.

Using the small-angle approximation where $\Omega_{n,n+m}t/2 \ll 1$ we get

$$P_e(t) = \sum_n p_n \sin^2(\Omega M_{n,n+m} t/2) = t^2 \frac{\Omega^2}{4} \sum_{n=0}^{N} p_n M_{n,n+m}^2 = t^2 \frac{\Omega}{4} \tilde{M}_m(\bar{n}) \tag{4.13}$$

with an *effective Matrix element* function $\tilde{M}_m(\bar{n}) = \sum_{n=0}^{N} p_n(\bar{n}) M_{n,n+m}^2$ only dependent on the used transition m and the mean phonon number $\bar{n}$ of the phonon distribution. This matrix element can be pre calculated using the known Lamb-Dicke parameter for the used transitions m. A pulse width scan with an experiment number of 2000 is performed to determine the curvature of the parabola in equation 4.13. In figure 4.10 four different measurements are shown with different wait times after Doppler cooling, leading to different ion temperatures. In addition always two signals from CAR and BSB are measured to eliminate the bare Rabi frequency Ω. To fullfill the small-angle approximation only excitation probabilities below 0.15 are used in the evaluation.

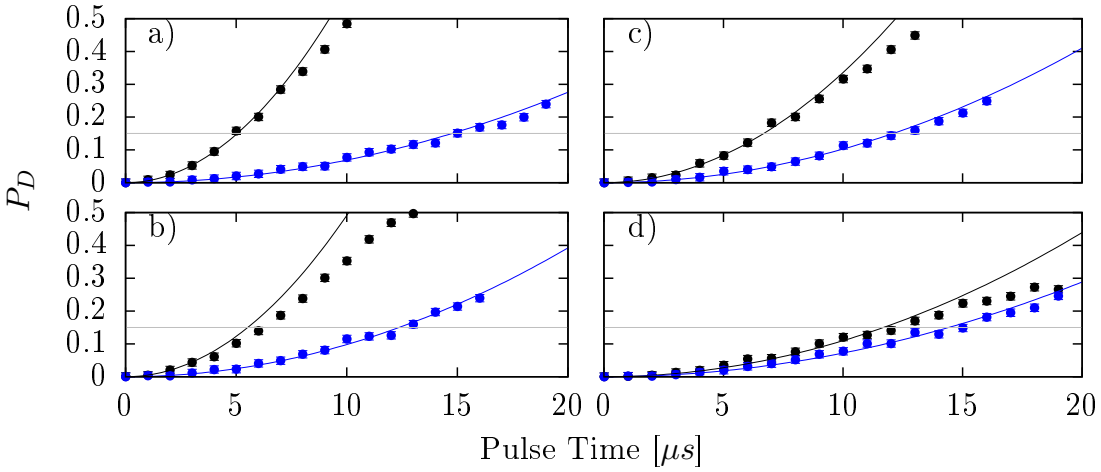

Figure 4.10.: Rising slope method: Beginning of Rabi oscillations for CAR and BSB for (a) a Doppler cooled ion with $\bar{n} = 30.7(9)$, with (b) additional 0.2 ms wait time and $\bar{n} = 59(2)$, (c) 0.4 ms wait time and $\bar{n} = 79(4)$ and (d) 0.7 ms wait time with $\bar{n} = 118(6)$. Only points below 0.15 are evaluated.

This method is well suited for heating rate measurements in micro ion traps. The short pulses with high repetition numbers ensure temperature measurements with high accuracy.

4.3.2. Phonon distribution Analysis

Like described in section 4.2.1 the Rabi oscillation dephasing is a consequence of different Rabi frequencies for the populated Fock states. This leads to the fact that the

information about the parameters describing the phonon distribution can be extracted of these Rabi oscillations. A fitting algorithm can match the full theoretical model to experimental data and extract the phonon distribution. This works for thermal and coherent distribution as well as for convolutions of these distributions. For a limited amount of phonon numbers this also works for arbitrary distributions. The technique uses the model of multiple motional transitions to increase the amount of obtained information. For low phonon number red and blue sidebands are a suitable choice. For large phonon numbers one chooses higher order sidebands. The actual measurement takes simultaneous pulse width scans of multiple transitions. A Bayesian fitting algorithm is used to obtain all parameters of the model function. The full evaluation of the matrix elements of equation 4.12 ensures that the evaluation is bound to the Lamb-Dicke limit. The model function for the RSB is given by

$$P_{RSB,i} = A + B\sum_n p_n e^{-\gamma t}(1+\cos(M_{n,n-1}\Omega t_i)) \tag{4.14}$$

$$\tag{4.15}$$

The discrete results for all measurement points i can be compared to the experiment outcome and used as input for the fitting algorithm. The combined fitting parameters are the measurement offset A, the contrast B, the bare Rabi frequency Ω, an empirical decay factor γ and the parameter of the phonon distribution. The offset and contrast parameters are required to compensate the limited detection and state preparation efficiency, while the decay facto covers additional decoherence effects.

For Doppler cooled ions the phonon distribution is thermal

$$p_n = \frac{\bar{n}^n}{(\bar{n}+1)^{n+1}}, \tag{4.16}$$

using the mean phonon number $\bar{n} := \sum_{n=0}^{\infty} n p_n$ as fitting parameter. For more complex problems the convolution of a thermal and a coherent distribution is used

$$p_n(\bar{n},\alpha) = \sum_{m=n}^{N} \frac{\bar{n}^m}{(\bar{n}+1)^{m+1}} \cdot e^{-|\alpha|^2} \frac{|\alpha|^{2(n-m)}}{(n-m)!}, \tag{4.17}$$

This distribution is shown with a constant thermal $\bar{n} = 0.08(1)$ in figure 4.11. The thermal part is determined from the ground state cooled situation and has to be taken into account for precise determination of the coherent excitation. All determined fit parameters with errors are also noted.

This technique enables precise values with realistic error estimations for a wide range of displacements. Parametrized phonon distributions can be modelled for different kinds of motional states. The measurement time is the only drawback of this technique. If required a less accurate but more efficient technique can be used, which is described in the next section can be performed.

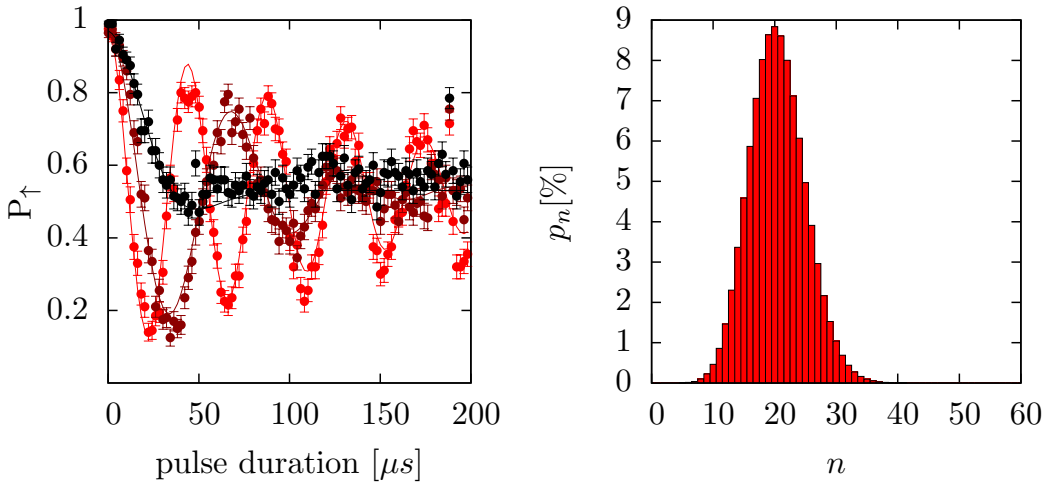

Figure 4.11.: Coherent state analysis: Simultaneous pulse width scan on CAR, RSB and second RSB with fit(left), and determinated coherent distribution (right) with displacement $\bar{n}_\alpha = 19.99(0.12)$, the Rabi frequency $\Omega = 252.9(3)\,\mathrm{kHz}$, decay parameter $\gamma = 4.5(2)\,\mathrm{kHz}$, contrast $B = 0.970(4)$ and offset $A = 0.091(6)$.

4.3.3. Optimized Energy Measurement (Pseudo Energy)

If the requirements on accuracy are less demanding and a defined phonon distribution can be assumed, an efficient energy measurement can be carried out by probing different $P_{\uparrow,m}$ transitions with fixed pulse areas. The individual pulse areas can be chosen to optimize the measurement sensitivity with a given energy range. An example for such an energy measurement is given by

$$E_\mathrm{p} = 2 \cdot (P_{\uparrow,+1}(3\pi) - P_{\uparrow,-1}(3\pi) - P_{\uparrow,-2}(2\pi)) + 7/2. \tag{4.18}$$

We term the quantity E_p *pseudo energy*, as its value is monotonically increasing for a coherent state in the medium excitation range ($\bar{n}_\alpha < 50$). This relation is shown in figure 4.12 including higher excitation ranges. Additional information can be used to include the overdetermined ranges in the evaluation. Using different measurement methods like the full phonon analysis described in section 4.3.2, one can identify the right phonon range and evaluate these sections as well. If the measurement is designed to generate a monotonic increasing excitation the turning points in the signal also denote the change of the pseudo energy ranges.

This method is fast and precise enough to evaluate the coherent excitation of certain transport operations. It enables determination of interesting measurement parameters for more precise techniques.

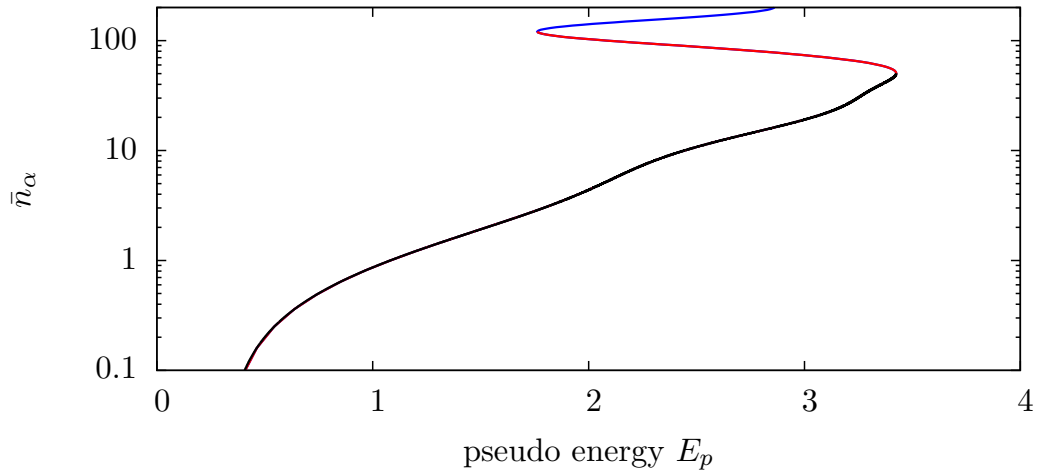

Figure 4.12.: Pseudo Energy: The relation between pseudo energy and $\bar{n}_\alpha$ is displayed for the specific choice of pulse areas in equation 4.18. The overdetermined values can be used if the measurement uses monotonic increasing excitation or the range is verified by a different measurement methods.

5

Coherence Measurement and Testinig of Decoherence Processes

The motional coherence of the ion in the trap is relevant for most future quantum devices, where the motion is used as interaction bus between several ions. A ground state cooled ion with $\bar{n} = 0$ is prone to heating from ambient electric fields. Random momentum kicks to the ion cause a rising mean phonon number $\bar{n}$. In section 5.1 the linear change of the temperature versus time, the *heating rage* is measured and described. A closer look on the dependence on the trap surface temperature is performed in section 5.2.

The decoherence of the internal electronic state is measured by creating a superposition state and monitoring its phase coherence. The timescale on which the superposition phase remains well defined is dependent on the external magnetic field fluctuations and the laser coherence. These measurements are described in section 5.3.

5.1. Motional Heating Rate

The heating rate is obtained by performing several temperature measurements at different heating times [TKK$^+$00]. Hereby, the ion is left in the dark, without laser interaction. During this time the heating rate of the ion trap acts on the ion. Afterwards a temperature measurement like a full phonon analysis described in section 4.3.2 or a rising slope method (section 4.3.1) is performed to determine the mean phonon number. Each measurement has to be performed with multiple heating times to determine the

line of best fit. Like shown in figure 5.2 the linear relation between mean phonon number $\bar{n}$ and time t is consistent with a constant heating rate $\dot{n}$. In this figure, six different heating rate measurement results are shown taken at different cryostat temperatures.

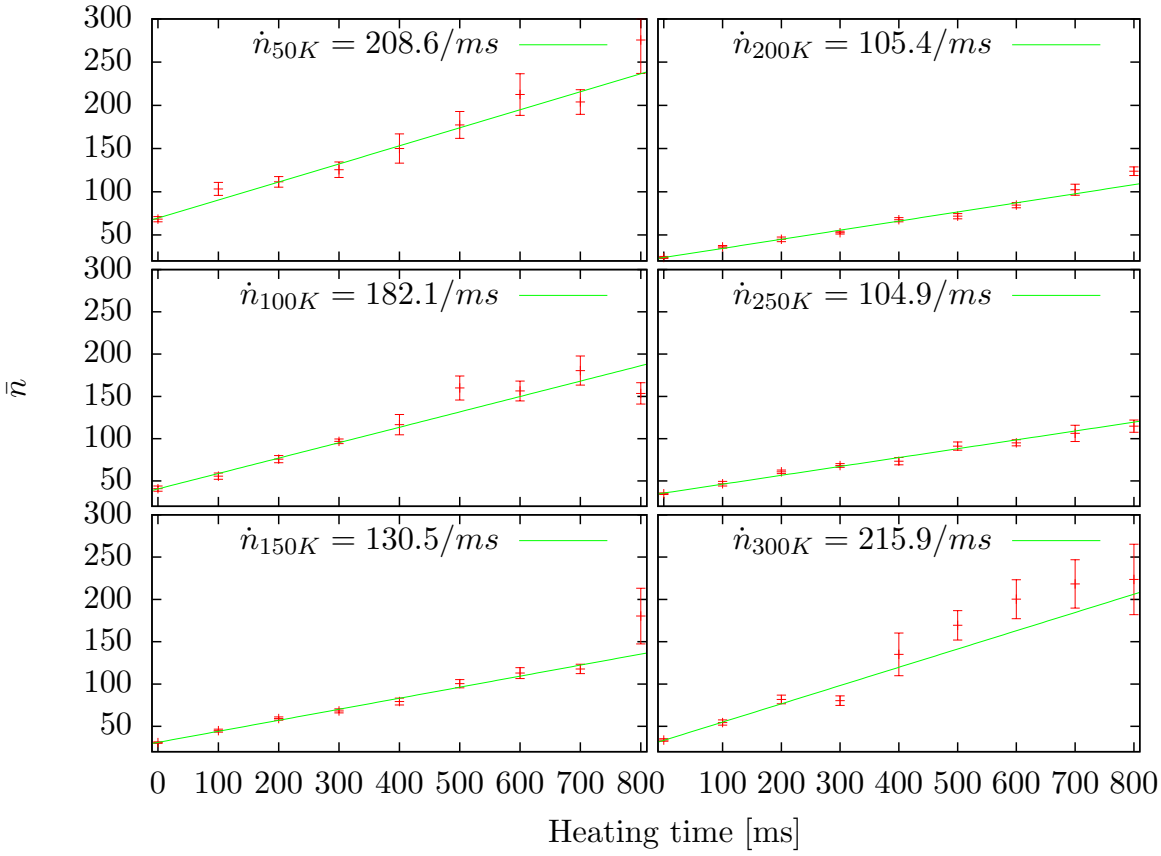

Figure 5.1.: Heating rate measurements: These six heating reate measuremnts (points) have been performed at different cryostat temperatures using the rising slope method. The error bars are obtained by the rising slope method, described in section 4.3.1.

The electrical noise, causing this heating strongly depends on the used DC voltage supply. Without low pass filtering of the DC signals no coherent Rabi oscillations can be observed, because of the high heating rate. This lowest order heating is caused by varying voltages on the DC electrodes causing random electric field kicks disturbing the ions motion. This effect is dependent on the ion-surface distance and results in higher heating rates for smaller ion traps.

Even if all voltage noise on the DC electrodes is suppressed one observes a linear heating of the ion. This anomalous motional heating is generated by microscopic noisy poten-

tials. These fluctuating patch charges are a current goal of research and discussed in the next section.

5.2. Heating Rate Dependency from Trap Surface Temperature

On the cryogenic setup, the dependence of the heating rate on the electrode surface temperature can be analysed. Several experiments of the group from Chuang at quanta[1] have shown that the heating rate strongly depends on the ion trap surface temperature. Their work at the lower temperature range from 7 K to 100 K was analysed and they found a suppression of the heating rate by two orders of magnitude for a temperature of 46 K in a planar ion trap [LGA+08, LGL+08]. In a RF needle trap a suppression by one order of magnitude was shown by cooling to 150 K [DOS+06].

For easy comparison to other results the heating rate is converted to the electric field noise [LGA+08] using

$$S_E(\dot{n}, \omega_z) = \frac{4m\hbar\omega_z}{e^2}\dot{n}, \tag{5.1}$$

where m is the ion mass and ω_z the motional frequency. This quantity implies a linear dependence of the heating rate from the motional frequency ($\dot{n} \propto 1/\omega$) which has been proven for this experiment [Sch09]. As shown in figure 5.2 the actual results are not fully conclusive. Within the measured range no strong dependence from the trap surface temperature was observed. Most measurement points where taken interleaved within one cool down and warm up cycle. After each temperature change a 6 hours thermalisation time ensured equilibrium temperature of the cryostat and the ion trap.

Due to the large temperature range several parameters change physically. At first the thermal contraction of the cryostat and the trap holder leads to spatcial displacement of the whole ion trap and the ion itself. This requires a realignment of all lasers and the imaging optics after each temperature change. The arising error from possible misalignments are excluded by an appropriate measurement technique described in section 4.3.1. The impedance matching of the helical resonator changed slightly during cool down. This could be compensated for a large range with adjusting the drive power. At low temperatures a new incoupling was necessary to achieve suitable RF drive amplitudes. This might occur due to varying parasitic capacitances from thermal contraction of the wiring and the trap itself. Furthermore the used micro ion trap was visibly contaminated with unknown material. The gold coating of this used model was incomplete at the end of the DC and RF finger structure. The visible material might be the confinement layer of titanium which is supposed to be between the alumina and the gold layer. If the titanium is not completely covered by gold it would oxidise and

[1] Center for Ultracold Atoms, MIT Research Laboratory of Electronics, Boston, USA

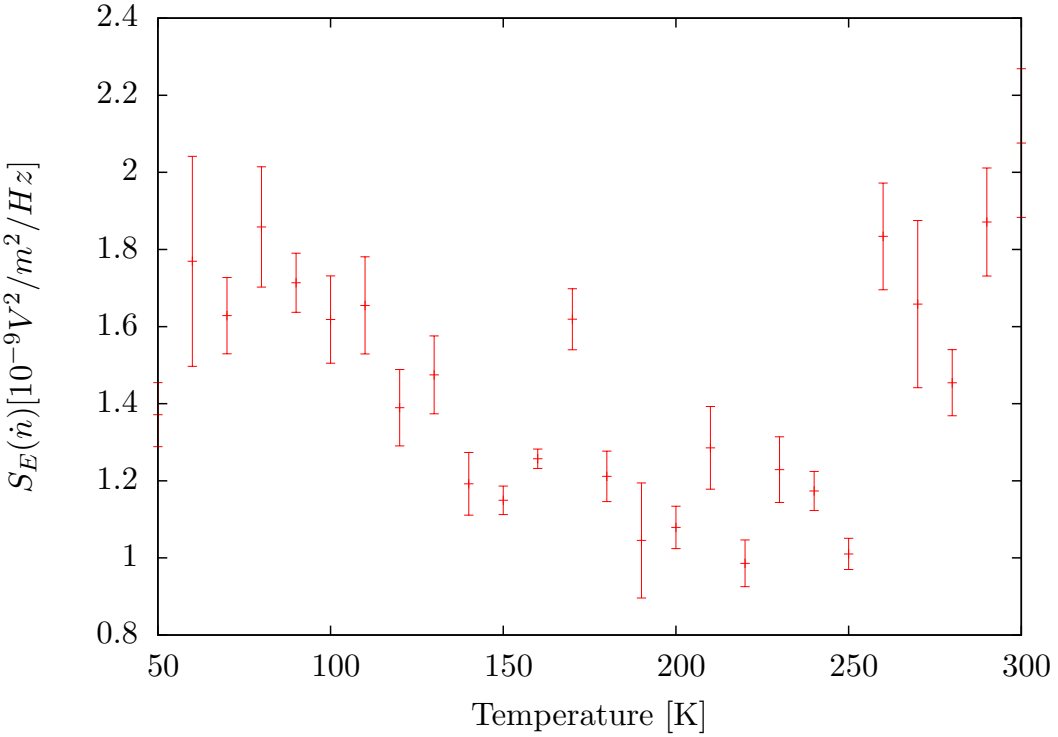

Figure 5.2.: Electrical field noise density temperature dependence: The results of about 200 temperature measurements. Within the temperature range from room temperature (293 K) to 50 K no clear trend can be recognized.

also bind several other atoms or molecules. This might have an unpredictable effect on the heating rate of the ion.

Recent experiments showed that surface contamination takes part in heating effect. In [HCW+12] an Argon ion beam was used to clean the electrode surface of a planar trap, which reduced the motional heating rate by two orders of magnitude. This first experiment detected a 2-3 monolayers of oxygen-free carbon on the Auger trap electrodes, which is removed by the cleaning process.

Due to the contamination of the electrode surfaces, this measurement series is a comparison basis for future experiments. This time consuming measurement has to be performed using different kinds of ion traps and different surface structures to identify the individual effects. Furthermore the minimum detected electric field noise value of $0.98(2) \times 10^{-9}\,\mathrm{V}^2/\mathrm{m}^2/\mathrm{Hz}$ is four orders of magnitude higher than the values from [LGA+08, LGL+08]. The heating rate measurment in this ion trap could be dominated by non temperature dependent sources. Though this is the first temperature dependent heating rate measurement in a 3D trap it relies on further measurements to be inter-

preted. Especially results in the narrow region of the trap might be interesting because of the much higher expected heating rate.

5.3. Ramsey Experiments

The internal coherence of the laser-ion interaction can be determined using a Ramsey measurement scheme. It compares the coherence length of the laser with the phase coherence of a superposition state. This method was first described in [Ram86] for molecular beams. The general approach is universal and it has lead to many variations in the field of atom physics. A Ramsey type measurement uses the possibility to map the phase information on the internal state.

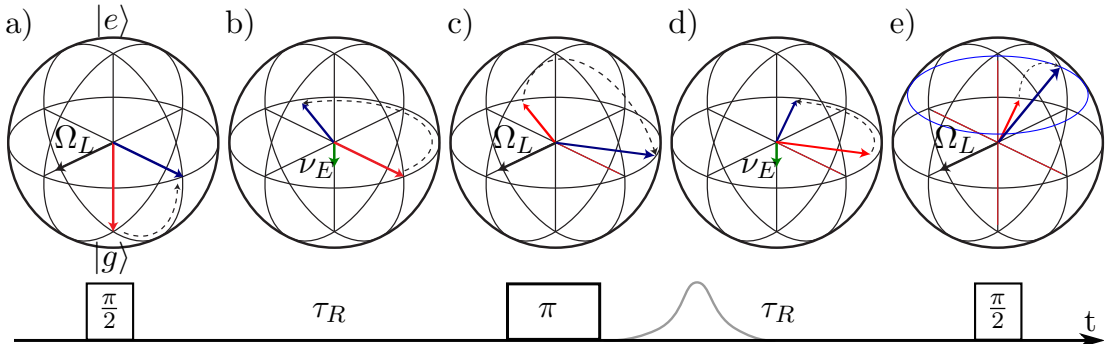

Figure 5.3.: Ramsey measurement sequence: a) the first $\pi/2$ pulse sets the phase reference between laser and ion. It creates a balanced superposition state driven with the laser Rabi frequency Ω_L. During the free evolution b) the phase rotates with the frequency ν_E corresponding to the energy splitting. The spin echo π pulse leads to a phase flip. Please note the unchanged Rabi frequency vector denoting the rotation axis. d) during the second Ramsey time τ_R optional effects like transport operations can act on the phase before at e) the phase state is mapped to the internal state by applying the $\pi/2$ analysis pulse.

This is realised with a pulse sequence which consists of a $\pi/2$ pulse, a free propagation time and a second $\pi/2$ pulse. The first pulse creates a balanced superposition state. On the same hand it sets a phase reference for the superposition state. This phase now starts to rotate with the transition frequency during the *Ramsey time* τ_R. The second $\pi/2$ analysis pulse maps back the phase information into the internal state, which can be measured. The sequence described in figure 5.3 contains one additional π pulse which performs a *spin echo*. It inverts the accumulated phase and removes phase dispersion at slow timescales.

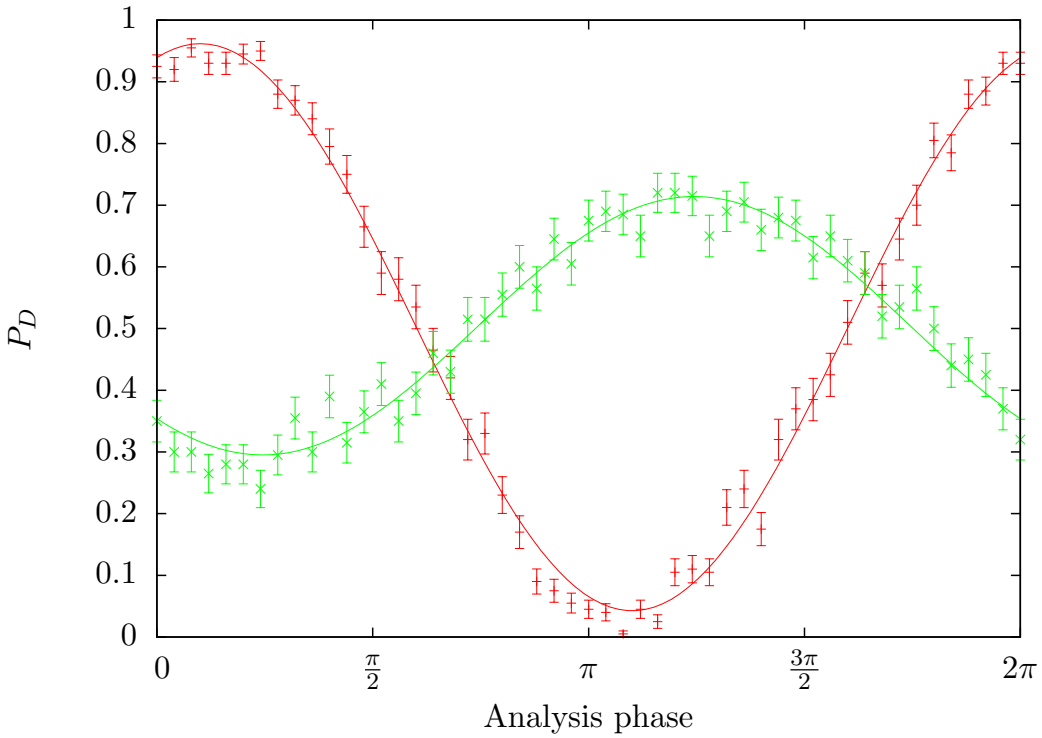

Figure 5.4.: Ramsey analysis of $S_{1/2}$ $m_j = 1/2 \rightarrow D_{5/2}$ $m_j = +5/2$ transition: The fitted sin function shows the metastable state population P_D versus the phase of the analysis pulse for a Ramey time of 50 μs with a contrast of 0.91(1) and for 300 with 0.41(1).

The relative phase information acquired during the Ramsey time can be evaluated using the contrast of the resulting fringe signal when the phase of the analysis pulse is scanned. Figure 5.4 shows the result for two different Ramsey times. The changing phase of the fitted sine function corresponds to a constant offset phase for all measurement points and can be neglected in the coherence analysis. The total achievable contrast is limited by phase fluctuations, which average out and reduce the amplitude. This contrast is a measurement of the internal coherence of the ion and the coherence length of the laser. This contrast can now be analyzed for different Ramsey times. Figure 5.5 shows an analysis during some setup improvement steps. The internal coherence depends on the stability of the transition levels of the atom and the laser coherence. The atom is mainly changed due to magnetic field fluctuations which can be seen during the setup improvement. A simple shielding for the current supply lines of the magnetic field coils lead to in improvement of 28 % and the partially attachment of magnetic shielding foil a total improvement of 58 %.

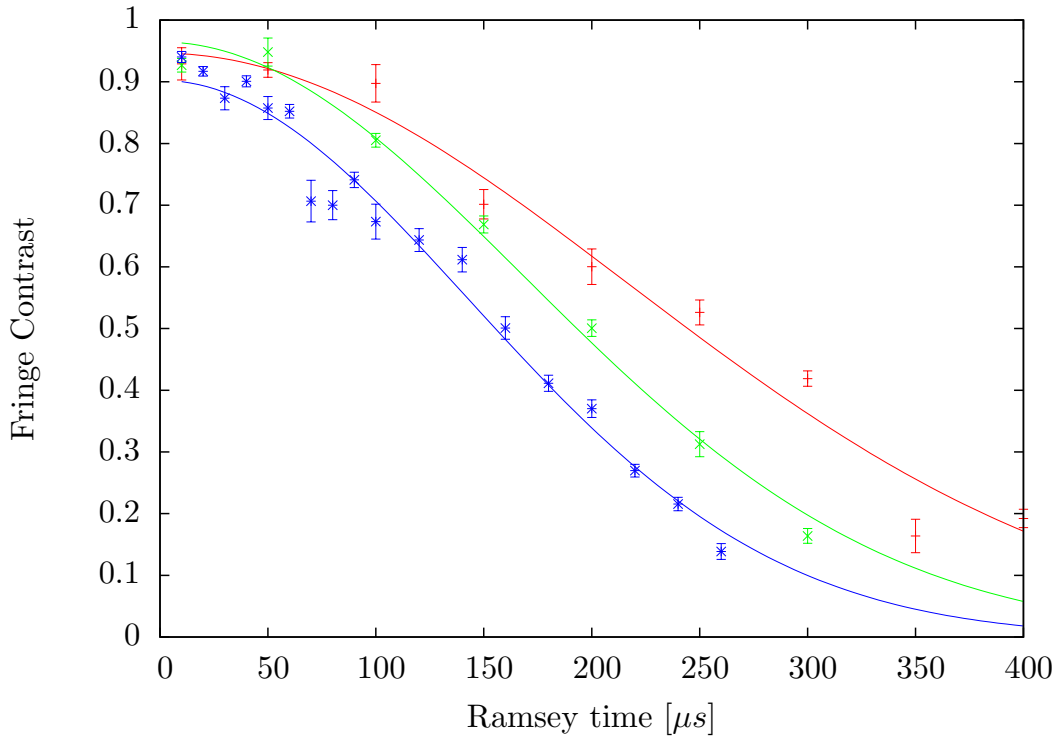

Figure 5.5.: Ramsey contrast improvement: The initial setup Ramsey contrast in blue, the first improvement using shielded coil current connections in green and the additional attachment of μ-metal shielding foil in red. To all measurement points individual Gaussian functions are fitted.

This shows that the main source for internal state decoherence are magnetic field fluctuations. If longer internal state coherence is necessary one has to improve the magnetic shielding and the current supply for the field coils. The laser coherence could not be quantified because no second laser source was available.

5.4. Fock State Thermalisation

If one takes a closer look at the coherence of specific nonclassical states one has to perform a more general phonon analysis. To obtain more information of arbitrary phonon states no probability distribution is assumed. The phonon numbers are analysed using the same technique as described in section 4.3.2, but with a free fit parameter for each phonon probability p_n. This technique is limited to the lowest ten Fock states using the pulse width scans of the blue and red motional sideband as input information.

A maximum likelihood fit algorithm provides normalised probabilities including error estimation for each phonon number.

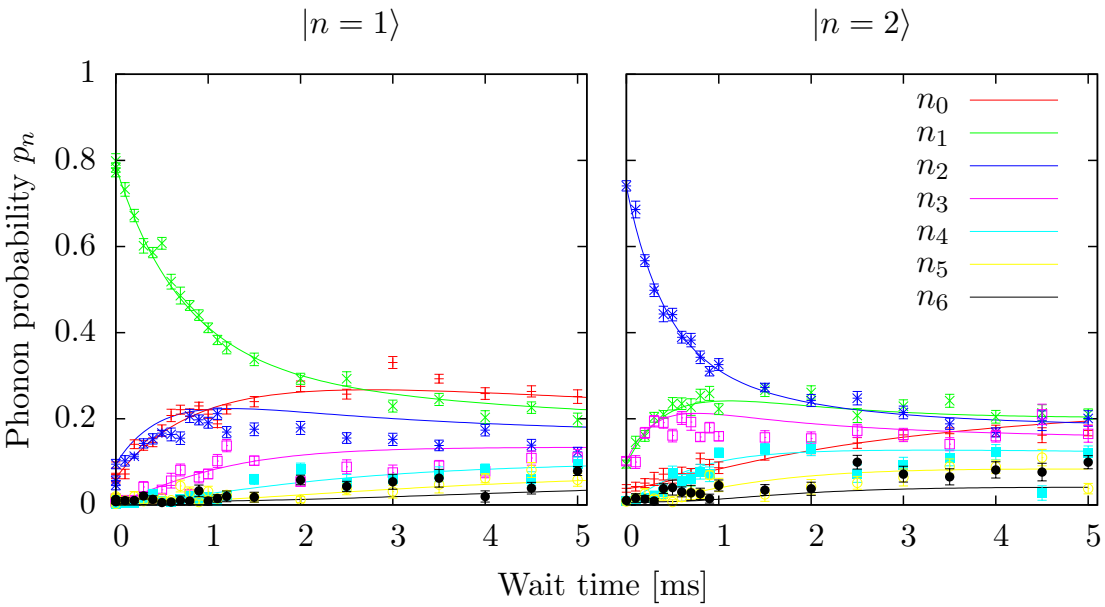

Figure 5.6.: Fock state thermalisation: The measurements points correspond to individual phonon probabilities which are modelld using rate equation as solid lines.

This technique enables detection and coherence studies of a Fock state $|n\rangle$. These states are generated from a ground state cooled ion with additional optical excitation pulses. The Fock state $|n=1\rangle$ is produced by applying one π pulse on the BSB and one π pulse on the carrier to gain 1 phonon and end up in the same spin state. This can be performed with sufficient fidelity for low phonon numbers, as you see in figure 5.6. The thermalisation of these Fock states is on the time scale of the heating rate. A simple rate model is used to describe the transitions between different Fock states.

$$\dot{p}_n = R_{n-1,n} \cdot p_{n-1} + R_{n+1,n} \cdot p_{n+1} - (R_{n,n-1} + R_{n,n+1}) p_n, \tag{5.2}$$

where we introduce the transition rates $R_{n,m}$ from phonon number n to m. If we consider the steady state $\dot{p}_n = 0$ as Boltzmann distribution and find

$$\frac{p_{n-1}}{p_n} = e^{\frac{\hbar\omega}{k_B T}} \approx 1 \tag{5.3}$$

For temperatures above 4 K and axial frequencies of 1 MHz. If we take a look at all rate terms for increasing phonon number we find

$$R_{n-1,n}p_{n-1} = R_{n,n+1}p_n \Rightarrow \frac{p_{n-1}}{p_n} = \frac{R_{n,n+1}}{R_{n+1,n}} = 1 \tag{5.4}$$

$$R_{n-1,n} = R_{n,n+1} = R_+(n) \tag{5.5}$$

The same solution for the negative rate $R_-(n)$ fulfilling the steady state of equation 5.2 and leads to the simplified form

$$p'_n = R_+(n) \cdot p_{n-1} + R_-(n) \cdot p_{n+1} - (R_-(n) + R_+(n))p_n \tag{5.6}$$

The data in figure 5.7 was fitted using a transition rate $R_+(n) = R_-(n) = 300\,\text{Hz}\cdot(1 + \sqrt{n})$.

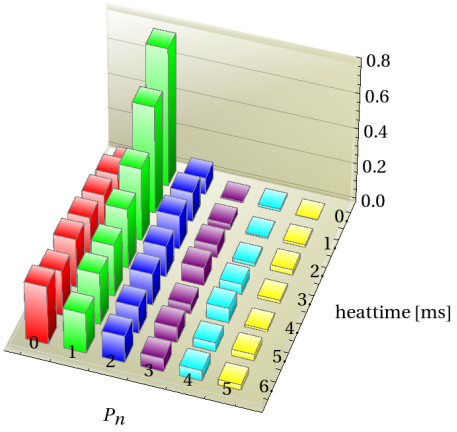

Figure 5.7.: Fock state thermalisation: The prepared Fock state $\langle\Psi_1|n=1\rangle = 0.8$ yields to a thermal distribution with $\bar{n} = 2$ after a thermalisation time of 6 ms.

The same data is shown in figure 5.7 to demonstrate the transition from Fock to a thermal state. The initial state $|\Psi_1\rangle$ is prepared with a fidelity of $\langle\Psi_1|n=1\rangle = 0.8$. It is spread to a thermal state with the mean phonon number $\bar{n} = 2$. Note that the probability for the $|n=0\rangle$ excitation increases more strongly than the probability of $|n=2\rangle$.

6

Transport Operations in Segmented Ion Traps for Sensing Electric and Magnetic Fields

Transport operations are a key component for the operation of segmented ion traps for quantum computation. The execution of quantum algorithms on segmented ion traps will require a high number of transport operations [Ste97]. The ions are shuttled around, merged in larger crystals or separated in individual potentials. These transport operations must be much faster than the coherence time, and further one aims at executing these operations to be as fast as possible to render the quantum computer efficient.

But also in the slow transport regime (ms and adiabatic) the ion is a useful tool to probe physical quantities. The first applications for transport based ion operations are demonstrated in section 6.1.1, where the ion is used as electrical field probe through the ion trap also published in [HZP+10]. In section 6.1.2 it is demonstrated how a single ion can be utilized as precision probe for magnetic field gradients, published in [WPZ+11]. The ions position within the RF field is used to measure multi dimensional stray field components in section 6.1.3, published in [NDM+11].

To perform fast transport operations one requires a voltage source which applies arbitrary voltage ramps to multiple DC segments sinmultaneously. This is done with the multi channel arbitrary function generator from section 2.4. It is calibrated by performing coherent excitations of the ion wavepacket, described in section 6.2. This technique can be used to generate displaced fock states, described in section 6.2.3.

As already mentioned the relevant timescale for ion transport operations is the axial motional frequency ω_z. The axial harmonic oscillator is manipulated and the ions equation of motion change to

$$\ddot{z} = -\frac{e}{m}E_z(t) = -\omega^2(z(t) - z_0(t)) \tag{6.1}$$

where the varying voltages generate a time dependent axial electric field $E_z(t) = \frac{\partial \Phi}{\partial z}$ while conserving the motional frequency ω_z. The time dependent equilibrium position of the axial potential $z_0(t)$ is chosen by the voltage variation described in section 3.7. The ions Trajectory in the moved electric force is dependent from the time scale of the movement operation $z(t)$, with $t \in [0..T]$. For adiabatic transports $T \gg 2\pi/\omega_z$ the ion stays close to the potential minimum z_0. A ground state cooled ion would be accelerated by the potential without increasing the mean phonon number. Because this technique is slow compared to the measured heating rate is is only used for measurements which do not require motional coherence described in section 6.1.

For non-adiabatic transport operations on the timescale $T \approx 2\pi/\omega_z$ the ion is displaced in the transport potential. The potential movements are on the timescale of the harmonic oscillator and cause high motional excitation during the transport operation. This gives rise to novel analysation methos described in section 6.3 where ground state ion transport operations are realised with minimum energy gain.

6.1. Adiabatic Transport Operations

For several kinds of experiments slow, adiabatic transport operations are sufficient. The requirements for the transport operation depend on the kind of information which has to be preserved. If no motional state preservation is necessary the transport is very robust in a wide range. The transport must be faster than the lifetime of the transported state. For information in the metastable $D_{5/2}$ state for example, transport operations of more than 100 ms are possible to realize remote spectroscopy as described in the next section.

6.1.1. Remote Electric Field Sensing

A trapped Ca ion can classically be treated as charged point particle. Especially if one compares it to conventional voltage measurement probes, its size and mass is negligible. Due to its charge to mass ratio the ions back action on the trapping potential is neglected. The ion is utilized to measure the electric curvature, created by the DC trap electrodes.

If the trapping potential is shifted the potential curvature at the minimum, i.e. the trap frequency, changes. Position changes can be observed using imaging optics resolving

1 μm displacement which corresponds to applying 50 mV to a neighbouring segment. This method would require a continuous observation of the ion. For a remote measurement scheme one observes the axial frequency while moving through the trap. The variation of the axial frequency around $\omega_z = 2\pi 1.3$ MHz can be determined with a 1 kHz resolution, which corresponds to applying a voltage of 26 mV to a neighbouring segment.

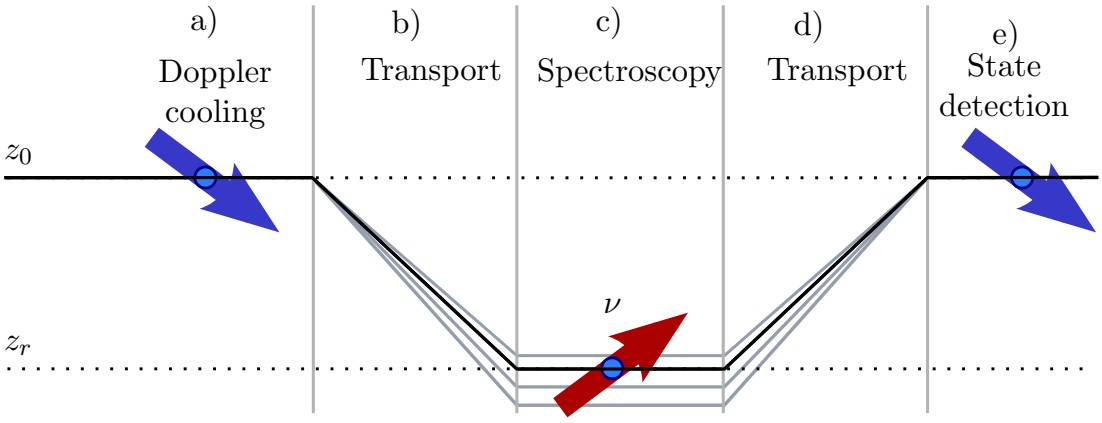

Figure 6.1.: Remote spectroscopy scheme: The ion is initially Doppler cooled a) at the trap site z_0. After the first transport b) to the remote location z_r the spectroscopy pulse is applied c). The same transport ramp is now reversed d) to bring the ion back in the camera field of view and perform the state measurement e).

The remote spectroscopy measurement scheme is described in figure 6.1. One measurement operation consists of five steps:

a) The ion is initialized applying a voltage configuration $V_0(s)$ to all trap segments, which locates the ion at trapping site z_0. Here the ion is Doppler cooled and optically pumped to the $S_{1/2}, m_j = +1/2$ state.

b) Afterwards the ion is shuttled to the remote location z_r where the spectroscopy laser at 729 nm is aligned using a simmilar scheme.

c) The ion is exposed to a spectroscopy pulse at remote location z_r with the laser frequency ν close to the BSB transition.

d) The ion is shuttled back to the observation site

e) After a settling time the ion is locates at the initial position z_0 where the imaging optics are aligned. The following state detection determines the $D_{5/2}$ excitation.

These five steps are repeated typically 100 times with fixed laser frequency ν, which generates one measurement point in a spectrum. The whole spectrum is obtained by repeating this measurement for varying laser frequencies.

The transport ramps are determined using the SVD and Thikonov regularisation algorithm described in section 3.2. The created voltage ramps realize an almost constant axial frequency along the trap axis with periodic deviations of 14%. These oscillations are generated by adjusting the optimisation parameters with focus on smooth voltage change. Using this method the data from figure 6.2 was obtained. For each measure-

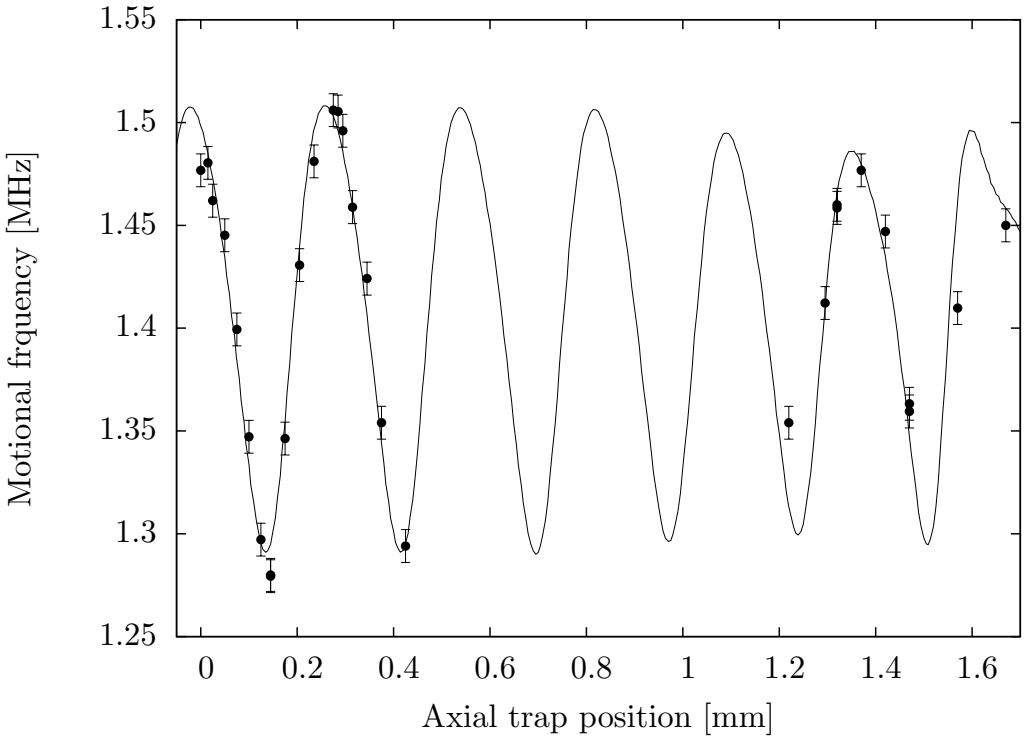

Figure 6.2.: Remote electric field probe: The ion was positioned over a range of 1.6 mm in the ion trap. The measured motional frequency is shown as points while the simulated frequency is shown as solid line. The mean deviation of all points is 0.73 %

ment an additional adjustment sequence has to be carried out. The ion is constantly moved to the new remote location z_r and excited on the CAR transition. The spacial position of the laser at 729 nm was adjusted to maximize the Rabi frequency. The final measurement consists of sideband spectroscopy like described in section 4.2.2 of the BSB transition. The distance from carrier to the motional sideband transition defines the motional frequency.

This measurement technique allows the verification of simulation models with high accuracy. The whole tool chain of numerical potential simulation, voltage determination algorithm and voltage supply is analysed. Furthermore the fabrication precision of the

trap is proven to be consistent with the model from whicht the electrostatic properties are determined.

6.1.2. Remote Magnetic Field Probe

The same scheme for remote measurement could also be used to measure the magnetic field. The Zeemann shift of the different magnetic levels m_j splits proportionally to the magnetic field

$$\Delta_{Zeeman} = (m_{j,+5/2} g_D - m_{j,+1/2} g_S)\mu_B |\vec{B}| \approx 2.89 \frac{\text{MHz}}{\text{Gauss}} \tag{6.2}$$

using the Bohr magneton μ_B and the Landé factors g_j of the driven transition. The major drawback of this method is that each remote location requires a realignment of the spectroscopy laser.

One can also think of a more advanced measurement scheme, which is based on the Ramsey method described in section 5.3. The phase of a superposition state is precisely measurable and all laser operations can be performed at the same location [WPZ+11].

The ion is prepared a superposition state of two Zeeman sublevels of the ground state $S_{1/2}$. Within the first Ramsey time a transport operation towards the neighbouring DC segment is performed. During this trajectory the ion would change its Zeeman splitting according to magnetic field change and acquire an additional phase. After this Ramsey time, a spin echo is performed using a π pulse, affecting a phase flip of 180° and leading to a elimination of slow magnetic field drifts. After a second Ramsey time without transport the phase information is mapped in the spin state using the second $\pi/2$ pulse. The final state readout determines the acquired phase. The accumulated phase change is given by the integral over the ions position

$$\Phi_{rad} = \frac{g_j \mu_B}{\hbar} \frac{\delta B_z}{\delta z} \int_0^T [z_{ion}(t) - z_{ion}(0)] dt, \tag{6.3}$$

using the Landé factor $g_j = 2$ for the $S_{1/2}$ state and the Bohr magneton μ_B. The variables are the magnetic field gradient $\frac{\delta B_z}{\delta z}$ along the axial trajectory $z(t)$. The magnetic field is generated by external field coils. By operating the two coils at different currents, the magnetic field gradient along the trap axis can be modified. The coils must always give rise to an offset magnetic field of about 7 Gauss to perform normal ion trap operation. In figure 6.3 measurement results for equal currents, a maximised and a minimized field gradient are shown. The phase shift is plotted versus the displacement-time inegral from equation 6.3. By varying the transport distance the constant gradient can be measured with a precision of $\Delta B/B \sim 5 \cdot 10^{-7}$.

This technique uses state superpositions for high precision measurement of magnetic field gradients. It allows high resolution spatial and magnitude wise measurement of the

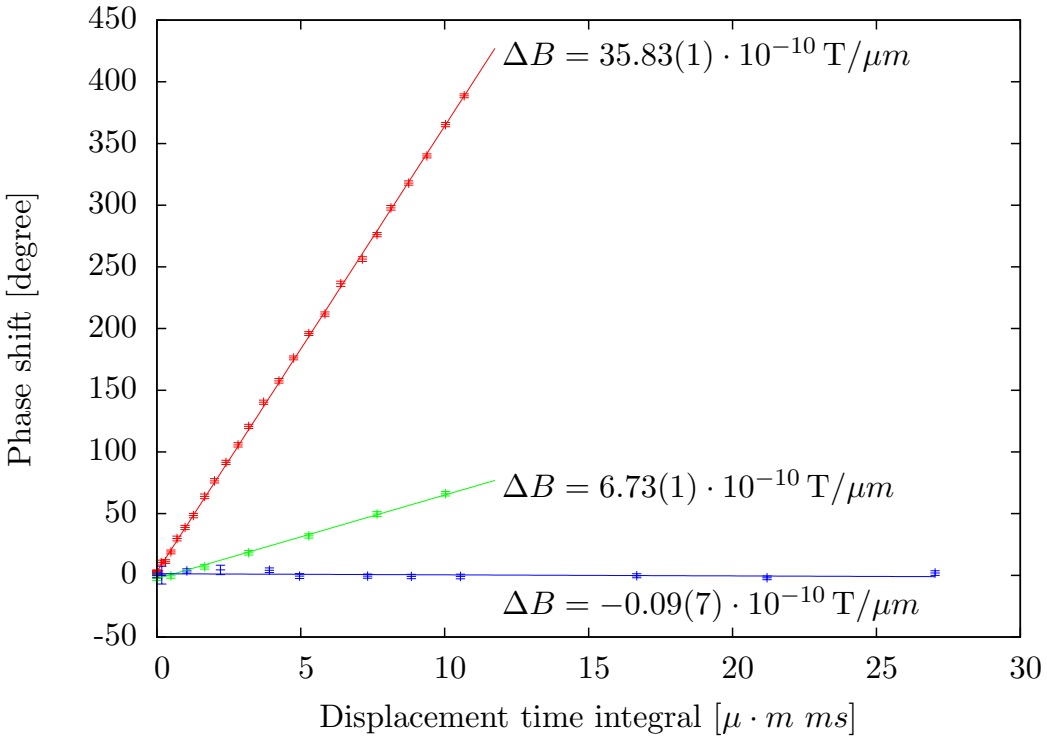

Figure 6.3.: Magnetic field gradient measurement: Three different measurements have been performed. The maximized gradient uses 1 A at coil 1 and 3 A at coil 2. This lead to a 3.58 mT/m gradient. The balanced gradient is measured with equal coil current of 1.9 A occurs from imperfect coil alignment and different magnetic materials in the setup. The minimized gradient is generated using 1.66 A at coil 1 and 2.122 A at coil 2.

field gradient in various distances. It can be performed to optimize operation parameters for more advanced measurements, shown in section 6.3.3.

6.1.3. Micro Motion Analysis in a Planar Trap

A different way of utilising a single ion as transported electric field probe has been published in collaboration with the ion trap group of H. Häffner[1] [NDM+11]. It is based on resonant motional excitation and used to determine the electric stray fields at various positions along a planar trap.

As foundation for this measurement the planar trap was numerically simulated as described in section 3.6.2. The ion positions above the trap geometry was obtained by

[1]Department of Physics, University of California, USA

a pseudo potential analysis and DC voltage ramps have been determined to realise a deterministic axial ion transport. That data was verified by ion observations with using a EMCCD camera and used to position the ion field probe in the trap.

The measurement scheme bases on a precise determination of the node of the RF drive field with drive frequency $\Omega_{RF} = 2\pi \cdot 15\,\mathrm{MHz}$. The pseudo potential minimum forms a continuous path above the surface of the ion trap, shown in figure 3.8. Applying compensation fields in all directions, pushing the ion into the node, corresponds to a measurement of the electric stray field at the position of the ion. In order to separate the spatial dimensions for the node distance measurement, resonant excitation of the motional oscillation mode is used. The transport potentials are determined to keep them constant along the axis as described in section 3.6.1. The two radial modes and the axial mode are chosen to be well separated in frequency: $(\omega_x, \omega_y, \omega_z) \approx 2\pi(1.2, 1.4, 0.4)\,\mathrm{MHz}$. The motional excitation is generated by the RF electrode by mixing the initial drive frequency with $\Omega_{RF} + \omega_{ex}$. The generated field by the RF electrode geometry contains the excitation frequency ω_{ex} as beat signal. This beat signal can resonantly excite ion motion on mode i if $\omega_{ex} = \omega_i$. As the excitation field is created by the same electrode geometry as the RF drive field their nodes coincide.

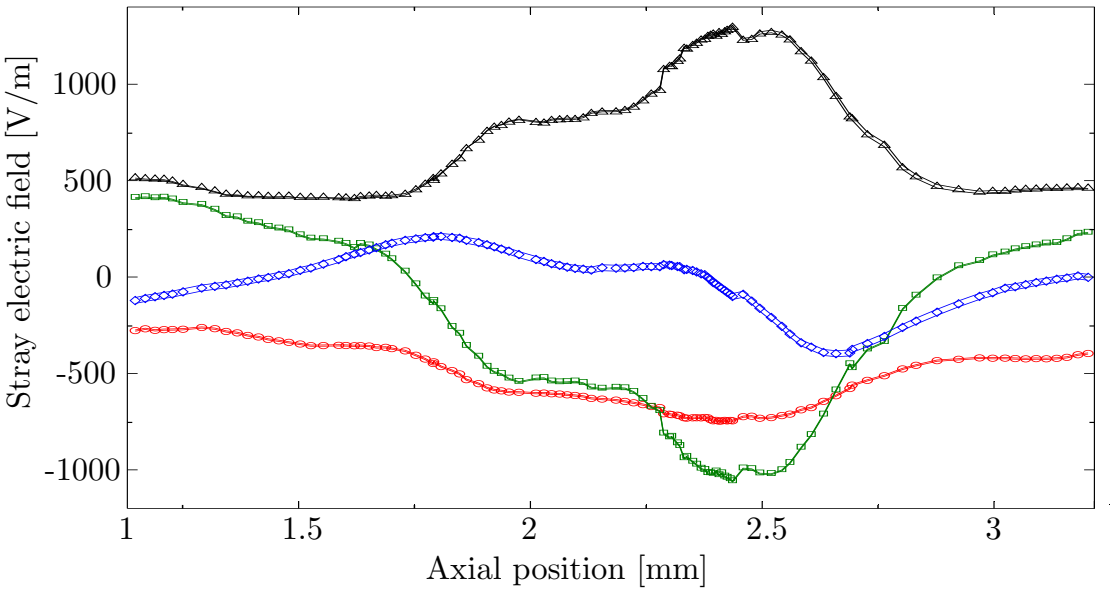

Figure 6.4.: Electric stray fields in planar trap: Sequential measurements of the electric stray field (black) $|\vec{E}| = |(E_x, E_y, E_z)|$ along the trap axis.

Carried out for both radial modes, the ion can be moved towards the excitation minimum using external compensation voltages. The radial stray field component can be calculated from the applied compensation voltage. The axial potition deviation from the simulated position is corrected by additional axial fields which leads to the axial

stray field component. This measurement is shown in figure 6.4 along the trap axis. The separation of the motional modes gives rise to a 3D stray field determination along the trap axis.

This technique requires the excitation frequencies lie within in the bandwidth of the RF amplifier and helical resonator. If required the modulation amplitude can be varied to increase the drive strength. This method also provides a precise tool to observe local charging effects of the trap surface.

6.2. Electronic Motional Excitation and Generation of Displaced Number States

There are several methods to excite motion in ion traps. Several experiments utilized coherent excitation using light forces [LKS+05, PWSSK10] as part of quantum protocols like the generation of entangled states. Optical beatnotes are used to resonantly drive the ion and excite a coherent state. This technique can be applied with precise amount of excitation and a spin dependent coupling. The limitation arises from the continuous excitation using the short wavelength of the optical field. The ions rising motional amplitude leads to a decreasing excitation force, which sets a limit to the total amount of excitation.

The displacement parameter α is used to describe the coherent state

$$|\alpha\rangle = D(\alpha)\,|0\rangle = e^{-|\alpha|^2/2} \sum_{n=0}^{\infty} \frac{\alpha^n}{\sqrt{n!}}\,|n\rangle \tag{6.4}$$

where the displacement operator $D(\alpha) = exp(\alpha a^\dagger - \alpha^* a)$ displaces the vacuum state $|0\rangle$ in phase space by the complex amplitude α. For this displaced state the phonon probability is given by the distribution

$$p_n = e^{-|\alpha|^2} \frac{|\alpha|^{2n}}{n!}. \tag{6.5}$$

This Poissonian distribution has the mean phonon number $\bar{n}_\alpha = |\alpha|^2$. For low excitations $\alpha \to 0$ the coherent distribution and the thermal distribution become experimentally indistinguishable.

For generating coherent states by means of electric excitation the axial DC voltages are manipulated to result in a shifted axial potential like shown in figure 6.5. The initial step is the preparation of a ground state cooled ion. Then an axial voltage step is applied which causes a displaced DC potential. This displacement must be faster compared to the ion oscillation period $\tau_z = 2\pi/\omega_z \approx 730\,\text{ns}$ in the displaced potential. The groundstate wavefunction forms now a coherent state according to the overlap with

the higher energy levels in the displaced potential. The ion propagates in the displaced potential during the applied pulse time τ_α. If the pulse is matched to be $\tau_\alpha = \tau_z/2$ the coherent states position probability moves the most from the initial position. Now the fast voltage change back leads to a high coherent excitation.

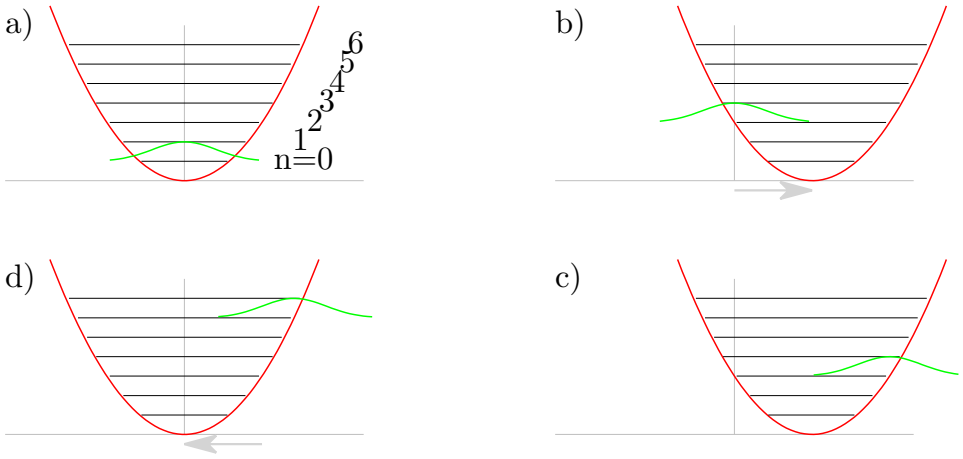

Figure 6.5.: Coherent excitation scheme: (a) ground state cooled ion at the initial trapping site. (b) displaced potential forms a coherent state which is (c) propagated in the displaced potential. (d) the recovering of the initial potential increases the coherent excitation.

In [PWSSK10] a maximum excitation of $\alpha = 2.$ was generated using light forces. The next sections demonstrates the generation of coherent states using voltage steps, generating a displaced quantum state.

6.2.1. Asymetric Excitation

The axial trapping potential generated by DC segment 5 is displaced by a short voltage pulse at one neighbouring segment. The multiple arbitrary function generator described in section 2.4 can perform high voltage resolution pulse with a length of 400 ns. This pulse leaves the ion in some motionally excited state which is analysed using the energy measurement techniques described in section 4.3.2. The excitation of a ground state cooled ion is found to match a coherent phonon distribution for a wide range of kick parameters.

In figure 6.6 the individual excitation behaviours for the two neighbouring segments with both polarities are shown. The differing excitation slope of segment 4 and 6 shows that the ions initial equilibrium position is not in the centre of segment 5. The

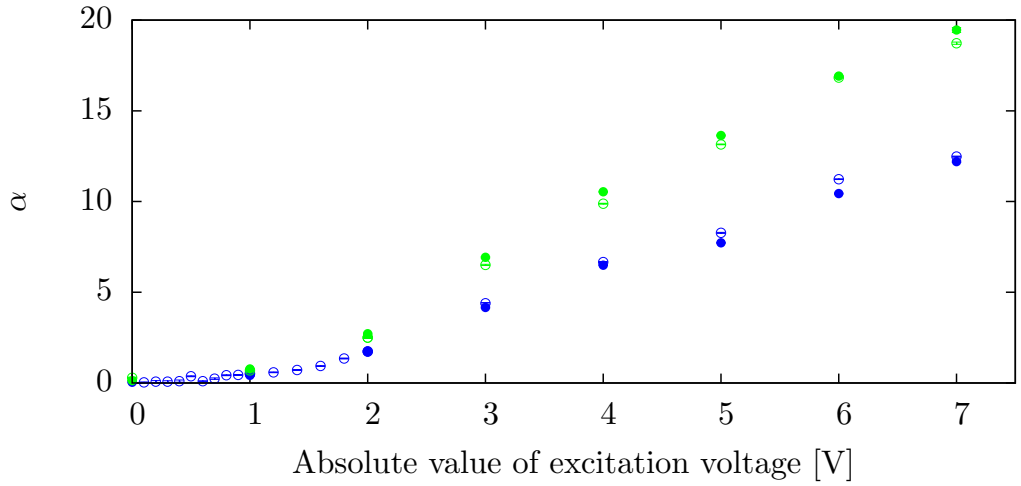

Figure 6.6.: Asymmetric coherent excitation: Using excitation pulses from segment 4 and segment 6 generated by positive (•) and negative (○) voltages. The general difference between the two segments correspond to an ion position closer at segment 4.

ion is trapped closer to segment 4 which could be explained by a ponderomotive force from the taper region RF electrode.

This technique is not recommended because the asymmetric voltage kick displaces the potential and changes the axial frequency. This leads to different displaced motional frequencies for varying excitation amplitude. A technique to generate axial frequency conserving kick operations is explained in the next section.

6.2.2. Symmetric Excitation

To perform a precise displacement operation, a symmetric excitation is more suitable. To realise a harmonic displaced potential with constant axial frequency the voltage ramps calculated in section 3.7 are used. The excitation consists of two simultaneous voltage changes at the trapping segment and one neighbouring segment. This leads to a fast shift of the harmonic potential and the ion populates a coherent distribution which can be analysed using the technique described in section 4.3.2.

In figure 6.7 the linear dependency between potential displacement and coherent state displacement α is shown. The linear relation $\alpha \propto 0.090(3) \cdot d_z$ occurs most probably from the rising slope of the voltage pulse and the low pass filtering.

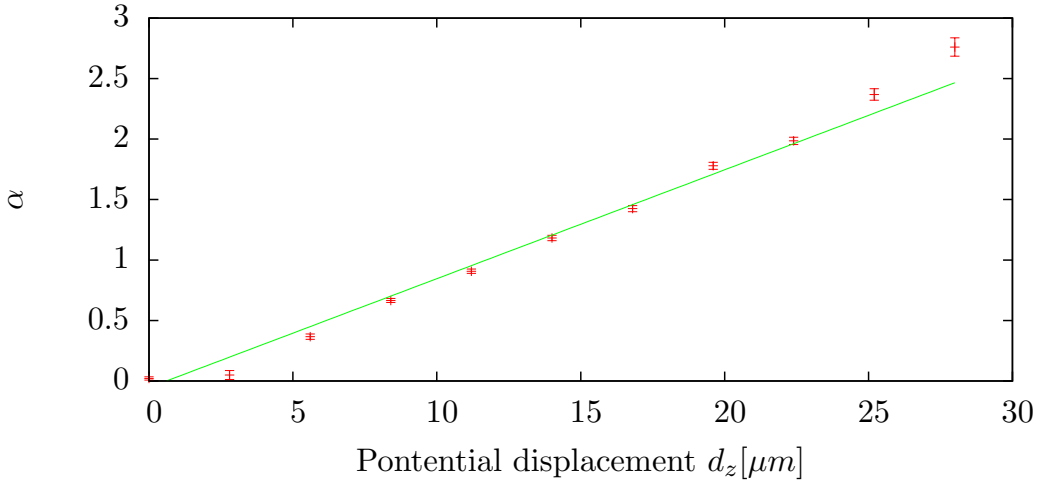

Figure 6.7.: Symmetric electric excitation measurement: The potential displacement give rise to a displacement operation with linear dependence on the distance ($\alpha \propto 0.090(3) \cdot d_z$).

6.2.3. Generation of Displaced Fock States

The dynamics of coherent excitation is now studied by changing the initial state. The coherent excitation of Fock states leads according to [BL73, dOKKB90] to an oscillating phonon distribution behaviour due to interference of different parts of the wave function. Fock states are generated from a ground state cooled ion with BSB pulses on the Raman transition. The coherent excitation is achieved by applying a voltage kick at one DC electrode close to the ion. The coherent excitation leads to displaced Fock states. Their phonon probability distribution is obtained from the overlap of the state $|\alpha, n\rangle$ with the Fock state $|l\rangle$:

$$p_n(\alpha, l) = |\langle l|\alpha, n\rangle|^2 = \left|\langle l|\,\hat{D}(\alpha)\,|n\rangle\right|^2 \tag{6.6}$$

Evaluation of this expression leads to [dOKKB90]:

$$p_n(\alpha, l) = \frac{e^{-|\alpha|^2}|\alpha|^{2(l-n))}}{n!l!} \times \left|\sum_{k=0}^{n} \frac{n!l!(-1)^k|\alpha|^{2(n-k)}}{k!(n-k)!(l-k)!}\right|^2 \tag{6.7}$$

In figure 6.8 the displaced Fock state is shown versus increasing displacment. The higher Fock states $|n = 1\rangle$ and $|n = 2\rangle$ show a reduced preparation fidelity as compared to the ground state. The individual phonon probabilities have been evaluated using the full phonon analysis described in section 4.3.2 without assuming a known distribution. Performing a closer look on the individual phonon probabilities we find a good agreement

with equation 6.7. The initial prepared Fock state was used as basis and the final result was obtained by superimposing the propagation of the relevant phonon numbers

$$p'_n(\alpha, l) = \frac{1}{C} \sum_{l=0}^{6} c_l p_n(\alpha, l) \tag{6.8}$$

With the initial prepared Fock state parameters c_l and there norm $C = \sum c_l$.

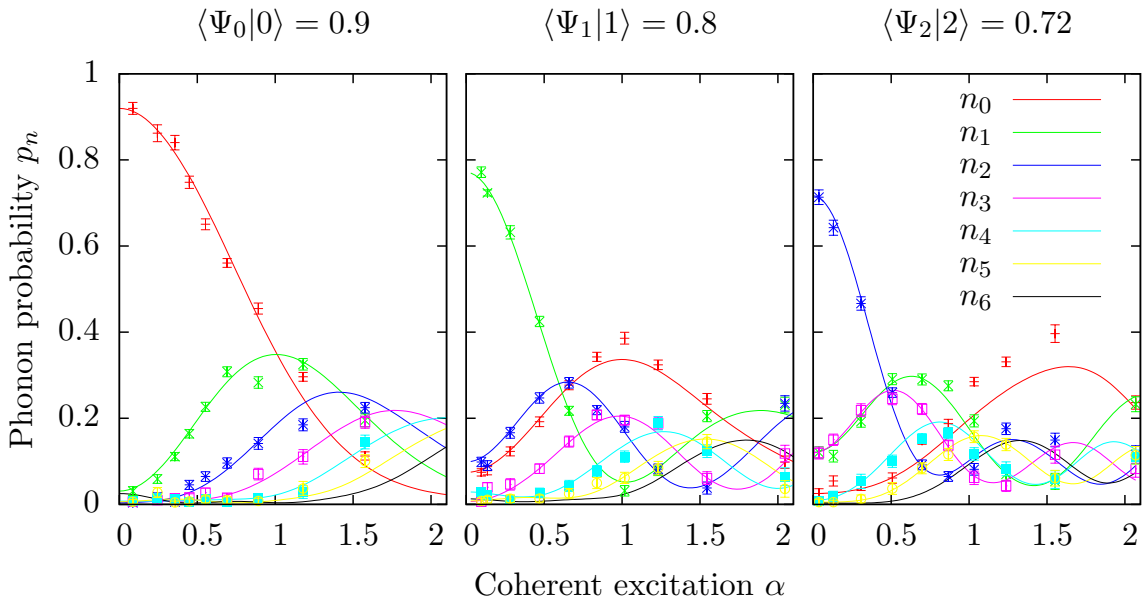

Figure 6.8.: Displaced Fock States: The lowest three fock states with phonon probabilities p_n as points and evaluated equation 6.7 as line.

This method proves the controllable interaction of the trap voltage supply with the ion wavepacket. The reliable generation of displaced Fock states is limited to the low phonon numbers because of the low state preparation fidelity.

6.3. Ultra Fast Transports Without Excitation as Architecture Building Block for Quantum Computing

Performing transport operations on the time scale of the axial frequency enables the fastest possible movement operations. These operations must be carried out with low residual energy transfer, leaving the ions close to the motional ground state, in order to perform transport based quantum protocols. In section 6.3.1 and 6.3.2 two schemes of non adiabatic ground state transport are described.

For fast transport operations two different realisations are demonstrated. In figure 6.9 (a) the *pairwise neutral* transport scheme is shown. The electrode voltages change from -5 V at the initial trapping segment and 0 V at the neighbouring segment to the inverted voltage configuration. Applying the voltage ramps calculated in section 3.7 realises a one segment transport with constant axial frequency. After a delay time τ_d the reversed voltage ramps are applied to perform an identical back transport. So the energy gain from the first transport can be cancelled by the second transport by choosing the appropriate delay time.

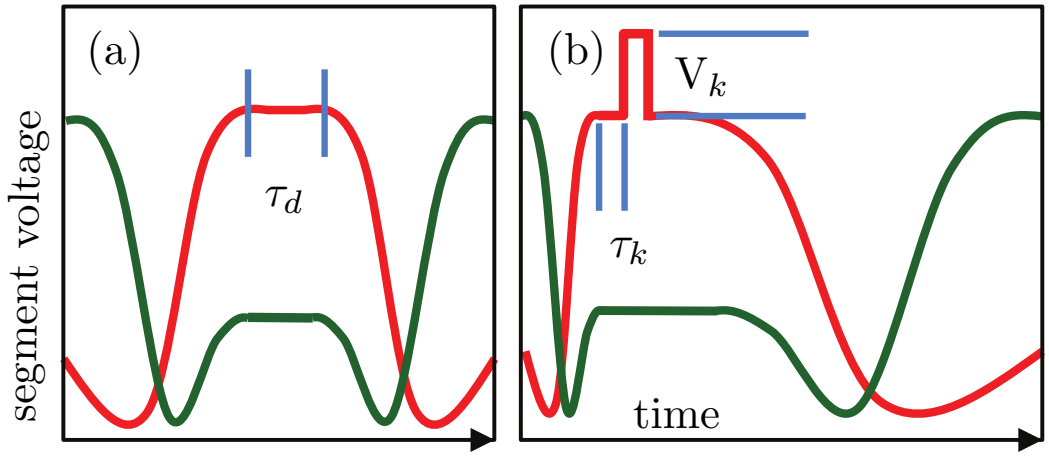

Figure 6.9.: Transport operations: The (a) pairwise neutral transport where the ion is transported from segment 5 to segment 4 using a defined voltage ramp. After a delay time τ_d the inverted voltage ramp brings the ion back for analysis. The (b) self-neutral scheme obtains a fast transport to the neighbouring segment, followed by a voltage kick which reduces the motional energy. An adiabatic back transport is performed to analyse the energy gain at the initial site.

The *self-neutral* transport scheme is shown in figure 6.9 (b) and realises a ground state transport to the neighbouring segment. A fast one segment transport is obtained by applying the voltage ramps calculated in section 3.7. The energy gain from this transport is now cancelled by a voltage kick of duration $\tau_k = 400\,\text{ns}$ and amplitude V_k. For the state detection and energy measurement the ion has to be transported back to the initial position. This is done by an adiabatic back transport with negligible effect on the ion energy.

6.3.1. Pairwise Neutral Transport Operation

The fact that preparation and detection of the ion have to be performed at the same axial trapping site is due to practical reasons. Some lasers and the detection apparatus

is used in both steps. The basic transport scheme consists of two opposite transport operations with a variable time delay in between. If the transport parameters can be

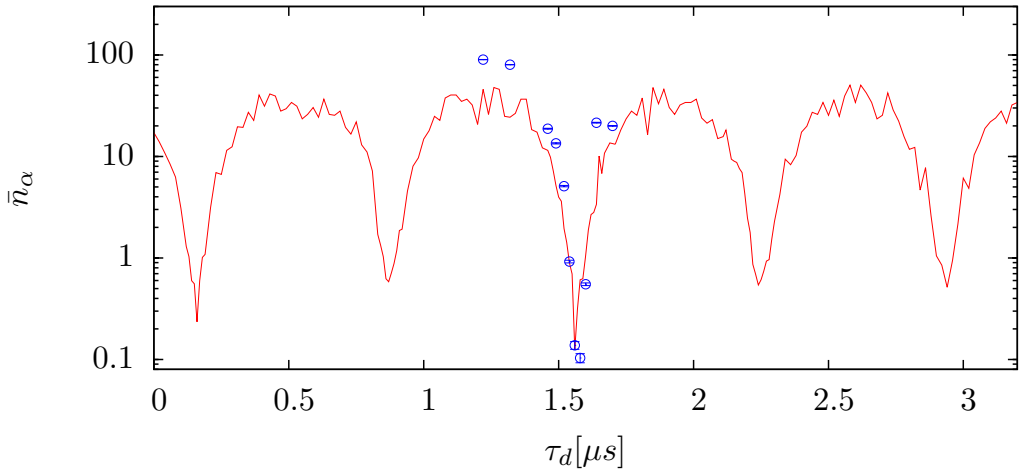

Figure 6.10.: Pairwise neutral transport: Two identical transport operations, separated by τ_d performing transport and back-transport with 11.2 μs each. The solid line corresponds to pseudo energy measured energy gain and the points to a full phonon analysis.

changed with aprecision better than the axial trap period $T = 2\pi/\omega_z$ one must observe a preiodic behaviour of the energy transfer. The delay time between the two transports can be scanned with 20 ns steps, which is the minimum time resolution of the arbitrary voltage supply from section 2.4. In figure 6.10 the periodic energy gain and energy neutral transports are shown. The pseudo energy measurement was used as wide range parameter scan while individual points with a full phonon analysis are used to precisely determine the energy gain. This transport was realised using the scheme of figure 6.9 (a) with each transport operation consisting of 28 voltage samples with 400 ns duration. The lowest energy gain corresponds to a mean phonon number $\bar{n}_\alpha = 0.10(1)$ where the coherent excitations from both transport operations cancels each other. The maximum coherent energy transfer is more than 100 phonons which is the sum of both transport operations.

This scheme proves that transport operations can be manipulated on the timescale of one axial oscillation period. The ground state transport is possible without significant energy gain and provides reproducible coherent excitation and deexcitation. The pairwise neutral transport is not scalable suited for transport based quantum computation because two transport operations are required for a cold transport. The next section explains a self-neutral transport scheme which can be concatenated to realise arbitrary long distance ground state transport operations.

6.3.2. Self-Neutral Transport Operation

A self-neutral one segment transport can be concatenated to realise arbitrary transport operations over all segments of the ion trap. This operations represents a building block for transport based quantum computing. Future additional operations like *splitting* and *merging* might also base on this principle.

The voltage ramps shown in figure 6.9 (b) consist of two asymmetric transports with an energy neutralising voltage kick in between. The first transport operation and the voltage kick are adjusted to be self-neutral. The adiabatic back transport is necessary for energy measurement. In figure 6.11 a self-neutral transport operation was analysed

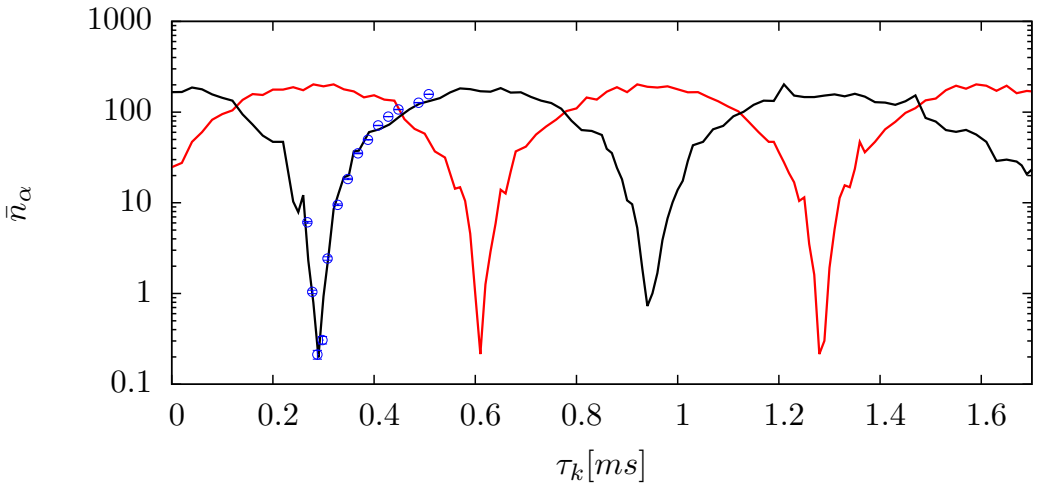

Figure 6.11.: Self-neutral transport: The measurement points are obtained using a full phonon analysis. The lines correspond to a pseudo energy gain due to varying kick delay for +3.85 V (red) and -3.68 V (black). The transport duration was chosen to be 4 μs with adiabatic return in 180 μs.

for positive and negative kick voltages with a varying kick time τ_k. The periodicity corresponds to the trap period. A change in polarity shifts the signal by half a trap period because the accumulated motional excitation is cancelled with the opposite force direction. The measurement points are obtained by a full phonon analysis described in section 4.3.2. The voltage ramp was generated using 10 samples with 400 ns each and one sample for the voltage kick. Including the kick delay the total transport time was 4.62 μs with an minimal energy gain of $\bar{n}_\alpha = 0.21(2)$. Due to the faster transport time also the maximum motional excitation is above 200 phonons.

6.3.3. Transport Optimisation using Spin-Motion Entangled States

The fast transport of ground state cooled ions has been proven to in the previous sections. A spin-motion superposition state in conjunction with a transport operation can be analysed using a Ramsey measurement scheme as described in section 5.3. A motional superposition state is generated and its phase evolves until the phase information is mapped back to the spin state. A similar technique was utilized to measure magnetic field gradients in section 6.1.2 using the two spin states $|\uparrow\rangle$ and $|\downarrow\rangle$ from the $S_{1/2}$ ground state. This signal can be used to minimize the magnetic field gradient and eliminate the shift. As background measurement is in figure 6.12 (a) shown that no magnetic field induced phase shift is acquired during one transport cycle on the $(|\uparrow\rangle + |\downarrow\rangle)\,|n=0\rangle$ state. The ground state spin-superposition shows full contrast after a transport to the neighbouring segment and back.

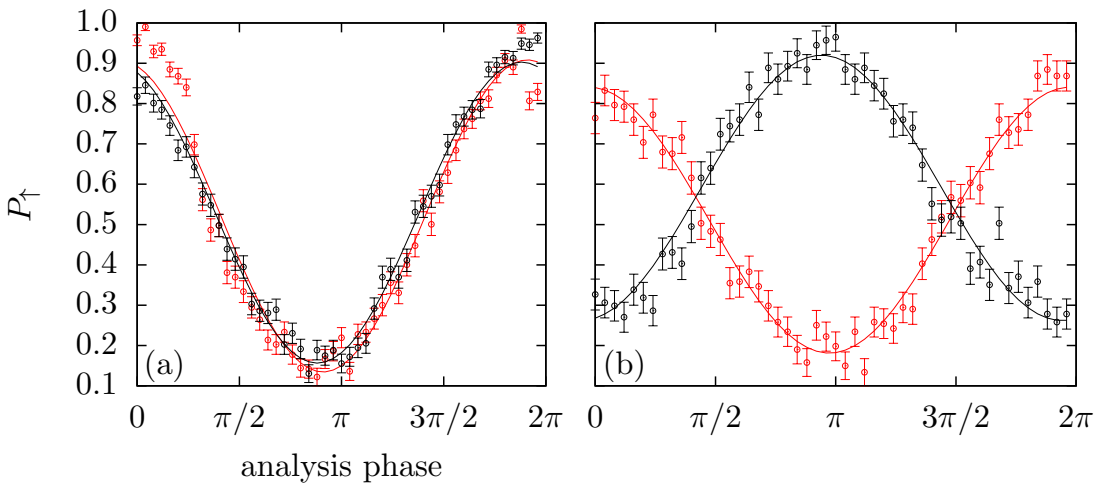

Figure 6.12.: Ramsey singal of ground state and spin-motion entangled state: The (a) spin state $(|\uparrow\rangle + |\downarrow\rangle)\,|n=0\rangle$ at rest (red) and after one transport cylce (black). No phase shift is observed because of the compensated magnetic field gradient. The spin motion superposition $|\uparrow, n=0\rangle + e^{i\Phi}\,|\downarrow, n=1\rangle)$ the observed shift occurs from a varying motional frequency during transport.

For measurement of the motional coherence a spin-motion entangled state is generated using a $\pi/2$ pulse on the BSB for a ground state cooled ion. This generates the state $|\uparrow, n=0\rangle + e^{i\Phi}\,|\downarrow, n=1\rangle)$. The phase shift will now only occur from a transient change of the motional frequency.

$$\Phi = \int_0^T \omega_0 - \omega(t)dt \tag{6.9}$$

The result for a non constant axial frequency is shown in figure 6.12. The moved measurement shows a phase shift due to the change of the axial frequency during transport.

A more detailed analysis is shown in figure 6.13 where the measured phase shift was used to derive the frequency deviation $\Delta\nu/\nu$. The ion is moved to the remote location and the superposition aquires phase for a duration τ which can be analysed as described. A variation of the remote location duration now obtaines the motional frequency difference at the remote location. Figure 6.13 (a) shows the deviation for a full transport with a 6% deviation directly in the centre between both electrodes. The ion is utilized as spin-motion entangled probe to minimize the frequency deviation on ten different transport distances. A voltage correction table is generated to realize a motional frequency precision along the transport path below 1 kHz shown in figure 6.13 (b).

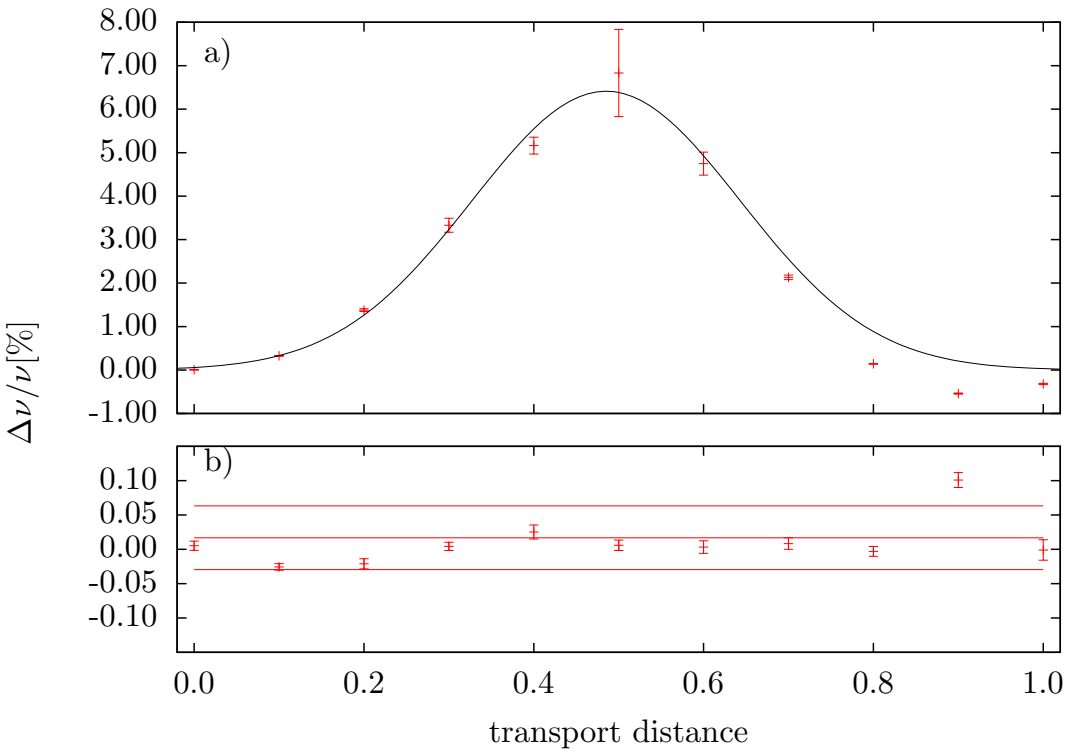

Figure 6.13.: Motional frequency deviation: a) axial frequency deviation for the uncorrected transport ramp, shown in figure 3.10. b) applying individual correction factors reduces the deviation by one order of magnitude where the dashed lines indicate the standard deviation.

The fast transport of a spin-motion entangled state showed now additional decoherence. This fast entanglement perserving transport of quantum systems could build the baisis of hibrid quantum systems.

7

Conclusion and Outlook

The realized experimental setup is capable of ion trap operation at low temperatures. The variable cryogen source allows economic and efficient usage of the liquidized gases Helium and Nitrogen. The ion trap setup was operated from 40 K to 320 K, performing accurate heating rate measurements with single ions in the wide region of the trap. The optimized laser setup allows fast and reproducible alignment of all laser beams on the ion. This first cryogenic 3D micro structured Paul trap experiment proved that a continuous temperature range from room temperature to cryogenic temperatures can be accessed within one experiment.

The implementation of a fibre optical resonator into a micro structured Paul trap proved the concept of resonator stabilisation while ion trap operation. The cavity resonator is successfully implemented in the ion trap design, allowing resonator locking to certain cavity modes. The design and mechanical stability of the cavity trap combination allows future quantum interfaces, using light as quantum information bus.

A multi channel arbitrary function generator, designed and optimized in house, is capable of generating voltage raps manipulating the quantum wave packet of single ions. The realized compromise of update rate and low pass filtering allows the manipulation of trapping potentials on the timescale of the motional frequency. This function generator opens the research field of transport based quantum computation and the development of the required protocols.

Ground state ion movements are developed as first building block of a transport based quantum processor. The possibility to generate and detect spin-motion entangled state transport operations allows successive improvement of voltage ramps obtained from

numerical simulation. The optimisation of these processes proved a consistent setup of ion trap hardware, experiment control and numerical simulation.

The cryogenic ion trap experiment discovered a non thermal driven source of heating. The future measurements will examine this heating which is assumed to occur from trap surface contamination. An Argon cleaning procedure might decrease this heating mechanism and give rise to study temperature dependent heating processes. Using the different ion-electrode distances along the trap axis, this experiment is suited to study the temperature and distance dependence of heating rates within one ion trap.

Manufacture problems of the fibre optical resonator requires the improvement of the production process. The next generation cavity fibres will have improved cavity mirror size and optical coating, which allows a larger ion-cavity distance. An improved construction will simplify the assembly of cavity and ion trap and reduce error sensibility.

The realisation of the arbitrary trap voltage generator gave rise to the first non-adiabatic transport operations in segmented traps. A future device could realise a voltage change much faster than the ions motion and study time dependent processes on ion crystals. Future noise analysis will improve the requirements for low pass filtering and allow faster potential changes. Future operations, like fast crystal splitting combined with concatenated transports of single ions will allow the realisation of transport based entanglement protocols. The generation large entangled quantum states can be studied and improved by operating in the narrow processing region in the trap.

A

Acronyms

3D	three dimensional
AOM	acousto optical modulator
ADC	analog to digital converter
API	application programming interface
ATE	automatic test equipment
BNC	bayonet navy connector
BEM	boundary element method
BSB	blue sideband
Ca	calcium
CAD	computer-aided design
CAR	carrier
CF	conflat
CLK	clock input
CS	chip select
DAC	digital to analog converter
DC	direct current

DDR-RAM double data rate random access memory

DIP dual in-line package

DMA direct memory access

DPDT double pole double throw

EMCCD electron multiplying charge-coupled device

EOM electro optical modulator

FDM finite difference method

FEM finite element method

FFT fast fourier transform

FIFO first in first out

FMM fast multipole method

FPGA field programmable gate array

GND ground

GUI graphical user interface

IR infra red

LED light emitting diode

LDAC load DAC

LSB least significant bit

LPT line print terminal

LVTTL low voltage transistor-transistor logic

op-amp operational amplifier

PBS polarising beam splitter

PDH Pound-Drever-Hall

PID proportional-integral-derivative

PMT photo multiplying tube

PC personal computer

PCI peripheral component interconnect bus

RAM random access memory

RF radio frequency

RSB red sideband

RWA rotating wave approximation

SDI serial data input

SHG second harmonic generation

SPI serial peripheral interface

SVD singular value decomposition

TSP titanium sublimation pump

TTL transistor-transistor logic

USB universal serial bus

UHV ultra high vacuum

UV ultra violet

VCO voltage controlled oscillator

VFG versatile frequency generator

B

Quantum Optics Laboratory Design

This section treats some general constrains which should be optimized for stable long term operation of a quantum optic laboratory. These kinds of experiments consists mainly of a dust and vibration sensitive laser setup, the quite robust vacuum chambers and various electronic control devices which are partial very sensitive to electrical noise. Due to its different sensitivity conditions a separation of the vacuum and the laser setup allows efficient design and use of infrastructure. In our case the laser setup and the ion trap setup are installed on two different optical tables and the control electronics are located above and below these tables. These considerations arise from the optimization of previous experimental designs and specific requirements for our experiment which could easily be adapted for different setups. The usual building infrastructure is an air conditioned room with the necessary connections for power supply, network connectivity, water cooling and compressed air. In figure B.1 you see a sketch of the actual laboratory with all relevant components. Usually there are also storage racks mounted at the ceiling above the optical tables to contain instruments. Cable chutes are installed to guide electric connections and optical fibres from one table to the other as well as connecting the experiment and the control desk. The focus for optimisation is always on the stability of the laser setup. Of course there are special requirements for the narrow line-width spectroscopy laser. In this section are only general considerations for the laser design. All optical components are mounted on an active levelling ibration insulation tables. These optical tables are hovering on compressed air pads which damp low frequency vibrations from the building. Common systems have one resonance frequency at about 1 Hz where now reduction of the oscillation amplitude is possible. For usual noise sources like vacuum pumps, equipment handling and foot traffic in the low

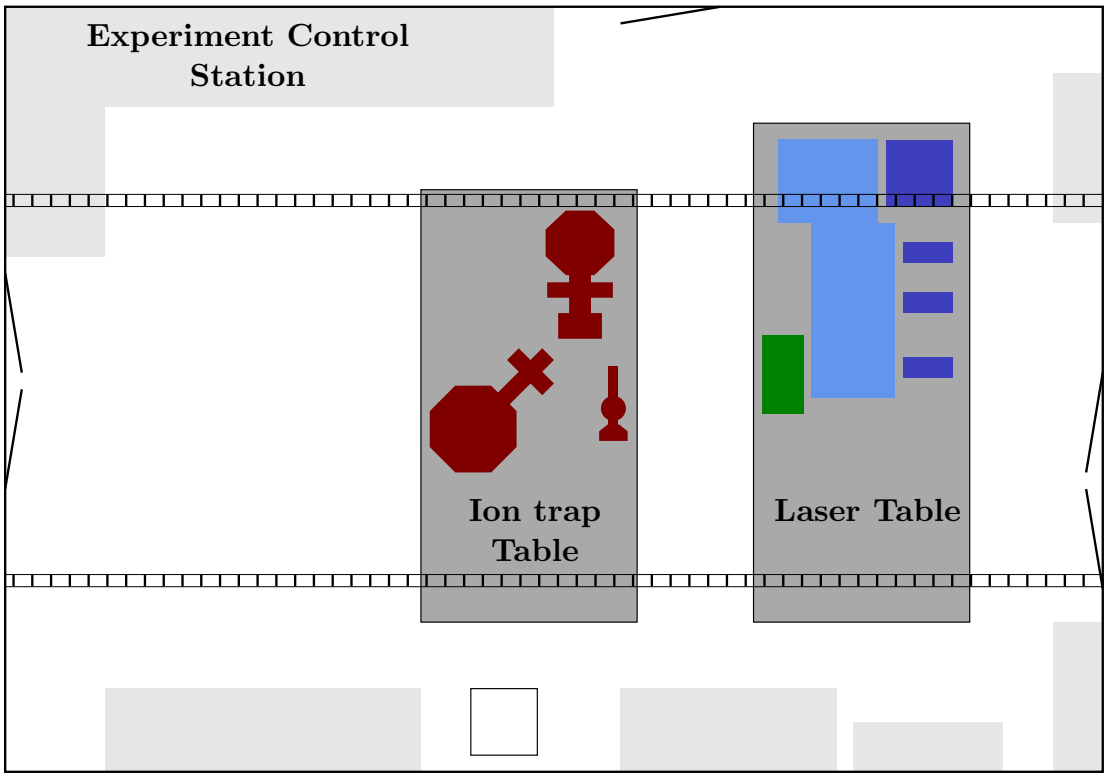

Figure B.1.: Sketch of Lab design: (light grey) indicates the lab infrastructure like furniture and in (dark grey) are the optical tables with active compressed air levelling. Three different ion traps experiments are highlighted in (dark red) and the laser sources are (blue). (light blue) shows the area of laser switching and routing while (green) is the optical resonator for frequency stabilisation.

frequency range from 2-50 Hz the damping increases to peak values of about 99 %. The larger frequencies are less likely or have insignificant oscillation amplitudes of the room floor. But higher frequency noise sources could also couple acoustically to the optical components. The main setup improvement can be a stable mount for all components which shifts resonance frequencies and increases mechanical stability. The setup of optical components should always be tried to optimize for long term stability. One goal is to use as less components as possible to limit effects from thermal expansions and vibration. Beam lines are planned through polarizing beam splitters (PBS) with preserving the polarisation as long as possible. Every additional polarisation optic component will introduce drifts in intensity due to thermal instability. Furthermore, dust contamination reduces the efficiency of all optical components in a beam line which is also reduced by keeping the amount of components as low as possible. Especially for SHG cavities at air pressure pollution is the main source of quality loss. On most experiments *flow*

boxes are used to create a laminar and clean air flow from above in combination with a surrounding enclosure. This creates an air flow through a set of dust filters onto the optics and out of the enclosure. This flow reduces the probability of dust moving in opposite direction to the air flow. One additional constraint is to reduce the amount of adjustment degrees of freedom to the necessary minimum. Even the long term stable micrometer adjusters from mirror holders introduce error sources like creeping. The

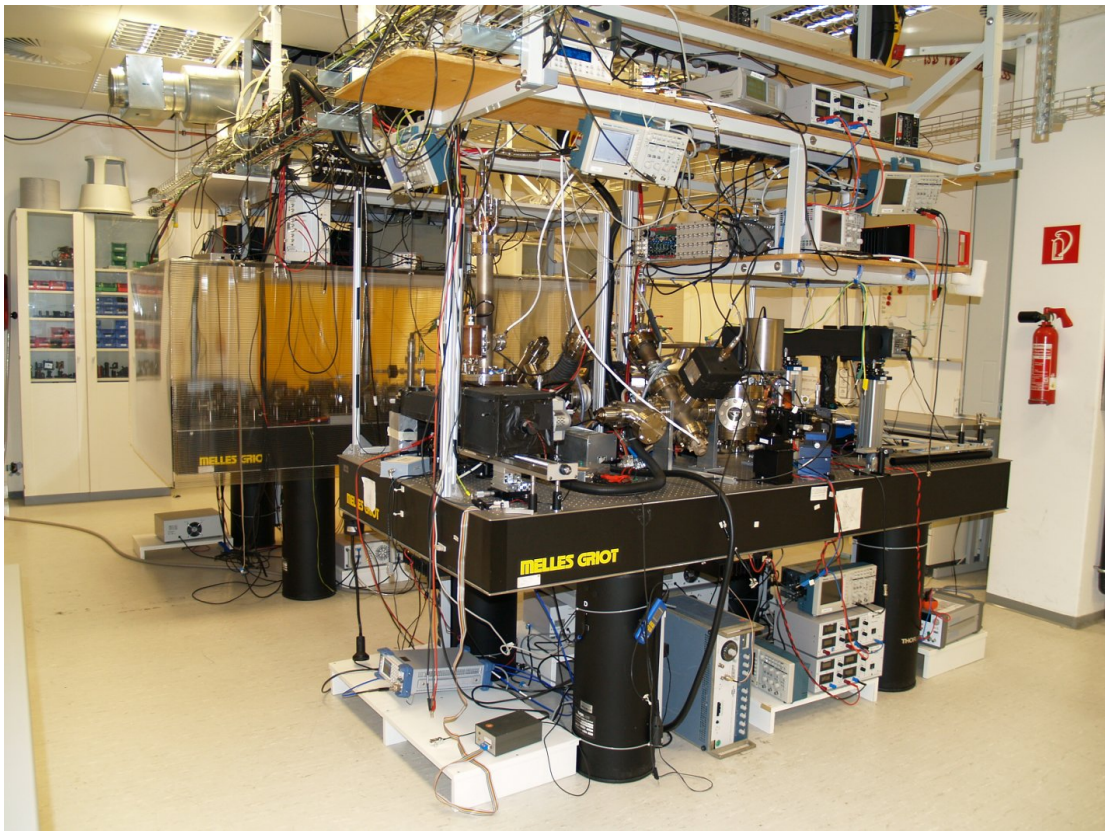

Figure B.2.: Quantum optics laboratory: From this viewpoint close to the experiment control station the ion trap table is in the front and the laser table in the back of the room. Instruments and power supplies above and below the tables are clearly visible.

vacuum setup of the ion trap is robust against dirt and does not require a flow box. This is mainly because all laser beams are guided using optical fibres directly to the viewport of the vacuum chamber[1]. The cryogenic ion trap design requires reproducible laser beam alignment because the cold finger of the continuous flow cryostat expands proportionally to the operation temperature. This means all laser beams must be re-

[1] A setup like this is only possible, if no interferometric stability is required.

aligned after changing the set temperature. Therefore the fibre couplers are mounted in a stable frame which provides the possibility to overlap various beams and align them on the trap center. Micrometer screws are utilized to align the beam and recover already known positions using the scale value and a created lookup table. The vacuum setup requires active pumping during operation. To achieve a vacuum of less than 10^{-11} mbar a combination of chemical vacuum pumps is used. In general, turbo molecular pumps which require an additional forepump are not recommended for reasons like high and low frequency acoustic noise and mechanical vibrations. The control electronics like laser control rack, acousto optical modulators for laser switching, photon detection system, control computers and trap DC voltage supply are quite different in the generation and sensitivity to noise. A general problem is instrument noise distribution due to ground loops. If multiple instruments share the same ground, noise produced from one instrument can couple to other instruments via the power supply line. There are several types of coupling, for example the ground line resistance leads to a noise shift of the ground level proportional to the current consumption of all attached instruments. Additional noise source distributed over the line voltage are produced by switching power supplies, in many devices like computers and general purpose instruments, which couple back to the power line on various frequencies. This is why lab instruments should be sorted in groups of noise sensitive instruments and noise generating instruments. These groups are supplied from different phases of the three-phase power lines with as far as possible separated ground connections. Obviously the most sensitive part of the experiment is the trapped ion, because every frequency component of electrical noise connected to the DC electrodes impresses a modulation of its position. These modulation effects all the ions motional state and optical transitions as discussed in chapter 5. These effects are minimized by heavy low pass filtering and low noise voltages sources. Because every filtering is a amplitude damping it is much more efficient to eliminate power line induced noise sources per se by using battery supplied voltages sources. If one needs to perform high speed transport operations, described in section 6.3, filtering is restricted and using a low noise power supply is the only solution. In conclusion there are some guidelines for setting up and operating a quantum optics laboratory:

- Voltages supplying ion traps must be low pass filtered and battery supplied
- Reduce amount of optical components to minimum
- Limit adjustment degree of freedom to necessary minimum
- Eliminate acoustic noise sources
- Guide laser in optical fibres as close as possible to the ion
- Separate instrument groups on different power lines to reduce noise coupling

The laser sources are mounted together on one optical table and lead through optical fibres to the ion trap. All laser light sources are commercial grating stabilised diode lasers. The control electronics of all laser is placed in shelf above the optical table.

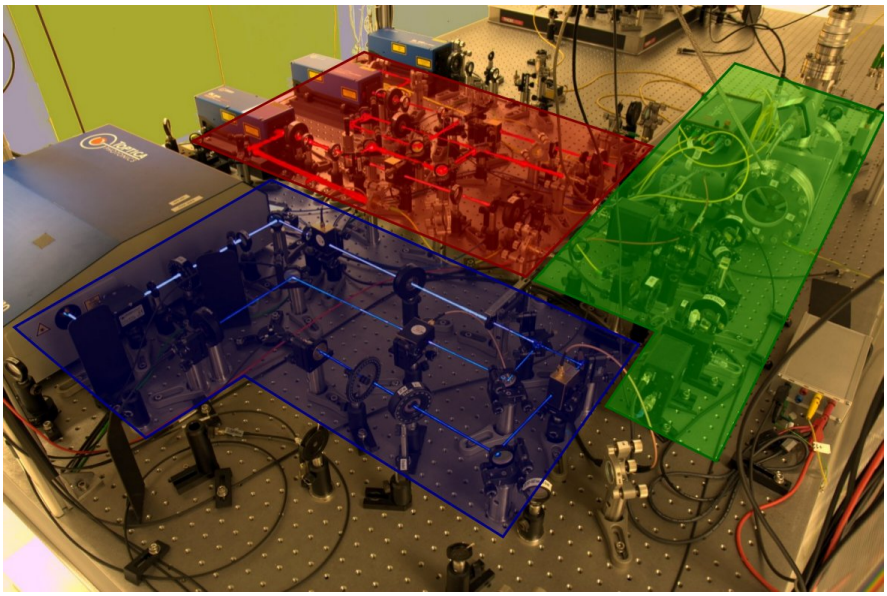

Figure B.3.: Laser setup: The optical setup required for controlling of the laser pulse sequences. Highlighted in blue, is the setup for the 397 nm laser used for Doppler cooling and detection. In red are both repump laser at 866 nm and 854 nm and green accents the laser wavelength measurement and stabilisation setup.

The individual racks control the laser diode current and temperature the piezo voltage and provide the necessary environment for frequency stabilisation. Figure B.3 shows a picture of the optical setup. To improve stability and reduce error sources the setup is designed as compact as possible. All relevant laser components to trap and observe ions find their space on half an optical table.

C

Lab Parameter Sheet

Laser	power at chamber	beam waist
397 nm sat.	115 μW	$\approx$ 80 μm
397 nm desat.	10 μW	$\approx$ 80 μm
397 nm σ	6 μW	$\approx$ 100 μm
866 nm	55 μW	$\approx$ 200 μm
854 nm	11 μW	$\approx$ 200 μm
423 nm	1100 μW	$\approx$ 100 μm
375 nm	280 μW	$\approx$ 80 μm
729 nm	25 mW	$\approx$ 10 μm

Table C.1.: Laser Power and Beam Dimension

Laser	Wavelength/nm (vac.)
Doppler	793.91820
Repump $D_{5/2} \rightarrow P_{3/2}$	854.44440
Repump $D_{3/2} \rightarrow P_{1/2}$	866.45200
Quadrupole $S_{1/2} \rightarrow D_{5/2}$	729.34758
Photoion $S_0 \rightarrow P_0$	422.79230
HeNe	632.9912347

Table C.2.: Wavemeter laser wavelengths

D

Publications

D.1. Peer reviewed journal publications

[ZRW+12] **F. Ziesel**, T. Ruster, A. Walther, H. Kaufmann, K. Singer, F. Schmidt-Kaler, and U. G. Poschinger. Experimental creation and analysis of displaced number states. arXiv:quant-ph/1211.5490, 2012 (submitted to J Phys B).

[WPZ+11] A. Walther*, **F. Ziesel***, T. Ruster, S. T. Dawkins, K. Ott, M. Hettrich, K. Singer, F. Schmidt-Kaler, U. G. Poschinger, "Controlling fast transport of cold trapped ions", Physical Review Letters 109, 080501 (2012) (* equal contribution)

[PWH+12] U. G. Poschinger, A. Walther, M. Hettrich, **F. Ziesel**, F. Schmidt-Kaler, "Interaction of a laser with a qubit in thermal motion and its application to robust and efficient readout", Applied Physics B: Lasers and Optics 107, 1159 (2012)

[NDM+11] S. Narayanan, N. Daniilidis, S. Möller, R. Clark, **F. Ziesel**, K. Singer, F. Schmidt-Kaler, H. Häffner, "Electric field compensation and sensing with a single ion in a planar trap", Journal of Applied Physics 110, 114909 (2011)

[WPZ+11] A. Walther, U. G. Poschinger, **F. Ziesel**, M. Hettrich, A. Wiens, J. Welzel, F. Schmidt-Kaler , "Single ion as a shot-noise-limited magnetic-field-gradient probe", Physical Review A 83, 062329 (2011)

[SPM+10] K. Singer, U. G. Poschinger, M. Murphy, P. A. Ivanov, **F. Ziesel**, T. Calarco, F. Schmidt-Kaler, "Colloquium: Trapped ions as quantum bits: Essential numerical tools", Review of Modern Physics 82, 2609 (2010)

D.2. Peer reviewed journal publications from earlier work

[HZP+10] G. Huber, **F. Ziesel**, U. G. Poschinger, K. Singer, F. Schmidt-Kaler, "A trapped-ion local field probe", Applied Physics B: Lasers and Optics 100, 725 (2010)

[PHZ+09] U. G. Poschinger, G. Huber, **F. Ziesel**, M. Deiss, M. Hettrich, S. A. Schulz, G. Poulsen, M. Drewsen, R. J. Hendricks, K. Singer, F. Schmidt-Kaler, "Coherent Manipulation of a 40Ca+ Spin Qubit in a Micro Ion Trap", Journal of Physics B 42, 154013 (2009)

[Ste08] S. A. Schulz, U. G. Poschinger, **F. Ziesel**, F. Schmidt-Kaler, "Sideband cooling and coherent dynamics in a microchip multi-segmented ion trap", New Journal of Physics 10, 045007 (2008)

D.3. Talks

Progress report Ulm mictrotrap group, MICROTRAP project meeting, Denmark, Aarhus, 2008

D.4. Posters

Kontrollierte Transporte in mikrostrukturierten Ionenfallen, DPG Frühjahrstagung, Hamburg 2009

Cryogenic Micro Ion Trap with integrated Fiber cavity, SCALA summer school, Institut d'Études Scientifiques de Cargèse 2009

Cryogenic Micro Ion Trap with integrated Fiber cavity, DPG Frühjahrstagung, Hannover 2010

Integration and stabilization of a fiber cavity within a cryogenic micro ion trap, Bad Honef 2011

Bibliography

[BAO+12] A Bermudez, J Almeida, K Ott, H Kaufmann, S Ulm, U Poschinger, F Schmidt-Kaler, A Retzker, and M BPlenio. Quantum magnetism of spin-ladder compounds with trapped-ion crystals. *New Journal of Physics*, 14(9):093042, 2012.

[BL73] M Boiteux and A Levelut. Semicoherent states. *Journal of Physics A: Mathematical, Nuclear and General*, 6(5):589, 1973.

[CG69] K. E. Cahill and R. J. Glauber. Ordered expansions in boson operators. *Phys. Rev.*, 177, 1969.

[Deu08] C. Deutsch. High finesse fibre fabry-perot resonators; production,characterization and applications, 2008.

[DHK+83] R.W.P. Drever, J.L. Hall, F.V. Kowalski, J. Hough, G.M. Ford, A.J. Munley, and H. Ward. Laser phase and frequency stabilization using an optical resonator. *Appl. Phys.*, 31:97, 1983.

[dOKKB90] F. A. M. de Oliveira, M. S. Kim, P. L. Knight, and V. Buek. Properties of displaced number states. *Phys. Rev. A*, 41:2645–2652, Mar 1990.

[DOS+06] L. Deslauriers, S. Olmschenk, D. Stick, W. K. Hensinger, J. Sterk, and C. Monroe. Scaling and suppression of anomalous heating in ion traps. *Phys. Rev. Lett.*, 97:103007, Sep 2006.

[DW87] Frank Diedrich and Herbert Walther. Nonclassical radiation of a single stored ion. *Phys. Rev. Lett.*, 58:203–206, Jan 1987.

[Fra] Alexander Franzens. `http://www.gwoptics.org/ComponentLibrary/`.

[Gho95] P.K. Ghosh. *Ion Traps*. Clarendon Press, Oxford, 1995.

[GHSK08] W. Schnitzler R. Reichle K. Singer G. Huber, T. Deuschle and F. Schmidt-Kaler. Transport of ions in a segmented linear paul trap in printed-circuit-board technology. *New J. Phys.*, 10:013004, 2008.

[HCW+12] D. A. Hite, Y. Colombe, A. C. Wilson, K. R. Brown, U. Warring, R. Jördens, J. D. Jost, K. S. McKay, D. P. Pappas, D. Leibfried, and D. J. Wineland. 100-fold reduction of electric-field noise in an ion trap cleaned with *In Situ* argon-ion-beam bombardment. *Phys. Rev. Lett.*, 109:103001, Sep 2012.

[Het09] Max Hettrich. Präparation eines 40ca+-quantenbits und entwicklung eines faseroptischen resonators für seine detektion. Master's thesis, Ulm, 2009.

[HS75] T. Hänsch and A. Schawlow. Cooling of gases by laser radiation. *Opt. Commun.*, 13:68, 1975.

[Hun05] D. Hunger. Herstellung und charakterisierung von faserresonatoren hoher finesse, 2005.

[HZP+10] G. Huber, F. Ziesel, U. G. Poschinger, K. Singer, and F. Schmidt-Kaler. A trapped-ion local field probe. *Applied Physics B: Lasers and Optics*, 100:725, 2010.

[KMW02] D. Kielpinski, C. Monroe, and D.J. Wineland. Architecture for a large-scale ion-trap quantum computer. *Nature*, 417:709, 2002.

[KUJ+12] H. Kaufmann, S. Ulm, G. Jacob, U. Poschinger, H. Landa, A. Retzker, M.B. Plenio, and F. Schmidt-Kaler. Precise experimental investigation of eigenmodes in a planar ion crystal. *arXiv:1208.4040*, 2012.

[Len] H. Lenk. Op40 segmentcontroller funktionsbeschreibung. Documentation, Quantum, University Mainz.

[LGA+08] Jaroslaw Labaziewicz, Yufei Ge, Paul Antohi, David Leibrandt, Kenneth R. Brown, and Isaac L. Chuang. Suppression of heating rates in cryogenic surface-electrode ion traps. *Phys. Rev. Lett.*, 100:013001, Jan 2008.

[LGL+08] Jaroslaw Labaziewicz, Yufei Ge, David R. Leibrandt, Shannon X. Wang, Ruth Shewmon, and Isaac L. Chuang. Temperature dependence of electric field noise above gold surfaces. *Phys. Rev. Lett.*, 101:180602, Oct 2008.

[LKS+05] D. Leibfried, E. Knill, S. Seidelin, J. Britton, R.B. Blakestad, J. Chiaverini, D.B. Hume, W.M. Itano, J.D. Jost, C. Langer, R. Ozeri, R. Reichle, and D. Wineland. Creation of a six-atom 'schrodinger cat' state. *Nature*, 438:639, 2005.

[NDM+11] S. Narayanan, N. Daniilidis, S. Möller, R. Clark, F. Ziesel, K. Singer, F. Schmidt-Kaler, and H. Häffner. Electric field compensation and sensing with a single ion in a planar trap. *Journal of Applied Physics*, 110:114909, 2011.

[NHTD78] W. Neuhauser, M. Hohenstatt, P. Toschek, and H. Dehmelt. Optical-sideband cooling of visible atom cloud confined in parabolic well. *Phys. Rev. Lett.*, 41:223, 1978.

[PHZ+09] U. G. Poschinger, G. Huber, F. Ziesel, M. Deiss, M. Hettrich, S. A. Schulz, G. Poulsen, M. Drewsen, R. J. Hendricks, K. Singer, and F. Schmidt-Kaler. Coherent manipulation of a 40ca+ spin qubit in a micro ion trap. *Journal of Physics B*, 42:154013, 2009.

[POF58] W. Paul, Q. Osberghaus, and E. Fischer. Ein Ionenkäfig. *Forschungsberichte des Wirtschafts- und Verkehrsministeriums Nordrhein-Westfalen*, 415, 1958.

[Pos10] U. G. Poschinger. Quantum optics experiments in a microstructured ion trap. *Dissertation, Universität Ulm*, 2010.

[PS53] W. Paul and H. Steinwedel. Quadrupole mass filter. *Z. Naturforsch.*, A8:448, 1953.

[PWH+12] U. G. Poschinger, A. Walther, M. Hettrich, F. Ziesel, and F. Schmidt-Kaler. Interaction of a laser with a qubit in thermal motion and its application to robust and efficient readout. *Applied Physics B: Lasers and Optics*, 107:1159, 2012.

[PWSSK10] U. G. Poschinger, A. Walther, K. Singer, and F. Schmidt-Kaler. Observing the phase space trajectory of an entangled matter wave packet. *Physical Review Letters*, 105:263602, 2010.

[Ram86] N. F. Ramsey. *Molecular Beams.* Clarendon Press, 1986.

[Sch09] Stephan Schulz. *Scalable Microchip Ion Traps for Quantum Computation.* PhD thesis, Ulm, 2009.

[SPM+10] K. Singer, U. G. Poschinger, M. Murphy, P. A. Ivanov, F. Ziesel, T. Calarco, and F. Schmidt-Kaler. Colloquium: Trapped ions as quantum bits: Essential numerical tools. *Review of Modern Physics*, 82:2609, 2010.

[Ste97] A. Steane. The ion trap quantum information processor. *Appl. Phys. B*, 64:632, 1997.

[Ste08] Stephan Schulz, Ulrich Poschinger, Frank Ziesel, Ferdinand Schmidt-Kaler . Sideband cooling and coherent dynamics in a microchip multi-segmented ion trap. *New J. Phys.*, 10:045007, 2008.

[TKK+00] Q. A. Turchette, Kielpinski, B. E. King, D. Leibfried, D. M. Meekhof, C. J. Myatt, M. A. Rowe, C. A. Sackett, C. S. Wood, W. M. Itano, C. Monroe, and D. J. Wineland. Heating of trapped ions from the quantum ground state. *Phys. Rev. A*, 61:063418, May 2000.

[WD75] D.J. Wineland and H. Dehmelt. Proposed 1014 $\delta\nu/\nu$ laser fluorescence spectroscopy on tl + mono-ion oscillator iii. *Bull. Am. Soc.*, 20:637, 1975.

[WEL+07] J.H. Wesenberg, R.J. Epstein, D. Leibfried, R.B. Blakestad, J. Britton, J.P. Home, W.M. Itano, J.D. Jost, E. Knill, C. Langer, R. Ozeri, S. Seidelin, and D.J. Wineland. Fluorescence during doppler cooling of a single trapped ion. *Phys. Rev. A*, 76:053416, 2007.

[WPZ+11] A. Walther, U. G. Poschinger, F. Ziesel, M. Hettrich, A. Wiens, J. Welzel, and F. Schmidt-Kaler. Single ion as a shot-noise-limited magnetic-field-gradient probe. *Physical Review A*, 83:062329, 2011.

[WZR+12] A. Walther, F. Ziesel, T. Ruster, S. T. Dawkins, K. Ott, M. Hettrich, K. Singer, F. Schmidt-Kaler, and U. G. Poschinger. Controlling fast transport of cold trapped ions. *Physical Review Letters*, 109:080501, 2012. APS viewpoint article: http://physics.aps.org/articles/v5/94.

[Zie08] Frank Ziesel. Spektroskopie und transport von ionen in einer mikrofalle. Diplomarbeit, Universität Ulm, 2008.

[ZRW+12] F. Ziesel, T. Ruster, A. Walther, H. Kaufmann, K. Singer, F. Schmidt-Kaler, and U. G. Poschinger. Experimental creation and analysis of displaced number states. *arXiv:quant-ph/1211.5490*, 2012.

F

Acknowledgements

Der Aufbau und Betrieb eines solch komplexen Experiments wäre allein nicht denkbar. Während des Verlaufes dieser Doktorarbeit haben verschiedene Personen entscheidend zu ihrem Erfolg beigetragen. Mein Dank gilt vor allem meinem Betreuer Prof Ferdinand Schmidt-Kaler für die ursprüngliche Idee, seinem immer gerne geteilten Erfahrungsschatz und den konstruktiven Diskussionen.

Bei der Planung des experimentellen Aufbaus ersparte das Wissen von S. Schulz eine lange Einarbeitungszeit. Bei der Herstellung der mechanischen Komponenten gilt es der Universitätswerkstatt Ulm allgemein, Herrn Feierabend, Herrn Rapp, Herrn Haringer und Herrn Kogler im Besonderen für ihren kompetenten Rat und die fachkundige Arbeit zu danken. Während des Aufbaus war die tatkräftige Unterstützung von Michaela Petrich und Max Hettrich eine große Hilfe.

Der Umzug des Experiments von Ulm nach Mainz wäre ohne die freundliche Unterstützung von Herrn Becker nicht möglich gewesen. Dank gilt auch dem Kranfahrer, welcher mein Experiment sicher in das zweite Stockwerk befördert hat, sowie der Firma Hasenkamp, die für den sicheren Transport gesorgt hat.

Ein besonderer Dank gilt all meinen Kollegen der Arbeitsgruppe Quanteninformationsverarbeitung für die fachlich und privat verbrachten Momente. Die produktiven Diskussionen und die konstruktive Kritik, welche in lockerer Runde in der Kaffeepause entstanden sind, haben entscheidend zu meiner persönlichen Weiterbildung beigetragen. Der offene Gedankenaustausch mit Georg Jacob führte zu vielen kreativen Ansätzen und Lösungen. Die unermüdliche Arbeit aller am Experiment beteiligten Doktoranden und Diplomanden war essenziell für die Umsetzung dieses Projekts. Mein Dank gilt

Michaela Petrich, Daniel Heinrich, Alex Wiens, Konstantin Ott und Tim Lindner für ihren überdurchschnittlichen Einsatz. Entscheidend beteiligt am Erfolg dieser Arbeit war Max Hettrich, der über die Jahre immer ein treuer Leidens- und Kampfgefährte war. Besonders erwähnen möchte ich die Unterstützung von Ulrich G. Poschinger, welcher mich stets mit Sachverstand, theoretischem Hintergrund und Laborausrüstung unterstützt hat.

The author acknowledges support from in form of illustration templates[Fra].

Funding from the EU within the research programs MICROTRAP, SCALA, AQUTE and the MRTN EMALI, and from the DFG within the framework SFB/TRR21 is gratefully acknowledged.